POLARIZATION ANGLE CALIBRATION AND B-MODE CHARACTERIZATION WITH THE BICEP AND *Keck Array* CMB TELESCOPES

A DISSERTATION SUBMITTED TO THE FACULTY OF THE UNIVERSITY OF MINNESOTA BY

ERIC BULLOCK

IN PARTIAL FULFILLMENT OF THE REQUIREMENTS FOR THE DEGREE OF DOCTOR OF PHILOSOPHY

MARCH 2018

ACKNOWLEDGMENTS

The BICEP and *Keck Array* Collaborations include many talented scientists, without whom this dissertation would not be possible. I especially thank my advisor, Clem Pryke, for teaching me about thorough investigation and clear communication. I also thank Stefan Fliescher for our in depth discussions and for helping write the code used to model the Dielectric Sheet Calibrator data. A special thank you goes to the current and former graduate students at the University of Minnesota who have greatly improved my lab experience: Chris Sheehy, Justin Willmert, Mike Crumrine, Kenny Lau, Jaime Cheshire, and Grantland Hall.

In addition to Clem, I'm grateful to John Kovac, Jamie Bock, and Chao-Lin Kuo who have exceptionally led the collaborations. I also appreciate all of the senior scientists, postdocs, grad students, and engineers who have offered insight into problems I faced and have made collaboration meetings and deployments to South Pole interesting and fun. Besides the people already mentioned above, the list includes Zeesh Ahmed, Denis Barkats, Colin Bischoff, Rachel Bowens-Rubin, Immanuel Buder, Victor Buza, Jake Connors, James Cornelison, Tyler St. Germaine, Jimmy Grayson, Madeline Hickman, Howard Hui, Jae Hwan Kang, Kirit Karkare, Ethan Karpel, Sinan Kefeli, Sarah Kernasovskiy, Nicole Larsen, Toshiya Namikawa, Hien Nguyen, Roger O'Brient, Walt Ogburn, Steve Sansone, Caroline Sorensen, Zak Staniszewski, Bryan Steinbach, Grant Teply, Keith Thompson, Jamie Tolan, Abby

Vieregg, Chin Lin Wong, Kimmy Wu, and Eric Yang. I also thank Yuki Takahashi and Randol Aikin whose work with a Dielectric Sheet Calibrator on BICEP1 and BICEP2 served as a starting point for a large portion of this dissertation.

Our winterovers, the people who spend at least nine consecutive months at South Pole to operate our telescopes are all amazingly dedicated. Thank you Steffen Richter (BICEP2), Robert Schwarz (*Keck Array*), Sam Harrison (BICEP3), Hans Boenish (BICEP3), and Grantland Hall (BICEP3).

Most importantly, I thank my family for their support and advice throughout my entire academic career.

ABSTRACT

Since its discovery in 1964, the Cosmic Microwave Background (CMB) has led to widespread acceptance of the Big Bang cosmological paradigm as an explanation for the evolution of the Universe. However, this paradigm does not explain the origin of the initial conditions, leading to such issues as the "horizon problem" and "flatness problem." In the early 1980's, the inflationary paradigm was introduced as a possible source for the initial conditions. This theory postulates that the Universe underwent a period of exponential expansion within a tiny fraction of a second after the beginning. Such an expansion is predicted to inject a stochastic background of gravitational waves that could imprint a detectable B-mode (curl-like) signal in the polarization of the CMB. It is this signal that the family of telescopes used by the BICEP1, BICEP2, and *Keck Array* collaborations were designed to detect. These telescopes are small aperture, on-axis, refracting telescopes. We have used the data from these telescopes, particularly BICEP2 and the *Keck Array*, to place the tightest constraints, as of March 2016, on the tensor-to-scalar ratio of the CMB of $r_{0.05} < 0.07$.

In this dissertation, we provide an overview of the *Keck Array* telescopes and analysis of the data. We also investigate, as the main focus of this dissertation, a device we call the Dielectric Sheet Calibrator (DSC) that is used to measure the polarization angles of our detectors as projected on the sky. With these measurements, we gain the potential to separate

the polarization rotation effects of parity-violating physics, such as cosmic birefringence, from a systematic uncertainty on our detectors' polarization angles. Current calibration techniques for polarization sensitive CMB detectors claim an accuracy of $\pm 0.^{\circ}5$, which sets a limit for determining the usefulness of the DSC. Through a series of consistency tests on a single *Keck Array* receiver, we demonstrate a statistical uncertainty on the DSC measurements of $\pm 0.^{\circ}03$ and estimate a systematic uncertainty of $\pm 0.^{\circ}2$. which meets the minimum goal. We also conclude that there is no conflict between the DSC-derived polarization angles of this single receiver and the rotation derived from that receiver's CMB data under the hypothesis of no cosmic birefringence.

TABLE OF CONTENTS

LIST OF FIGURES

LIST OF TABLES

Chapter 1

INTRODUCTION

Over the millennia, civilizations have looked toward the sky with curiosity and wonderment. Pondering over those points of light now known to be planets within our solar system and stars far beyond lead to the seemingly ubiquitous question of the human psyche—"What is our place in the Universe?" The path toward answering this question was guided by logic, reason, and philosophy, which eventually lead to a geocentric model of the Universe. There have been several versions of the geocentric model, but they all share some basic concepts: the earth is stationary at the center of the Universe and all celestial objects, like the sun, moon, planets, and stars, orbit the earth.

Though the question "What is our place in the Universe?" has both physical and philosophical qualities, knowledge of the physical aspect has evolved to use science instead of philosophy over the last few centuries. It is the physical portion of this question that we will address in this dissertation.

1.1 Cosmology

We begin with a description of cosmology. In broad terms, cosmology is the study of the Universe. More specifically, cosmologists concern themselves with the origin, evolution, fate, geometry, and matter/energy content of the Universe. To address such enormous questions, we begin with the cosmological principle, which states that there are no special locations or directions in the Universe, at least on large enough scales. Said another way, the Universe is homogeneous and isotropic. Observational evidence from galaxy surveys (e.g., [1, 2]) indicates that our Universe meets these criteria on scales larger than around 100 megaparsecs, about 3.1×10^{24} m.

Throughout the rest of this section, we follow the notations in chapter 22 of the Particle Data Group's 2016 review [3]. We begin with the Robertson-Walker metric, a solution to Einstein's general relativity field equations. Setting $c = 1$, the space-time separation between two events, ds, is described by

$$ds^2 = dt^2 - R^2(t)\left[\frac{dr^2}{1-kr^2} + r^2\left(d\theta^2 + \sin^2\theta d\phi^2\right)\right], \tag{1.1}$$

where r, θ, and ϕ are spherical coordinates; t is a temporal coordinate; R is the Ricci scalar; and k is a curvature constant that can only take on the values $+1$, -1, or 0, depending on whether the geometry is closed, open, or spatially flat, respectively. It is common to replace R with a dimensionless scale factor $a(t)$ such that $a(t) = R(t)/R_0$ and where R_0 is $R(t_0)$, the value of R at present. It follows that $a(t_0) = 1$.

Combining the Robertson-Walker metric with Einstein's field equations, we can write

the Friedmann equations, which are the cosmological equations of motion. They are

$$H^2 \equiv \left(\frac{\dot{R}}{R}\right)^2 = \frac{8\pi G_{\rm N}\rho}{3} - \frac{k}{R^2} + \frac{\Lambda}{3} \tag{1.2}$$

$$\frac{\ddot{R}}{R} = \frac{\Lambda}{3} - \frac{4\pi G_{\rm N}}{3}\left(\rho + 3p\right), \tag{1.3}$$

where $H(t)$ is the Hubble parameter describing the expansion rate of the Universe at time t, $G_{\rm N}$ is Newton's gravitational constant, ρ is the density, and Λ is a cosmological constant. We can combine Equations (1.2) and (1.3) to derive the energy-momentum relation

$$\dot{\rho} = -3H\left(\rho + p\right). \tag{1.4}$$

Further, we can use Equation (1.2) to define a critical density

$$\rho_{\rm c} \equiv \frac{3H^2}{8\pi G_{\rm N}}, \tag{1.5}$$

which specifies the density of the Universe which separates a closed and open geometry in the absence of Λ. We can then introduce a density parameter $\Omega_{\rm tot}$, such that

$$\Omega_{\rm tot} \equiv \frac{\rho}{\rho_{\rm c}}. \tag{1.6}$$

It is common to split the total density into its components of pressureless matter ($\Omega_{\rm m}$), relativistic particles ($\Omega_{\rm r}$), and a vacuum energy density ($\Omega_{\rm v}$). If the vacuum energy density is constant, we may replace $\Omega_{\rm v}$ with $\Omega_\Lambda = \Lambda/3H^2$. Under that assumption and using the current density parameters, we can re-write the first Friedman equation (Equation (1.2))

$$\frac{k}{R_0^2} = H_0^2\left(\Omega_{\rm m} + \Omega_{\rm r} + \Omega_\Lambda - 1\right). \tag{1.7}$$

Given the equations presented in this sub-section, and with knowledge of the parameters H, Ω_m, Ω_r, and Ω_Λ, the evolution of the Universe can be extrapolated, both forwards and backwards in time, meaning the Universe is deterministic.

1.2 Standard Model

The current most widely accepted cosmological model is ΛCDM, so called because the energy content of the Universe at present is dominated by a cosmological constant, Λ, and Cold Dark Matter (CDM). In this section, we discuss some of the major milestones which led to the acceptance of ΛCDM as the Standard Model.

By 1925, Vesto Slipher had measured the shift in spectral lines for about 40 galaxies [4], though at this time galaxies were often referred to as nebulae. Slipher found that, except for the local group, the spectral lines of these galaxies were redshifted. By 1929, Hubble had estimated distances for 24 galaxies [5]. He combined these estimated distances with the galaxies' redshifts and found a linear correlation—the more distant a galaxy, the higher its redshift, which points to an expanding Universe. Hubble's original plot shows this relationship and is reproduced in Figure 1.1. When these measurements were made, a galaxy's redshift was interpreted as its recessional velocity, but we now understand that these redshifts are a property of the expanding Universe.

Before the discovery of the Cosmic Microwave Background (CMB) by Arno Penzias and Robert Wilson in 1964 [6], there were two prevailing paradigms for the origin of the Universe, the steady state model and the Big Bang theory. Steady state model proponents included Herman Bondi, Thomas Gold [7], and Fred Hoyle [8]. This model represents the perfect cosmological principle in that there is neither a special location nor special time in the Universe. To account for an expanding Universe, matter must be continuously created in

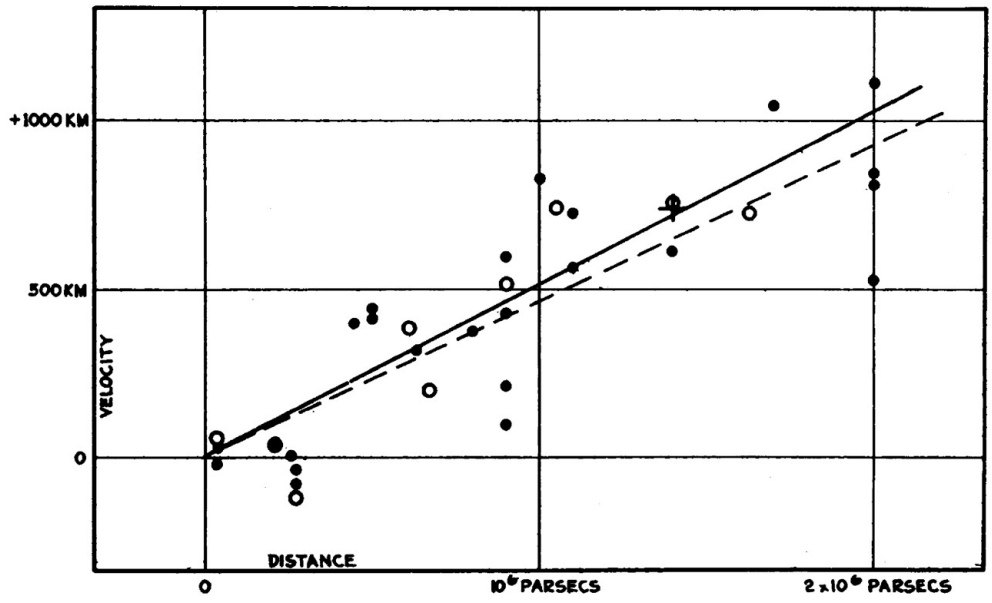

Figure 1.1: Hubble's diagram as he originally published it in 1929 [5]. The vertical axis shows measured radial velocities, so the units in the labels should be km/s, not km. The horizontal axis shows the estimated distances to the "nebulae" (galaxies). The plot shows that the more distant an object, the faster it appears to be receding from us. This apparent recessional velocity is now understood to be a property of the expanding Universe.

order to keep the density of the Universe constant. Conversely, the Big Bang theory does not require continuous creation of matter. Since we see an expanding Universe, the Big Bang theory postulates that at some point in the past, the Universe was much denser and hotter. At some time, the Universe would have been so hot and dense that a photon could not travel far before scattering off a free electron. Then, as the Universe cooled and electrons combined with protons, the density of free electrons became sufficiently low that photons could stream, uninhibited. We should now be able to detect those photons, albeit at a lower temperature than when they last scattered due to the expansion of the Universe. The CMB is made up of those photons, and since its detection, the Big Bang theory has been widely accepted as the theory explaining the evolution of the Universe [4].

An image of the CMB temperature sky is shown in Figure 1.2. This is a result of the European Space Agency's *Planck* satellite mission and was measured in a band centered at 143 GHz [9]. The mean temperature, Milky Way galaxy signal, and dipole induced by Earth's motion are subtracted in this map. Although the CMB frequency spectrum is well modeled as a black body with temperature 2.726 K, Figure 1.2 shows that it's not quite uniform. Comparing the color stretch of the map at the top of the figure, $\pm 300\ \mu$K, with the black body temperature, we see that the non-uniformity is small, around 1 part in 10^4 in the map.

For full-sky measurements, these temperature anisotropies can be expanded in spherical harmonics as

$$\frac{T(\hat{\mathbf{n}})}{T_0} = 1 + \sum_{\ell=1}^{\infty} \sum_{m=-\ell}^{\ell} a^T_{\ell m} Y_{\ell m}(\hat{\mathbf{n}}), \tag{1.8}$$

where $T(\hat{\mathbf{n}})$ is the temperature anisotropy field as a function of position $\hat{\mathbf{n}}$ on the unit sphere, T_0 is a normalization constant, the $Y_{\ell m}$ are the spherical harmonics, and the $a^T_{\ell m}$ are their

coefficients. When collapsing over the m-modes, we arrive at the power spectrum C_ℓ^{TT}

$$C_\ell^{TT} = \frac{1}{2\ell+1} \sum_{m=-\ell}^{\ell} \left(a_{\ell m}^{T*} a_{\ell m}^{T} \right). \tag{1.9}$$

Often, the CMB angular power spectra are plotted in D_ℓ^{TT}, where

$$D_\ell^{TT} \equiv \frac{\ell(\ell+1)}{2\pi} C_\ell^{TT}. \tag{1.10}$$

The bottom of Figure 1.2 shows the angular power spectrum of the temperature anisotropies with the best fit ΛCDM model.

1.3 CMB **Polarization**

In addition to the temperature anistropies (and because of them), the CMB is naturally polarized since it is the result of the last scattering of photons off free electrons through Thomson scattering. As shown in Figure 1.3, a quadrupolar temperature anisotropy is necessary to induce a net polarized signal in the CMB. We can express the polarization of a photon traveling in the z-direction through the following two electric field vectors:

$$E_x = a_x \cos\left(wt - \xi_x\right) \tag{1.11}$$
$$E_y = a_y \cos\left(wt - \xi_y\right). \tag{1.12}$$

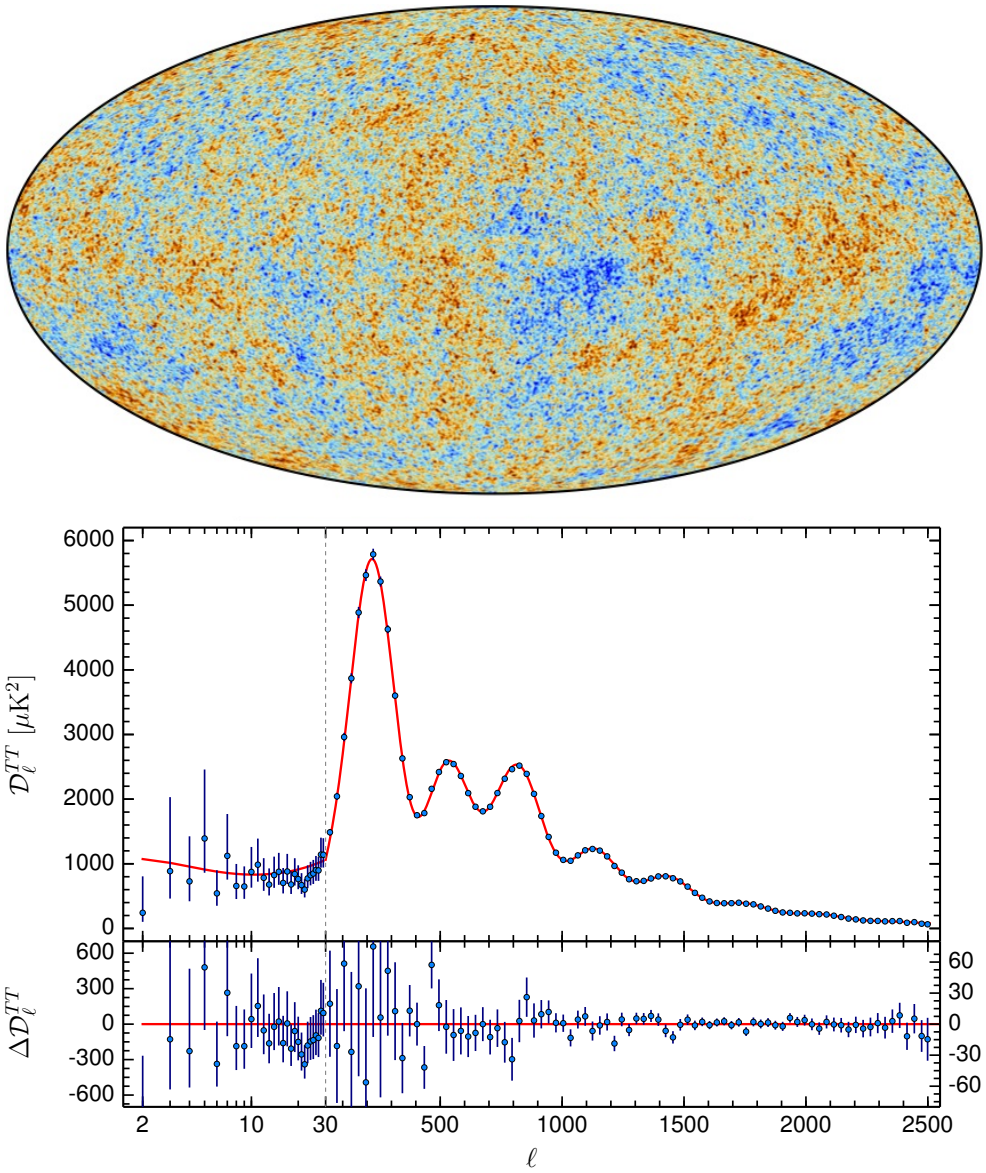

Figure 1.2: *Top*: Temperature anisotropies of the CMB as measured by the *Planck* satellite at 143 GHz. The color stretch in this image is ± 300 μK, showing that the anisotropies are at a level of ~ 1 part in 10^4 with respect to the mean CMB temperature. *Bottom*: Angular power spectrum of the map. Larger ℓ correspond to smaller angular scales. The underlying red line shows the best fit ΛCDM model, and the bottom panel shows the residual of the data points to that model. This map and spectrum are taken from the *Planck* 2015 results paper I [9].

Equations (1.11) and (1.12) can be represented through the four Stokes parameters:

$$I = a_x^2 + a_y^2 \tag{1.13}$$
$$Q = a_x^2 - a_y^2 \tag{1.14}$$
$$U = 2a_x a_y \cos\left(\xi_x - \xi_y\right) \tag{1.15}$$
$$V = 2a_x a_y \sin\left(\xi_x - \xi_y\right), \tag{1.16}$$

where I is the temperature intensity, Q and U are the linear polarizations, and V is the circular polarization. Thomson scattering doesn't produce circular polarization, and in practice we only measure I, Q, and U with the BICEP and *Keck* family of telescopes.

Q and U are spin-two quantities, and their values depend on the coordinate system used. If the coordinate system is rotated, Q and U will change, even though the measured polarization pattern is unchanged. We would instead like to express the CMB polarization in spin-zero quantities that form a rotationally invariant basis [10, 11]. These are called E (curl-free) and B (divergence-free), and the conversion from Q and U is easily performed in Fourier space:

$$E(\ell_x, \ell_y) = +Q(\ell_x, \ell_y)\cos(2\phi) + U(\ell_x, \ell_y)\sin(2\phi) \tag{1.17}$$
$$B(\ell_x, \ell_y) = -Q(\ell_x, \ell_y)\sin(2\phi) + U(\ell_x, \ell_y)\cos(2\phi), \tag{1.18}$$

where we've assumed a flat-sky and where $\phi = \arctan(\ell_x/\ell_y)$. Just as with temperature, we can calculate the angular power spectrum of the E-modes and B-modes (see Equation (1.9)).

Figure 1.4 shows the measured power spectra of the CMB for temperature (TT), E-modes, and B-modes on a logarithmic scale. We've already mentioned that the CMB temperature anisotropies are a factor of 10^4 smaller than the mean CMB temperature in the map; Figure 1.4 highlights that the polarization anisotropies, dominated by E-modes, are smaller but significant. At multipoles larger than $\ell \sim 500$, the E-modes account for about

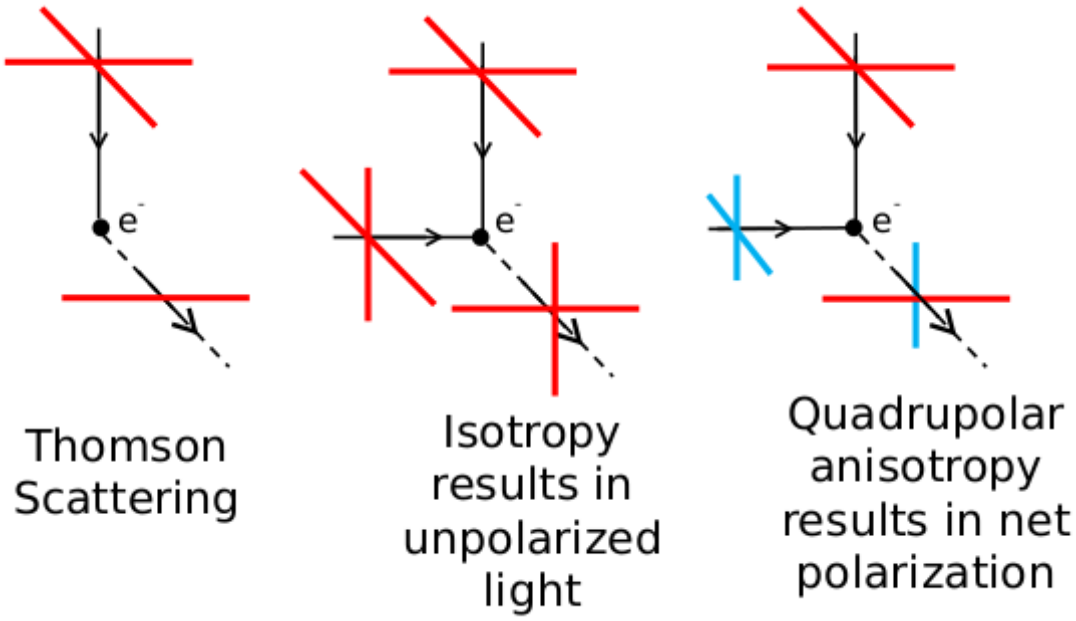

Figure 1.3: *Left*: Unpolarized radiation scatters 90° off a free electron through Thomson scattering and is polarized. *Middle*: When an electron is in an isotropic bath of radiation, the net result in unpolarized light. *Right*: When there is a quadrupole temperature anisotropy, for instance with hotter photons from the top and colder photons from the left, the net result is partially polarized radiation. Figure courtesy of Sarah Kernasovskiy [12], and the quadropolar anisotropy representation appears to be an adaptation of Hu and White [13].

10% of the CMB temperature anisotropies in the map (a factor of 1 part in 100 in the power spectrum).

The CMB photons we see today have traversed a Universe that is rich in structure. In particular, the gravitational potentials of large scale structure have deflected these photons along the line of sight. This deflection distorts both the temperature and polarization anisotropies of the CMB, converting some E-modes to B-modes [14]. These so-called lensing B-modes have been measured by SPT [15], POLARBEAR [16], and ACTPol [17] at small angular scales and BICEP2/*Keck* [18] at larger angular scales. Figure 1.4 includes these measurements and the expectation values for the lensing B-modes. Note that the B-modes are a factor 100 smaller than the E-modes (in power), placing stringent requirements on the ability to separate E- and B-modes.

1.4 Inflation

Although ΛCDM cosmology describes the evolution of the Universe, it requires initial conditions that aren't explained in the paradigm. Given the finite age of the Universe and the finite speed of light, information can not have been transferred between locations in the Universe located on opposite sides of the sky; they are causally disconnected. In fact, during the era of last scattering, the Universe was only old enough that areas encompassed in $\sim 1^\circ$ patches, as seen today, could have been causally connected. How then is the CMB so uniform in temperature? The preceding is referred to as the horizon problem, where the "horizon" is the farthest extent from which light could have been received in any direction around a given point.

Also, the Universe at present times is shown to be close to flat. Taking into account that a Universe which is originally flat, or nearly so, evolves away from flatness, the current

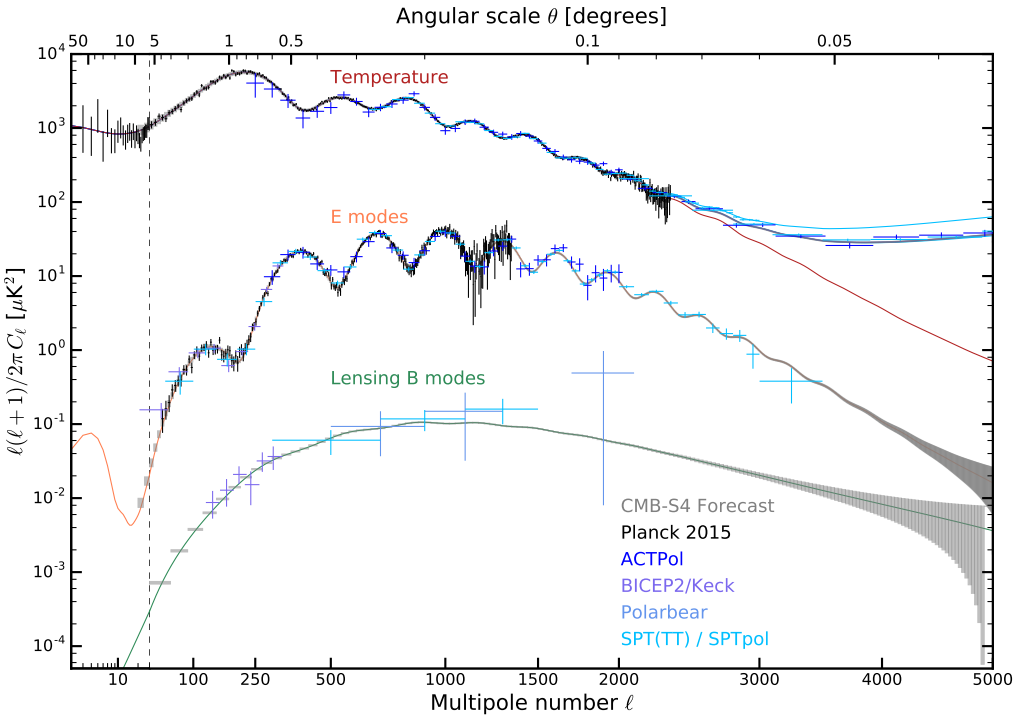

Figure 1.4: From top to bottom, the power spectra of the CMB temperature, *E*-mode, and lensing *B*-mode anisotropies. This figure is taken from the CMB-S4 Science Book, First Edition [19]

observations imply that the Universe's initial geometry must have been extraordinarily flat. This is a problem of fine-tuning and is referred to as the flatness problem.

In 1981, Alan Guth proposed the theory of inflation [20] to solve these and other problems. Although there are currently many inflationary theories, the basic postulate is that the Universe expanded exponentially in the first tiny fraction of a second. This solves the horizon problem because a small patch of the Universe which would have been in causal contact was expanded by such a scale that it has not yet reentered our horizon. Likewise, if the overall geometry of the Universe before inflation were not flat, the exponential expansion would have made our section of the Universe appear very close to flat. This solves the flatness problem. In addition to these classic examples of inconsistencies, inflation also naturally provides the seeds for structure formation by expanding quantum fluctuations to macroscopic scales.

A consequence of inflation is the creation of gravitational waves. These gravitational waves are at a much larger scale than can be detected with today's direct detectors (e.g., Advanced LIGO [21], Advanced Virgo [22], and MiniGRAIL [23]), but they would have left an imprint in the polarization of the CMB as B-modes. It is that signal, the imprint of gravitational waves, that the BICEP and *Keck* experiments are designed to measure.

1.5 Polarization Rotation

It's possible for the polarization direction of light to rotate as it propagates. Two mechanisms for polarization rotation are Faraday rotation and birefringence. Faraday rotation arises when

polarized light encounters a magnetic field within a medium. The rotation angle Ψ is

$$\Psi \propto \lambda^2 \int n_e B_{\parallel} dl, \tag{1.19}$$

where λ is the wavelength of light, n_e is the thermal electron density of the medium, and $B_{\parallel}$ is the strength of the magnetic field in the direction of propagation [24]. From this equation, we can see that Faraday rotation is frequency-dependent and is cumulative over distance. An astrophysical scenario for Faraday rotation is shown in Figure 1.5.

In contrast, birefringence occurs when the index of refraction in a material (typically a crystal) depends on both the polarization and propagation directions of light [25]. The result is a rotation of linearly polarized light except in the special case where the light propagates parallel to the optical axis of the crystal.

1.5.1 Cosmic Polarization Rotation

A tenet of the standard model in particle physics is CPT invariance, meaning that the product of charge conjugation (C), parity transformation (P), and time reversal (T) is conserved. In 1956, Lee and Yang proposed experiments which could settle the debate on whether or not there is violation of parity in the weak sector [26]. In 1957, Wu and team showed that parity is indeed violated by observing the anisotropies of electrons coming from the β-decay of polarized cobalt-60 nuclei [27]. In 1964, Christenson et al., demonstrated that the weak sector also includes CP violation [28]; the K_2^0 decays to two pions but with unequal probability. Despite these known violations, there are currently no measurements of CPT violation, but there are models of the Universe which predict this violation. Such models produce what is commonly called "cosmic birefringence," an effect which rotates linearly polarized light over cosmological distances.

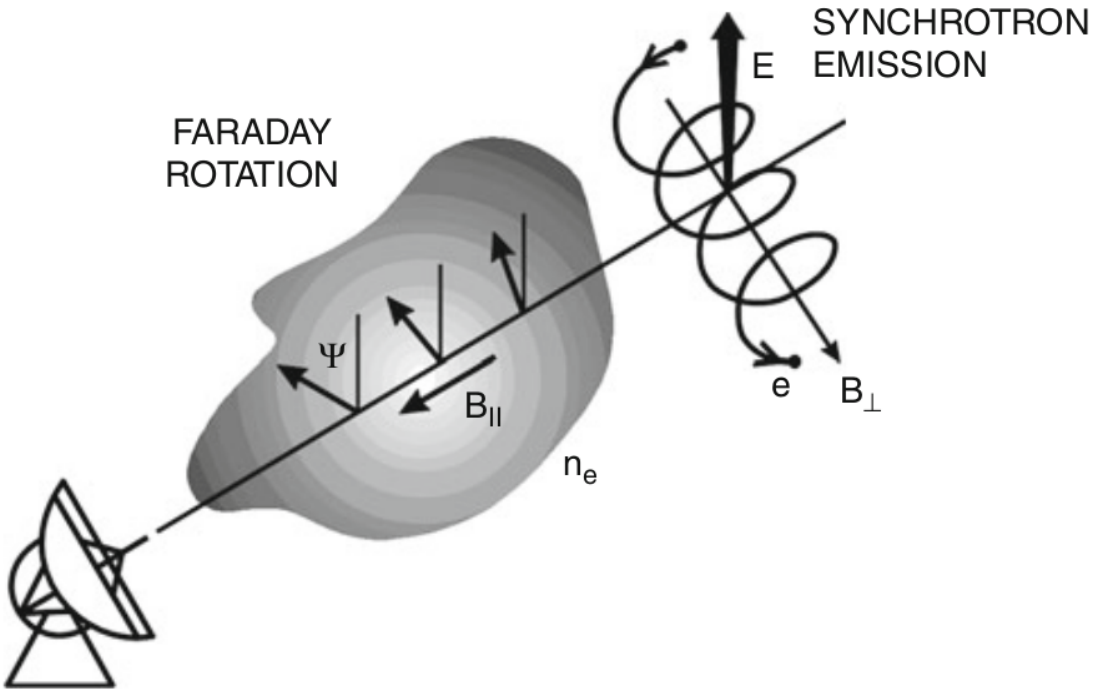

Figure 1.5: Cartoon representation of Faraday rotation. In this figure, the source of polarized light is synchrotron radiation. As the light propagates through a magnetic field aligned with some strength in the direction of propagation, the polarization axis of the light is rotated. This figure is taken from chapter 13 of "Planets, Stars and Stellar Systems" [24]

There are many models which can produce a cosmic birefringence effect, but we will not present them all in this dissertation. Contreras et al., [29] and references therein, contain a fairly comprehensive list of the various models. In this dissertation we will explore one way to produce a birefringent Universe, which is to add a Chern-Simons term [30, 31, 32, 33, 34, 35] to the Maxwellian Lagrangian in the form

$$\mathcal{L} \supset \frac{a}{2f_a} F_{\mu\nu} \widetilde{F}^{\mu\nu}, \tag{1.20}$$

where a is a pseudoscalar field, f_a is the coupling constant, $F_{\mu\nu}$ is the electromagnetic field, and $\widetilde{F}^{\mu\nu}$ is the dual (see e.g., [36] and references therein). The effect of adding the Chern-Simons term is that left- and right-circularly polarized light travel at different velocities. Because linearly polarized light can be decomposed into left- and right-circularly polarized light, this difference in velocities causes the CMB linear polarization to rotate by an angle $\Delta\alpha$ in this model:

$$\Delta\alpha = \frac{\Delta a}{f_a}, \tag{1.21}$$

where Δa is the change of the pseudoscalar field along the photon's propagation direction (e.g., [32]). Note that this model would create a uniform polarization rotation of the CMB across the entire sky independent of frequency, which means it's unlike both Faraday rotation and classic birefringence.

1.5.2 Measuring the Rotation Angle

Measuring a polarization rotation angle such as that in Equation (1.21) would indicate a violation of Lorentz invariance and CPT symmetry [37], both of which would inform us

of new and tantalizing physics. Since the rotation angle accumulates over distance, we would like to observe distant objects, for instance radio galaxies and quasars. Because polarized light is sourced by synchrotron radiation in radio galaxies and quasars, the intrinsic polarization angle of light in these can be deduced by the orientation of their double lobes [38]. The radio sources used in measuring cosmic polarization rotation are at redshifts $z < 1$. However, it would be better to observe more distant sources. This has been done using the polarized ultraviolet (UV) light from radio galaxies at redshifts $2 \lesssim z \lesssim 4$, which is observed in the optical regime due to redshifting [39].

The most distant source available is the CMB, so it should have accumulated the largest $\Delta\alpha$. The presence of a uniform rotation angle, no matter the source, affects the observed CMB power spectra. They become

$$C_\ell^{TE,\mathrm{obs}} = C_\ell^{TE}\cos(2\Delta\alpha) \tag{1.22}$$
$$C_\ell^{TB,\mathrm{obs}} = C_\ell^{TE}\sin(2\Delta\alpha) \tag{1.23}$$
$$C_\ell^{EE,\mathrm{obs}} = C_\ell^{EE}\cos^2(2\Delta\alpha) + C_\ell^{BB}\sin^2(2\Delta\alpha) \tag{1.24}$$
$$C_\ell^{BB,\mathrm{obs}} = C_\ell^{EE}\sin^2(2\Delta\alpha) + C_\ell^{BB}\cos^2(2\Delta\alpha) \tag{1.25}$$
$$C_\ell^{EB,\mathrm{obs}} = \frac{1}{2}\left(C_\ell^{EE} - C_\ell^{BB}\right)\sin(4\Delta\alpha), \tag{1.26}$$

where the C_ℓ are the theoretical spectra before rotation and the C_ℓ^{obs} are the spectra measured at the telescope after any uniform rotation is applied [40]. These equations apply to a generic cosmology, which is the reason the C_ℓ^{BB} terms are retained. In ΛCDM, however, BB is initially 0, consistent with current measurements, so we are free to remove the C_ℓ^{BB} terms. Figure 1.6 shows the TB and EB spectra in ΛCDM under a range of rotation angles according to Equations (1.23) and (1.26). If $\Delta\alpha = 0$, then the TB and EB spectra are 0 at all multipoles.

Table 1.1 shows the measured values of $\Delta\alpha$ from several CMB experiments, and Table 1.2

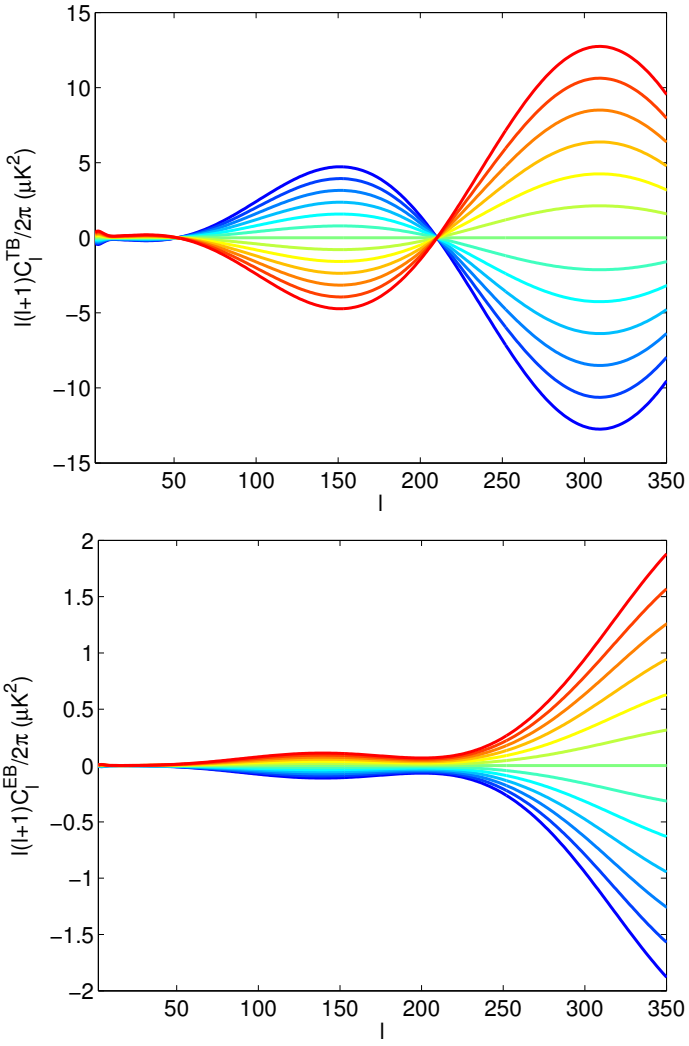

Figure 1.6: ΛCDM Power spectra for TB (top) and EB (bottom) after applying polarization rotations between -5° (blue) and +5° (red), in 1° increments.

Table 1.1: Measurements and uncertainties (statistical and systematic) on cosmological birefringence from CMB experiments. The BOOMERANG results are from an analysis which used a Gaussian prior on the systematic rotation of -0.°9±0.°7, which is the reason the table only includes a statistical uncertainty [41]. This table is adapted from Galaverni, et. al [39].

Experiment	Frequency (GHz)	$\Delta\alpha\pm$ stat ($\pm$ syst) (deg)
WMAP9	53	-0.36±1.24 (±1.5) [42]
BOOM03	145	-4.3±4.1 [41]
BICEP1	100	-2.27±2.04 (±1.3) [43]
BICEP1	150	-2.91±1.05 (±1.3) [43]
QUAD	100	-1.89±2.24 (±0.5) [44]
QUAD	150	0.83±0.94 (±0.5) [44]

Table 1.2: Measurements and uncertainties on cosmological birefringence from CMB, UV radiation from radio galaxies, and radio sources (galaxies and quasars). This table is adapted from Galaverni, et. al [39]

Experiment	Mean Redshift	$\Delta\alpha\pm$ uncertainty (deg)
CMB	1090	-0.36±1.29
UV Radio Galaxies	2.62	0.7±2.1
Radio Sources	0.47	1.6±1.8

summarizes the average measured values of $\Delta\alpha$ for the CMB, UV radio galaxies, and radio sources.

If the pseudoscalar field, a from Equation (1.20), is not homogeneous but a function of position on the sky, then the rotation angle from cosmic birefringence will also be a function of sky position. BICEP2/*Keck* [45] and *Planck* [29] data have recently been used to place upper limits on anisotropic rotation, characterized by the parameter A_{CB}. This parameter is the rotation power spectrum amplitude defined by

$$\frac{L(L+1)}{2\pi}C_L^{\alpha\alpha} = A_{CB} \times 10^{-4}, \tag{1.27}$$

where the units are rad^2. The limits from BICEP2/*Keck* and *Planck* are $A_{CB} \leq .33$ and

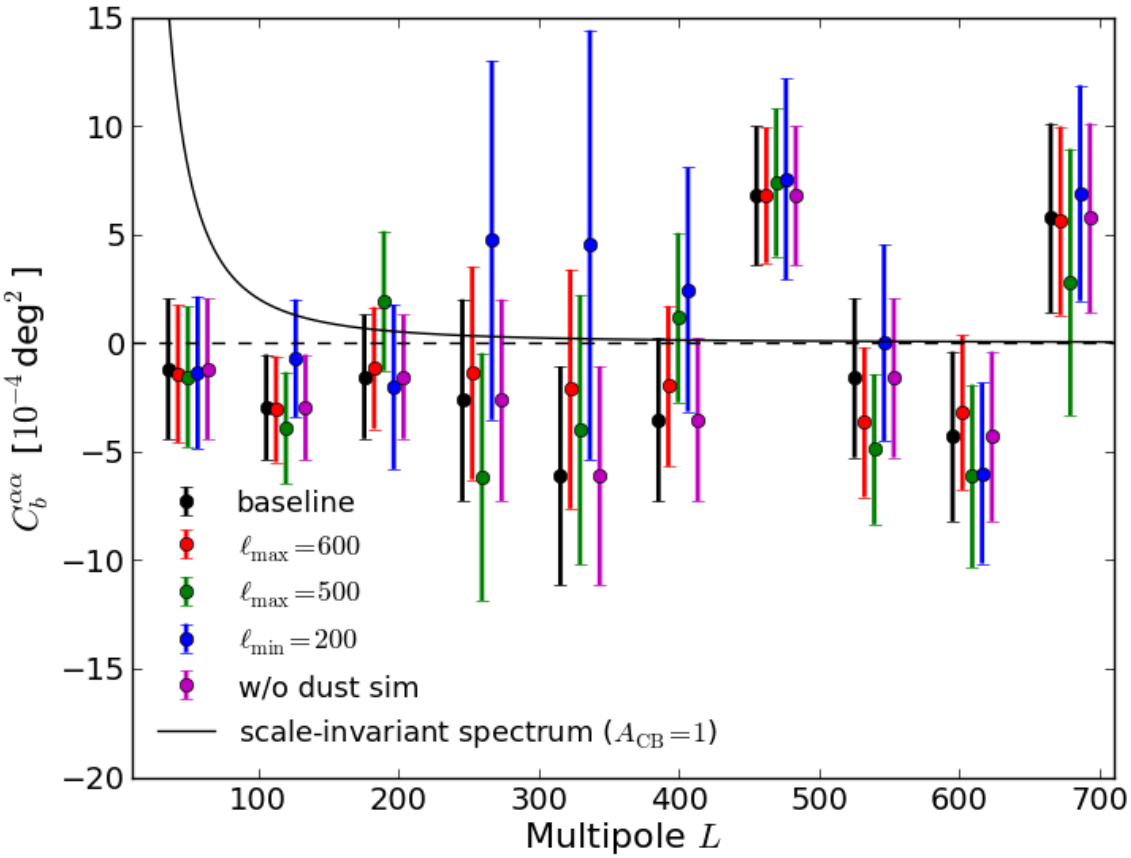

Figure 1.7: Angular power spectrum of rotation anisotropies using BK14 data. The data points are from real data, and the uncertainties are from our standard ΛCDM+noise+dust simulations. Different colored points are derived from alternative subsets of multipole bins. This figure is taken from BICEP2/*Keck Array* IX [45].

$A_{CB} \leq .29$, respectively. The anisotropic rotation power spectrum for the BICEP2/*Keck* data is shown in Figure 1.7.

The main goal of this dissertation is to improve on the systematic uncertainty listed in Table 1.1 to fully exploit the very low statistical uncertainty that is becoming possible with the BICEP2/*Keck* measurements.

Chapter 2

BICEP/*Keck Array* EXPERIMENTS

2.1 BICEP*Keck* History

We are guided in our telescope design decisions by our ambition to detect an inflationary *B*-mode signal. We have used the same basic guidelines for BICEP1 (observed 2006-2008) [46], BICEP2 (observed 2010-2012) [47], *Keck Array* (began observing 2012) [48], and BICEP3 (began observing 2015) [49]. Starting with BICEP2, we've used transition edge sensor (TES) detectors to measure the CMB photons. In Figure 2.1, we show the family of experiments, starting with BICEP2 and going through BICEP Array, which is currently in development. This figure also shows the progression of the focal plane sizes. In this chapter we discuss the telescope design, detectors, observing site, observation strategy, and observation frequencies.

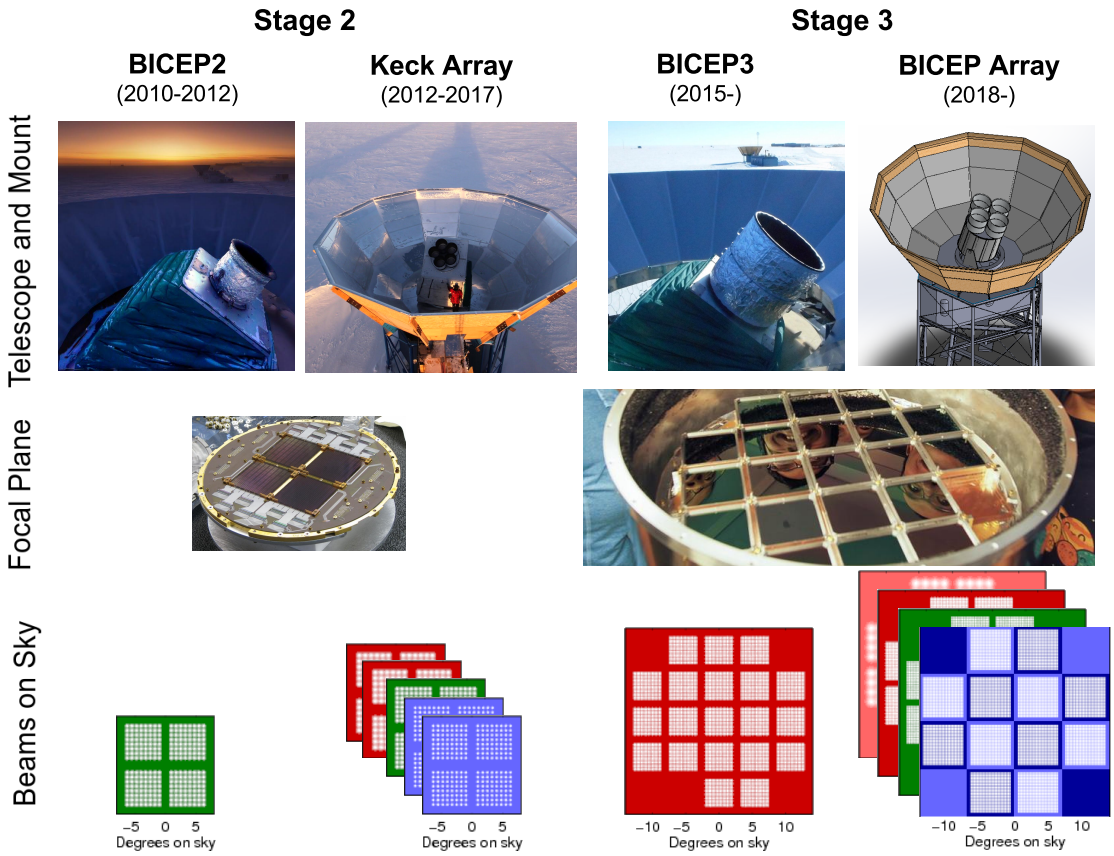

Figure 2.1: The sequence of the BICEP/*Keck* collaboration CMB experiments. BICEP1, which used a different detector technology, is not pictured, and BICEP Array is in the design phase. Fields of view and beam sizes are shown in relative proportion along the bottom of this figure. The beam sizes decrease toward higher observing frequency and with the larger aperture of the stage 3 telescopes (BICEP3 and BICEP Array). This figure is courtesy of the BICEP2 and *Keck* Collaborations.

2.2 Experimental Approach

2.2.1 Small Aperture

The *Keck Array* and BICEP telescopes are designed to target B-modes from primordial gravitational waves. The signal is expected to peak at $\ell \approx 100$, or 2 – 4 degrees. The theoretical diffraction limit for a telescope is given by

$$\theta = \frac{1.22\lambda}{D}, \tag{2.1}$$

where θ is an angle in radians, λ is the observation wavelength, and D is the aperture size. For the lowest frequency observed with the *Keck Array*, 95 GHz, a diffraction limited telescope must have a minimum diameter of 11.2 cm to resolve points on the sky separated by 2°. The aperture of the *Keck Array* telescopes is 26.4 cm.

While a larger telescope can of course resolve the theoretical primordial B-mode signal, our small apertures offer several advantages. Our telescope mounts have a third axis which rotates the telescopes about the boresight, which we call the "deck" axis. By observing at multiple deck angles, we get a cancellation of a class of systematics that leak temperature anisotropies to polarization anisotropies or mix between E-modes and B-modes. Second, the small aperture allows installation of a comoving absorptive baffle. The detectors' side lobes couple to non time varying radiation from the baffle instead of galactic emission or ground pickup. Third, the smaller telescope is easier to surround by a ground shield. The ground shield prevents radiation from the relatively hot ground from entering the telescope optics unless it's refracted at least twice. Figure 2.2 shows a cross section of the *Keck Array* mount and ground shield, depicting the comoving baffles, the drum (which carries the cryostats), and the three rotation axes. A picture of the real *Keck* mount and groundshield is shown in

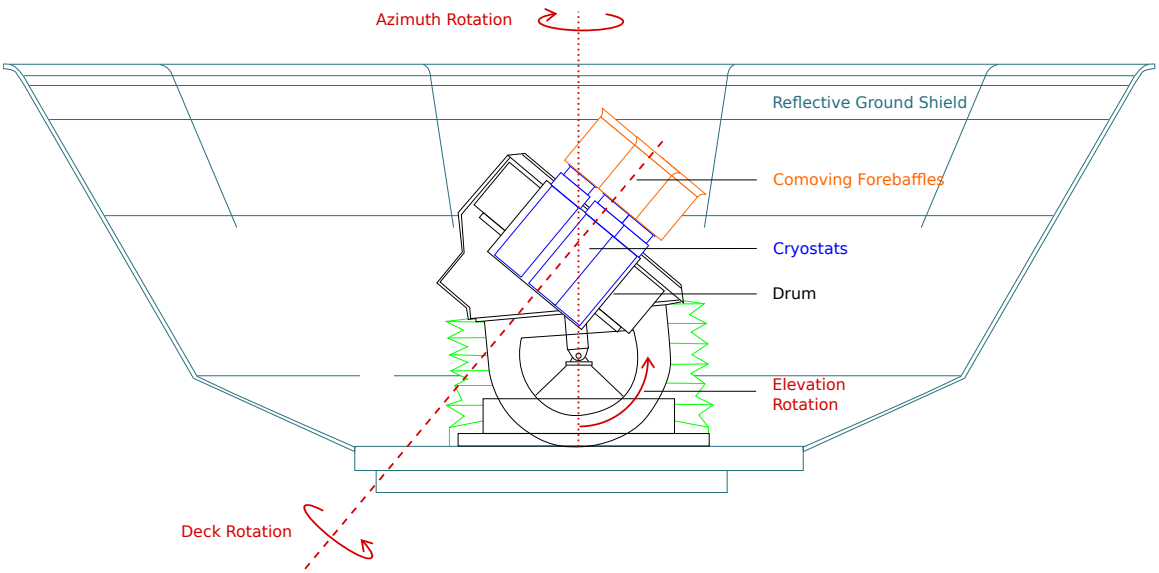

Figure 2.2: Cross section of the *Keck Array* mount and reflective ground shield. The "drum" of the telescope is a cylinder the five cryostats are attached to. In addition to Azimuth and Elevation, the drum can rotate about the boresight, called "deck" rotation. This figure is modified from BICEP2/*Keck Array* IV [48].

the top row of Figure 2.1.

2.2.2 Observing Region

All BICEP and *Keck* telescopes have targeted $\sim 1\%$ of the sky centered at RA 0h, Dec -57.5, a region expected to be low in polarized foregrounds (dust and synchrotron) since the total intensity is also lower than typical. In cross correlation with *Planck* [18], the polarized signal of foregrounds was found to be higher than expected. *Planck* released a paper which indicated there may be regions of the sky with lower polarized foreground contamination [50]. Upon reanalysis of the *Planck* data, using a different data split, we find the results to be less certain. This is summarized in Figure 2.3, which shows that the very cleanest regions in the original analysis are not present in the reanlaysis. We therefore continue to observe the same

region since there's not sufficient evidence for better patches of sky and since we've already observed this region very deeply at 150 GHz (and more recently at 95 GHz).

2.2.3 The Telescopes

In Figure 2.4 cross sections of the *Keck* and BICEP3 cryostats are shown. The two cryostats are similar. Both are on-axis two-lens refracting telescopes. Both use filters designed to block undesirable infrared radiation. Both use a pulse tube cryocooler to cool one radiation shell to $\sim$50 K and another shell to $\sim$4 K. A ^{4}He/^{3}He/^{3}He sorption refrigerator further cools the focal plane to $\sim$250 mK in both telescopes. Figure 2.5 compares the optical paths of the BICEP2/*Keck* and BICEP3 telescopes. It also labels the optical elements in the telescopes, showing the materials used for the filters and lenses in BICEP2/*Keck* and BICEP3.

2.2.4 The Detectors

To detect the faint polarized signal of the CMB, our experiments employ bolometers, essentially thermometers. The BICEP1 focal plane was composed of 49 pairs (25 at 100 GHz and 24 at 150 GHz) of "spiderweb" silicone nitride micromesh polarization-sensitive bolometers (PSBs) read out with neutron transmutation-doped germanium thermistors and fabricated at JPL [53, 54]. Behind each beam-forming feedhorn were co-mounted two of these PSBs, each sensitive to linear polarization in an orthogonal direction from the other. The noise of these detectors was dominated by photon shot noise from the atmosphere, which means we must do one or more of the following to increase sensitivity to the polarization of the CMB: (a) decrease the signal from the atmosphere by flying the detectors in a balloon or launching them into space, (b) observe for a longer time, or (c) use more detectors simultaneously. With BICEP2, we took the approach of "c," increasing the detector count nominally to 512

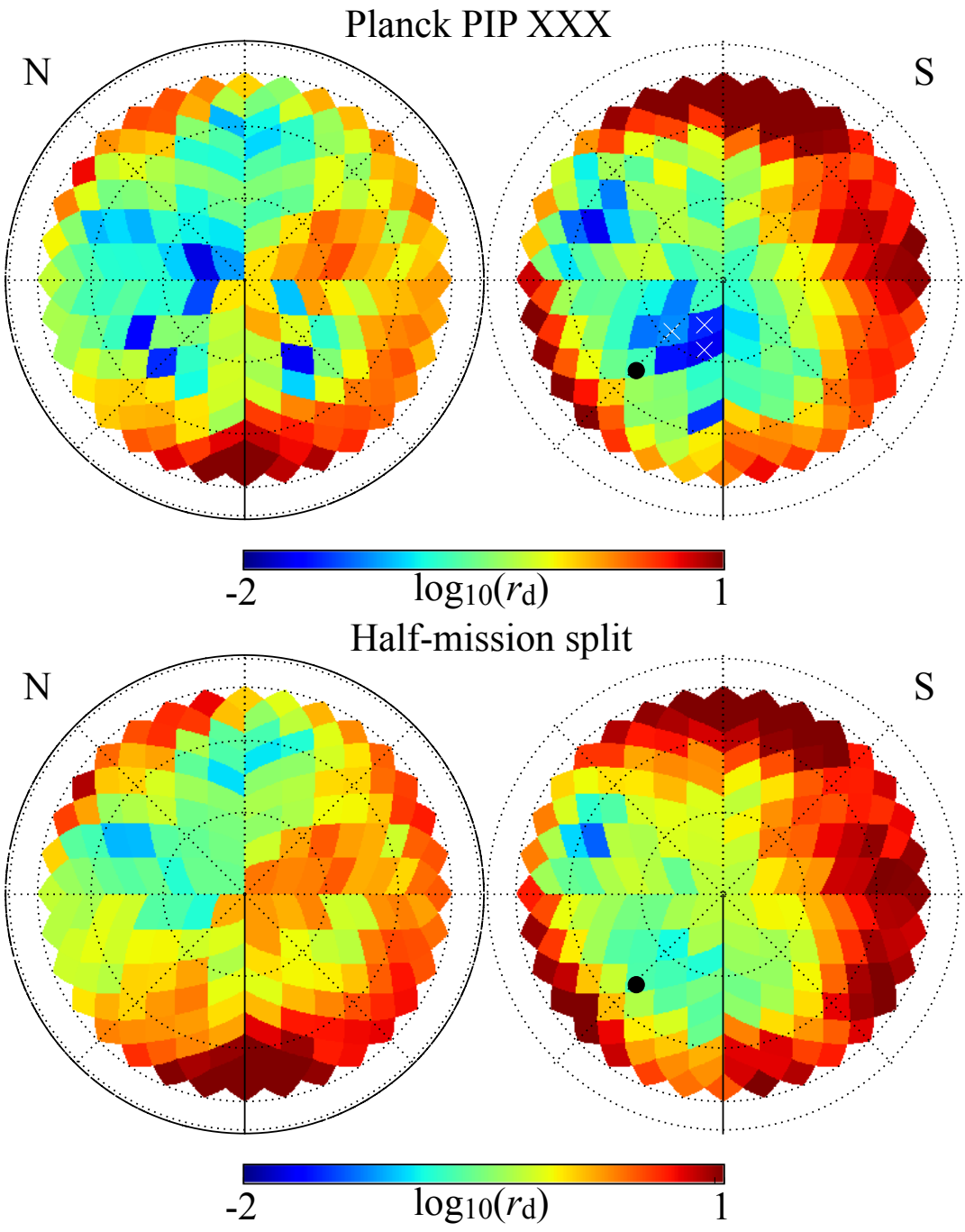

Figure 2.3: Level of polarized dust in patches across the sky shown as polar projections in galactic coordinates. *Top*: Analysis presented in *Planck* Collaboration Int. XXX [50] with the center of the BICEP field superimposed by a black dot. *Bottom*: Re-analysis showing a different split of *Planck* data. There is no clear evidence for a much cleaner patch of sky. This figure is courtesy of the BICEP2 and *Keck* Collaboration.

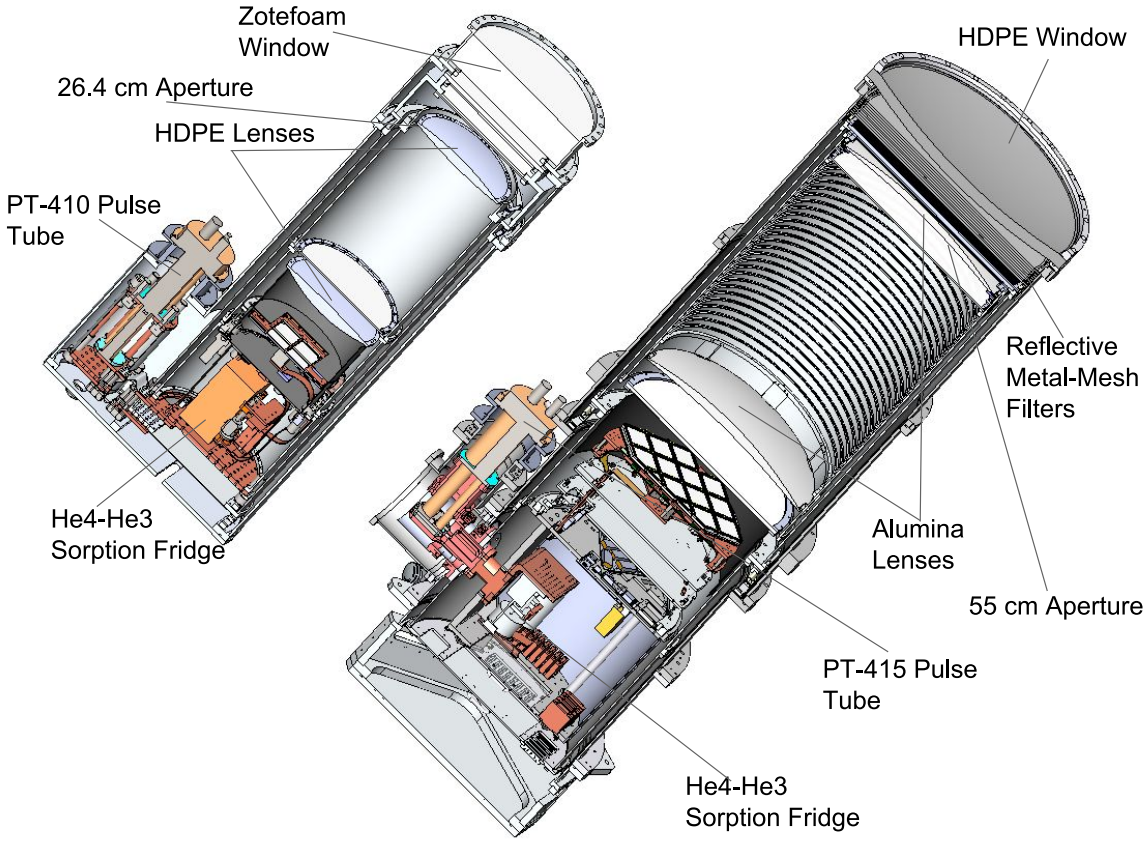

Figure 2.4: Cross sections of the *Keck* (left) and BICEP3 (right) cryostats. Both telescopes are two-lens refractors and have infrared-blocking filters. Both cryostats are cooled with pulse tube cryocoolers, and both focal planes are further cooled with a ^{4}He/^{3}He/^{3}He sorption refrigerator [51]. This figure is courtesy of the BICEP2 and *Keck* Collaboration.

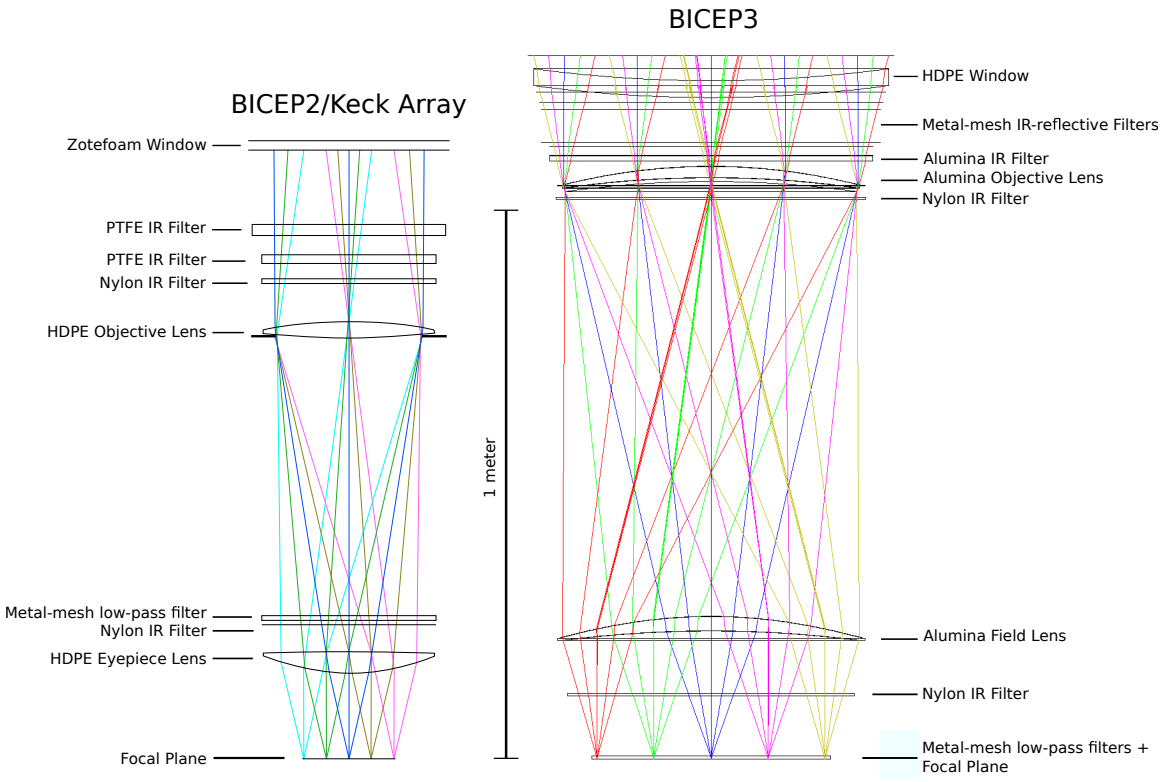

Figure 2.5: Optical chain of the BICEP2 and *Keck* telescopes (left) and BICEP3 telescope (right). This complete figure is taken from Karkare et al. [52]. A similar diagram for the BICEP2/*Keck Array* portion can be found in BICEP2/*Keck Array* IV [48].

(256 pairs) by switching to a radically different detector technology. Continuing on with the *Keck Array*, which is essentially BICEP2 cloned 5 times, we again use more detectors but also observe for a longer time. BICEP3 also takes the approach of "c" by placing the same number of detectors as in the *Keck Array* in one cryostat and observing concurrently with *Keck*, though at a different frequency.

The new detector technology used with BICEP2 and our successor experiments is fabricated at JPL [55] and is displayed in Figures 2.6 to 2.8. These transition edge sensor (TES) detectors are lithographically etched in arrays on a silicon wafer. Each pair of PSBs contain co-located grids of dipole antennas with orthogonal orientations. Each antenna feeds a microstrip line with a length chosen so that the waves constructively interfere to form a beam with finite angular extent. After combining the waves from the individual microstrip lines (which we call the summing tree), the signal is filtered with an on-board, three-pole, band-defining LC filter. Once filtered, heat is deposited in a resistive meander located on the TES island. The TESs, which are voltage biased to keep them on their superconducting-normal transition, are also heated. This increases their resistance, and the power, or current, through the biasing lines decreases. The change of current is detected through a series of superconducting quantum interference devices (SQUIDs). To record the signal outside of the cryostat, and to reduce the number of wires necessary, the SQUIDs are multiplexed in the time domain. Figure 2.9 shows an example of a TES readout schematic. In BICEP2 and *Keck*, the TES's couple to their own first stage SQUID (SQ1), and 33 SQ1's (16 detector pairs and one dark SQ1) couple to a single second stage squid (SQ2), which isn't shown in the figure. Each SQ2 is coupled to a SQUID Series Array (SSA) that provides further amplification of the detector signals. Because 33 SQ1's couple to a single SQ2, they are read out in sequence with a multiplexing (MUX) chip. Reading out an entire focal plane of

detectors requires multiple MUX chips. Each chip is referred to as a MUX column and each MUX column has 33 MUX rows (the SQ1's). A detailed discussion of these detectors can be found in a joint paper between the BICEP2, *Keck Array*, and SPIDER Collaborations [56].

2.2.5 Site

The *Keck Array* and BICEP experiments are located within 1 km of the geographic south pole at an elevation of 2800 m. There are several advantages to the south pole site:

- consistently dry atmosphere resulting in reduced atmospheric opacity;
- observation field always above horizon; and
- very little diurnal variation in temperature, most importantly sky temperature.

2.2.6 Observing Strategy

Starting with BICEP2, our observation aim was to observe a small patch of sky at a single frequency until we detected a B-mode signal. This strategy has been referred to as "relentless observation." The result of this strategy was the deepest CMB polarization map at 150 GHz, ever. Since we detected B-modes in our observation patch with three years of BICEP2 data [47], we have now moved into the strategy of observing the same patch of sky at multiple frequencies (see Section 2.3).

Although the details of observing this patch of sky have varied slightly through the years, the basic scanning method is largely unchanged since BICEP1. We begin with a partial load curve, which measures the shape of the super conducting–normal transition by stepping the detector biases from a value large enough to put the detectors in the normal range to 0. Then we perform a nod in elevation, "elnod" for relative gain calibration (see Section 3.1.2),

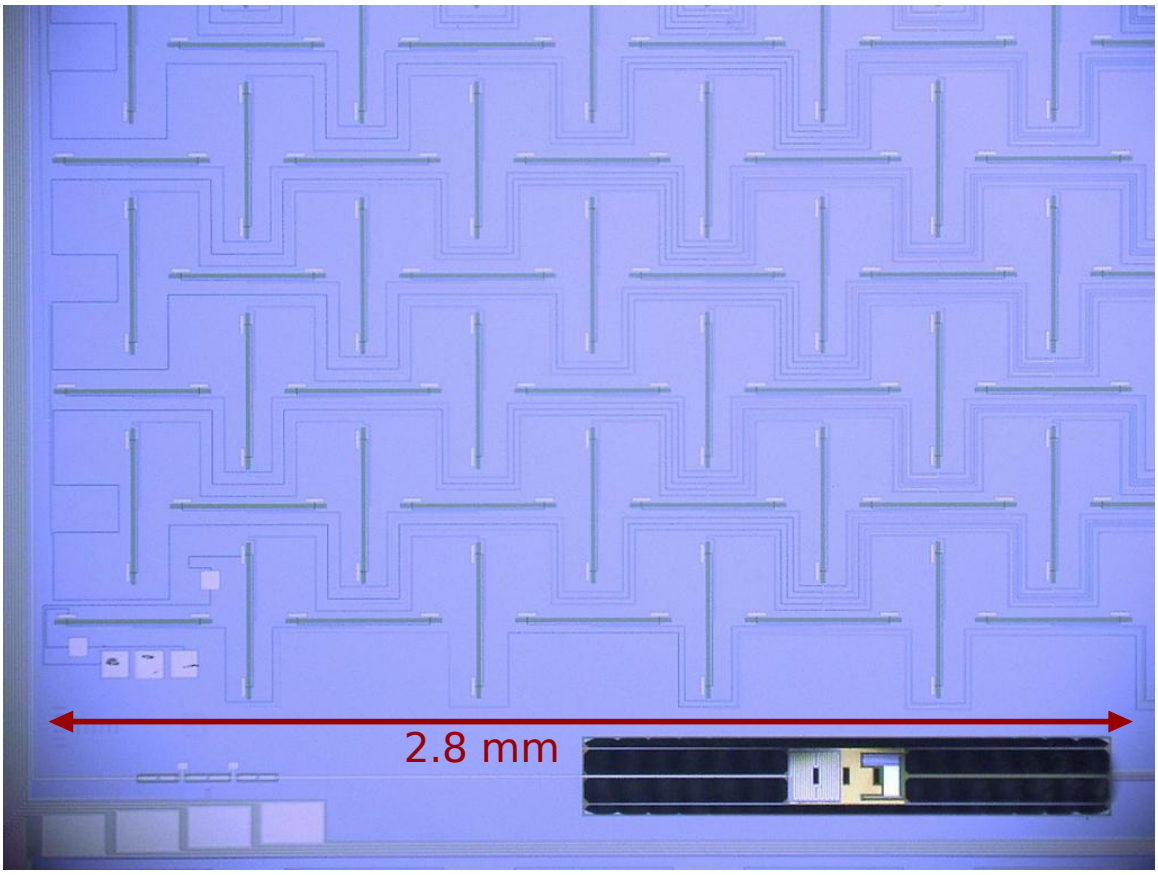

Figure 2.6: Portion of a detector pair. The signal from each slot antenna is transmitted through the microstrips, which are the lines weaving around the slots. The signals from all slots that are parallel are summed to synthesize a beam with one polarization. Once combined, the signal passes through a band-defining filter, shown toward bottom left, and then deposits energy on the TES island, shown at bottom right. The rest of the slots sum to synthesize a beam with orthogonal polarization and use a physically separate band-defining filter and TES island, neither of which are shown in this image. This figure is taken from BICEP2 Collaboration II [57].

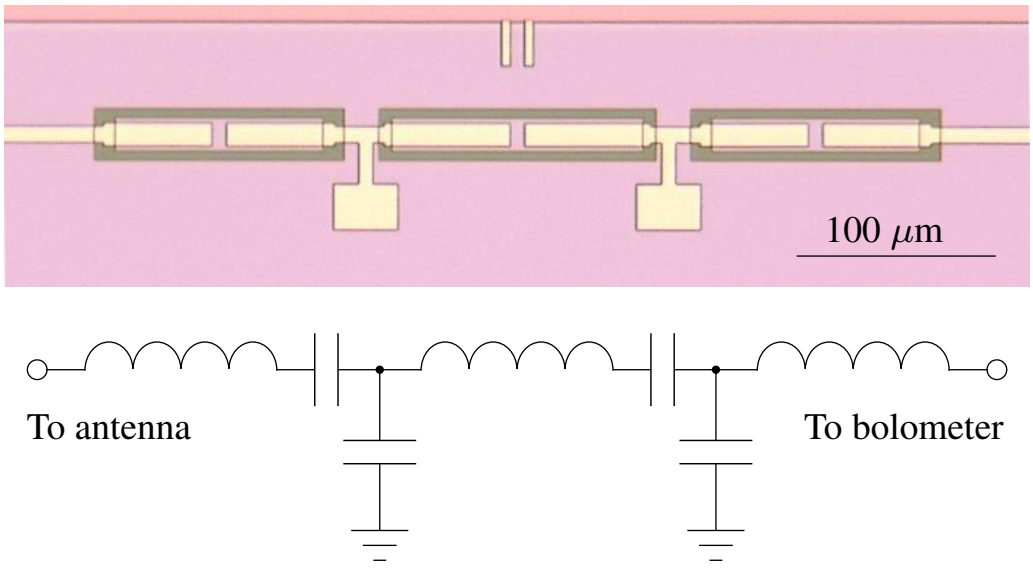

Figure 2.7: Microscope photograph of a band-defining filter. The circuit diagram is also shown. This figure is taken from BICEP2 Collaboration II [57].

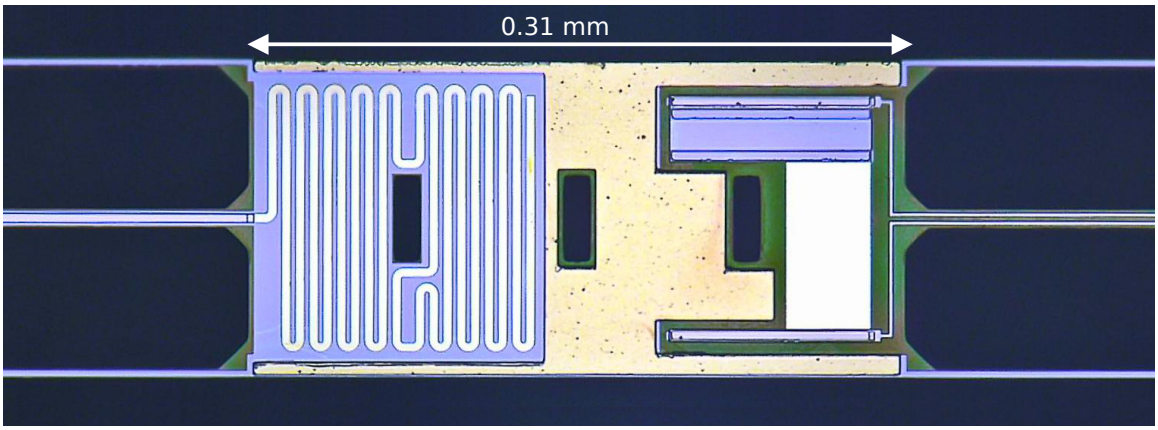

Figure 2.8: TES island for one detector. The island is lithographically etched so that six thin legs keep the TES suspended. After the signal is filtered (see Figure 2.7), it enters from the left and deposits power in the resistive meander, which heats the island. The TES is voltage biased through the microstrip line entering from right. Shown as two rectangles on the right are the titanium (blue) and aluminum (white) TESs. This figure is taken from BICEP2 Collaboration II [57].

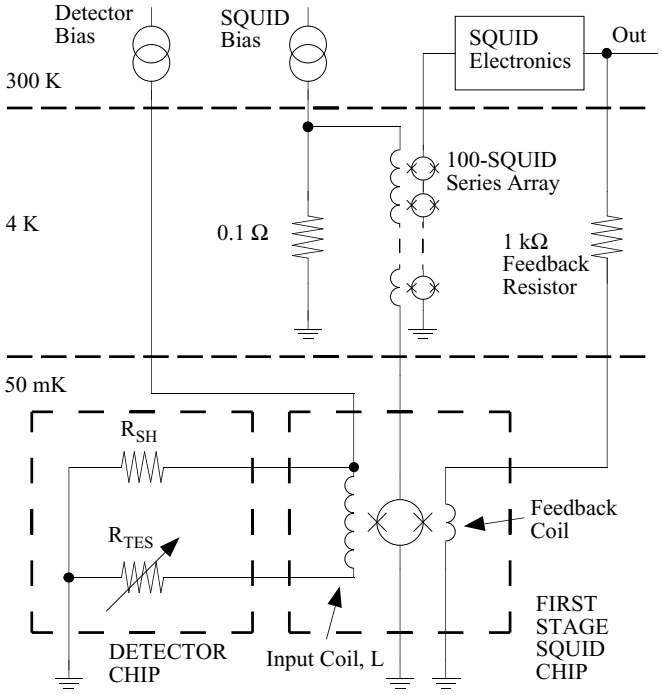

Figure 2.9: Example schematic of a TES detector readout. The TES detector is voltage biased with a bias current through the shunt resistor (R_{sh}) and is coupled to a first stage SQUID. In *Keck* there is a second stage SQUID before the SQUID Series Array. This figure is taken from Irwin and Hilton [58]

scan the telescope left and right between two azimuth limits and at a single elevation, and perform a second elnod. Each excursion between azimuth limits, either left- or right-going, is called a "halfscan," and the block of data between the first and second elnods is termed a "scanset." The length of the scanset varies, but is around 50 minutes. For much of the BICEP/*Keck* history, we've then stepped the telescope in elevation, usually by 0.°25, for the next scanset and scanned between another set of azimuth angles in order to observe the same patch of CMB. Beginning in 2015 for *Keck* and 2016 for BICEP3, we performed a second scanset between the same azimuth ranges and at the same elevation in order to reduce the number of sky modes filtered by ground subtraction (see Section 3.1.2).

Figure 2.10 shows a sample 2-day scanning pattern for *Keck* in 2017. In most cases, we break the scansets into subsets called "phases." The number of scansets in a phase varies but is typically 10. After two phases are complete, there is $\sim$7 hours left in the day. In *Keck*, this time is spent observing a portion of the galactic plane or recycling the refrigerator. When observing the galaxy, the azimuth limits and elevation are always changed between each scanset, which is shown between hours 17 and 24 in Figure 2.10. The length of an observation schedule is determined by the hold time of the refrigerator. BICEP2 had a 3-day schedule, *Keck* has a 2-day schedule, and BICEP3 moved from a 2-day schedule in 2016 to a 4-day schedule for part of 2017 and a 3-day schedule for the rest. After an observing schedule is complete, the telescope rotates to a new deck angle, and the process repeats. Although the elevations in the next schedule are not necessarily the same as the previous, the azimuth limits for the scansets are because their start times are tied to local sidereal time.

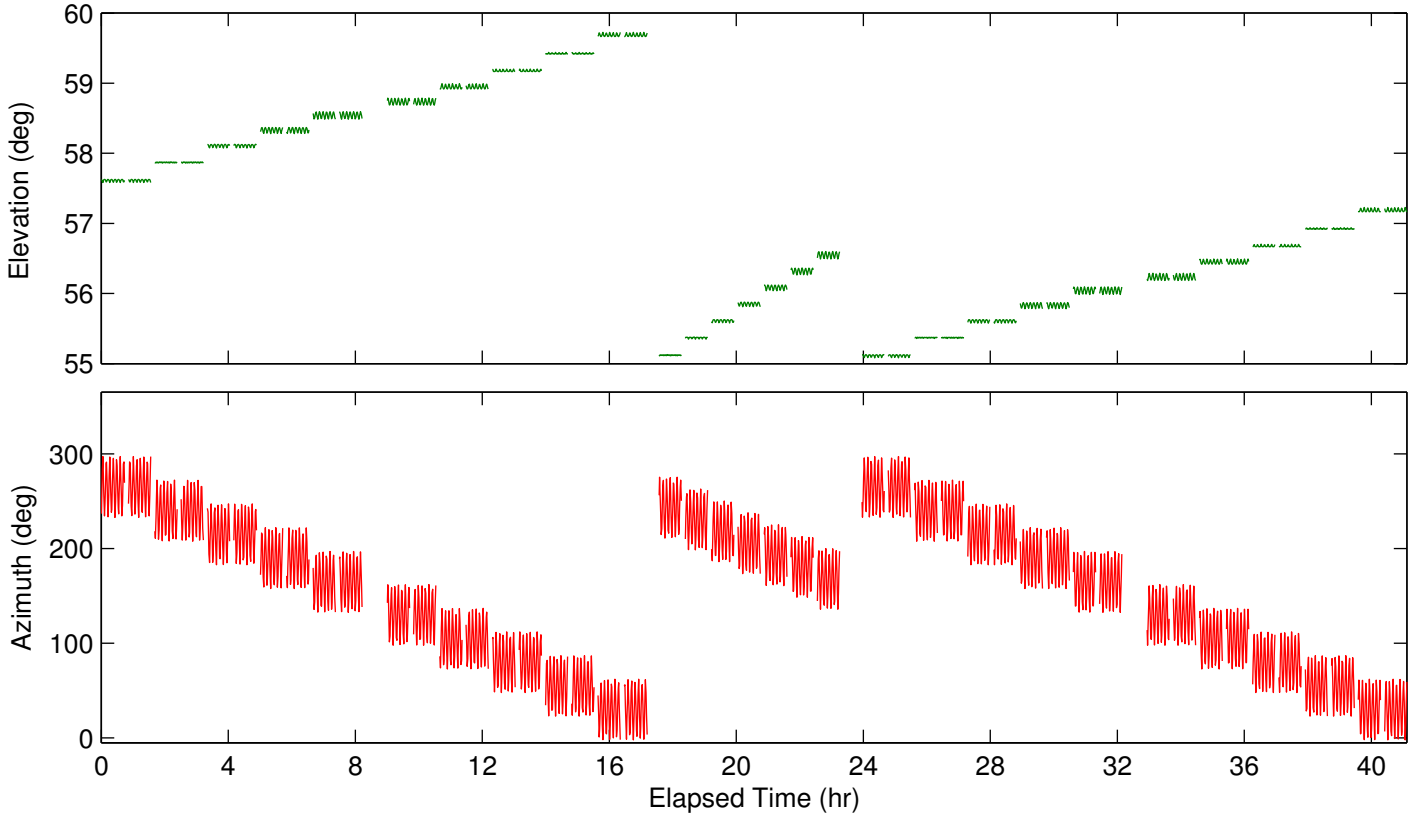

Figure 2.10: Example scanning pattern for a schedule used with *Keck* in 2017. The granularity of data points is one minute, and points are only shown when the telescope in scanning in Azimuth. *Top*: Elevation motion of the telescope. The width of the lines is due to the small tilt of the mount's azimuth axis with respect to the ground-fixed coordinates. *Bottom*: Azimuth motion of the telescope. The change in azimuth limits is to account for the rotation of the sky throughout the day.

2.3 Observing Frequencies

As shown in Figure 2.11, an optimal frequency for observing the CMB is near 100 GHz due to the expected contributions of foreground contamination from synchrotron radiation and warm dust. BICEP2 observed exclusively at 150 GHz, as did the *Keck Array* during its first two seasons. We now have a deep enough map at 150 GHz to detect a BB signal in excess of ΛCDM + gravitational lensing [47]. In order to distinguish between a cosmic signal and foreground contributions, we must observe the same patch of sky at multiple frequencies. This is effective because foregrounds have a different spectral signature. In CMB temperature units, the CMB spectrum has the same brightness at all frequencies, but a synchrotron component will appear to brighten toward lower frequencies while a dust component brightens toward higher frequencies.

For the 2014 season, two of the five *Keck* receivers were changed to observe at 95 GHz. In 2015, two more of the 150 GHz receivers were switched to 220 GHz, and in 2016, the 95 GHz receivers were switched to observe at 210 GHz. More recently, the last remaining 150 GHz focal plane was replaced with a 270 GHz focal plane, which occurred for the 2017 observing season. Additionally, we commissioned BICEP3, a 95 GHz telescope, in 2015 and began science observations with a fully-populated focal plane in the 2016 season [59, 60, 52, 61]. We have now accumulated 22 receiver-years of 95 GHz data, 18 receiver-years of 150 GHz data, 4 receiver-years of 210 GHz data, 6 receiver-years of 220 GHz data, and a single receiver-year of 270 GHz data. A receiver-year is defined as a single season of observations with the number of detectors at a given frequency that fits in a Keck receiver.

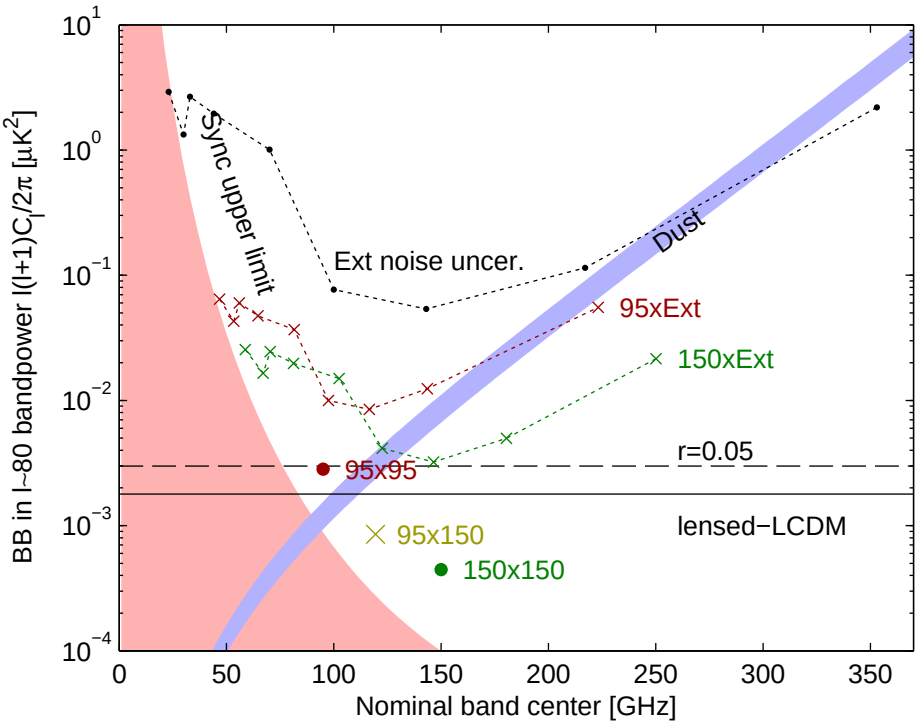

Figure 2.11: Measured limits on the B-mode signal of foregrounds in the BICEP/*Keck* observation field at multipole $\ell \sim 80$. This figure is plotted in CMB temperature units, which is the reason the lensed-ΛCDM and $r = 0.05$ lines are flat. The blue band is based on the best fit model using BICEP2 and *Keck* data through 2014, as well as external data from WMAP and *Planck*. The edge of the red region represents the upper limit on B-modes from synchrotron radiation in our field. In these units, dust increases in power toward higher frequency and synchrotron toward lower frequency. The level of B-mode contamination when using a single frequency is the sum of the dust and synchrotron signals at that frequency. Fitting the dust and synchrotron to the data will be discussed in Section 6.3. This figure is taken from BICEP2/*Keck Array* VI [62].

Chapter 3

DATA ANALYSIS

In Chapter 2, we discussed the procedures for collecting CMB data. In the current chapter we'll discuss the analysis steps used to reduce the data into power spectra.

3.1 Low Level Reduction

The CMB data coming from the telescopes are digitally filtered by the MCE[1] and again through GCP.[2] Other than that, they are raw and may contain defects which we want to exclude from our analysis. In this section, we discuss the low-level data reduction, which is a series of analysis steps beginning with raw data and resulting in the data product we call pairmaps. As stated in Section 2.2.6, we break our data into $\sim$50-minute blocks called scansets. Low level reduction is preformed on each scanset, and this reduction is independent of the other scansets.

[1] Multi Channel Electronics provide the interface between the detector operation inside and the data recording outside the cryostat.

[2] The Generic Control Program controls the operation of all aspects of the experiment.

3.1.1 Time-Ordered Data

The first step of reduction is to extract the data from the archive files for the relevant time period. This is time-ordered data (TOD), meaning the recorded data are packaged in sequential order. Along with the detector readout data, we archive the instantaneous telescope pointing (in telecentric coordinates), the GPS time, and a plethora of heater voltages and temperature readouts, which are used to monitor the health of each cryostat.

The filtering from the MCE and GCP shifts the bolometer data in the time domain. Once the appropriate chunk of data is loaded, we deconvolve the filtering kernel to remove the time domain shift. Also, it's possible for the SQUIDs to jump between stable set points, causing a discrete step in the data. When subjected to the filtering kernel, the discontinuity in the data results in an unphysical ringing in the signal. Therefore another early step in the data reduction searches for these steps in the data and discards the bolometer data surrounding the step in a range that is corrupted by the MCE and GCP filtering.

Figures 3.1 and 3.2 show the TODs for two scansets in July 2015. To create this figure, we've calculated the pairsum and pair difference (pairdiff) signals by adding and subtracting the signals from the two detectors within a pair and dividing by two. These two scanset are taken during different weather conditions. Figure 3.1 is taken during good weather, and Figure 3.2 is taken during bad weather. Although the atmosphere is structured in both cases, as evidenced by the amplitude variations in the pairsum signal within each halfscan, we can deduce that the atmosphere is largely unpolarized since the signal cancels in the pair difference signal.

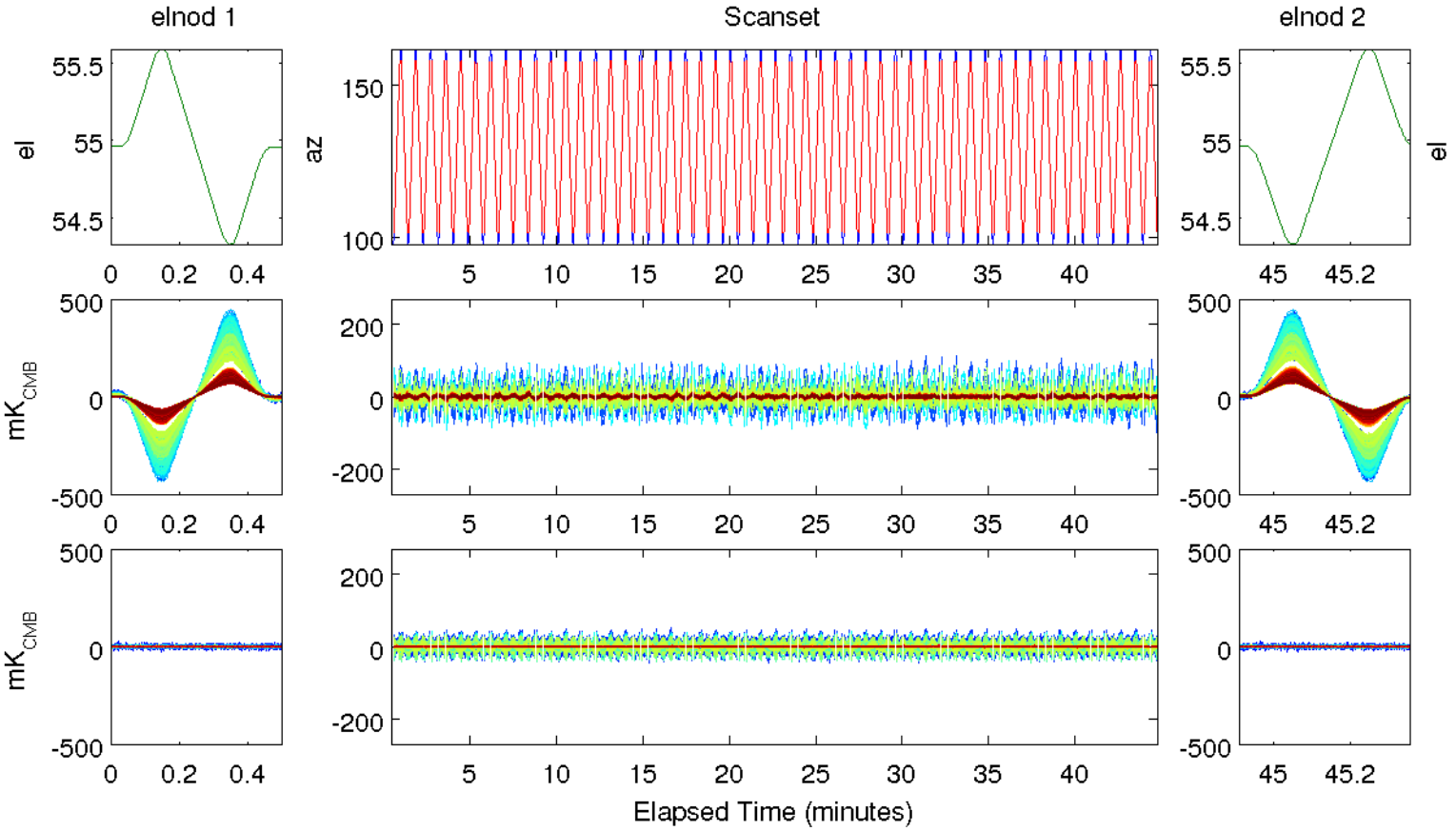

Figure 3.1: *Keck* scanset data from July 2015 during a period of good weather. The top row of panels show, from left to right, the mount motion starting with the leading elnod (AZ is stationary), the scanset (EL is stationary), and the trailing elnod. The middle row of plots show the pairsum data, and the bottom row shows the pairdiff. Each halfscan is mean-subtracted for display purposes.

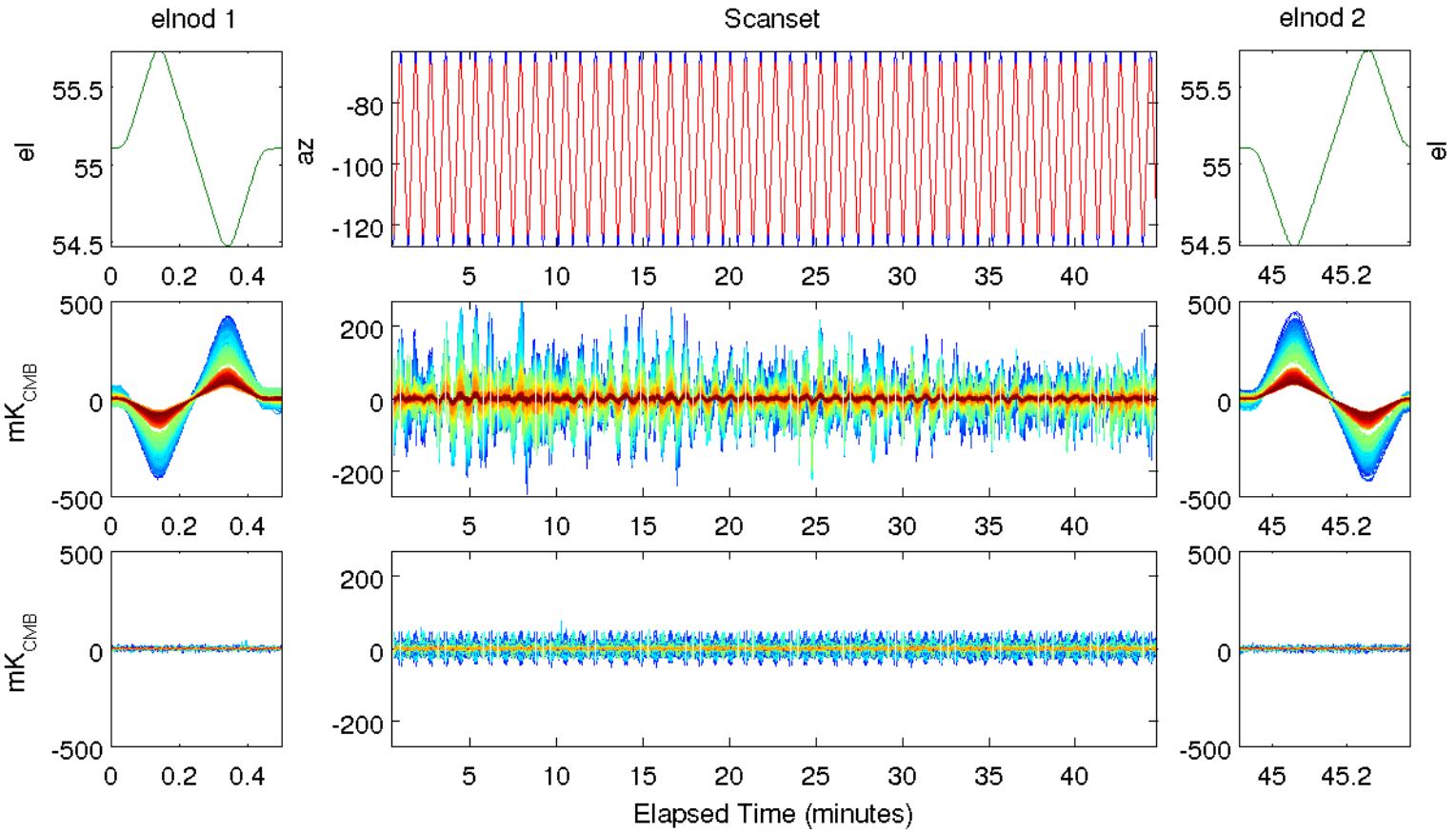

Figure 3.2: *Keck* scanset data from July 2015. This data is taken during worse weather than Figure 3.1, which is the reason the pairsum amplitude is larger; The telescope is scanning over larger variations in the amount of precipitable water vapor. Although the atmospheric emission is highly structured, it is not polarized, as evidenced by the cancellation of signal in the pair difference.

3.1.2 Relative Calibration

We use feedback units, also called analog-to-digital units (ADU), to describe the strength of the signal recorded by our detectors. These units are a measure of the feedback current which results from the changing resistance of the TES while holding the circuit voltage constant. In our use, ADU refers to a modulation in signal strength, not the DC level of the signal. Also, for a given underlying anisotropic CMB pattern, different detectors will not inherently record the same amplitude signal, even if it were possible to make noiseless measurements. In order to prevent a leakage of the temperature signal into polarization, and to weight the detectors for map coaddition, we must correct for the different levels of detector sensitivity. This is accomplished through an analysis step we call "relgain" (relative gain) calibration. Before and after each scanset, we nod the telescope in elevation, called an "elnod." This is a slow scan of the telescope by $\pm 0.6°$ in elevation, which produces a signal proportional to the gradient of the atmospheric opacity. We regress this signal against a secant model of the airmass through which the detectors scan, which gives us the detectors' gains in units of ADU/airmass. We then divide the detectors' data by their gains, which puts the signals in units of airmass. If we knew the sky temperature, we could then convert the timestreams directly into absolute temperature units, which is an avenue under current investigation. Instead, we multiply the signals by a normalization value that converts the signals back to ADU. A separate normalization value is calculated for each observing frequency. Before the 2014 data analysis, the normalization value was simply the median of all good detectors' gains.

There are three factors which influence a detector's measured gain: the innate sensitivity, the fractional resistance, and the weather. The innate sensitivity does not change for a given detector, but it does vary across the detectors. Optical loading and the voltage bias affect the

fractional resistance. An increase in the fractional resistance decreases the response of the detector. Finally, bad weather increases the opacity (and consequently the gradient of the opacity) of the atmosphere, which increases the measured elnod value.

In the BICEP2 data and first two seasons of *Keck* data, it was a reasonable assumption that the median of detector gains was stable. However, during the first half of the 2014 *Keck* season, we found issues with this assumption when a temporally split difference map showed a residual CMB temperature signal. The issues were two-fold. First, the TES biases were adjusted on several columns to reduce the detector noise, especially on the two new 95 GHz focal planes, which changed those detectors' fractional resistance. Second, there were periods of time when one or more of the receivers did not take data for a schedule due to cryogenic problems. Because the typical detector gain varied between receivers and since two receivers were at 95 GHz and three were at 150 GHz, the loss of one receiver was enough to change the distribution of gains, altering the median.

To avoid these pitfalls in our analysis of 2014 and later data, we calculated the detector gains in arbitrary units of power to calculate the normalization value. We convert the detector gains to power units with

$$\tilde{g} = gBC\frac{1 - R_{\rm sh}/R_{\rm s}}{1 + R_{\rm sh}/R_{\rm s}}, \tag{3.1}$$

where g is the gain in ADU/airmass (effectively current/airmass), B is the TES bias (effectively voltage), $R_{\rm sh}$ is the shunt resistance in the circuit and is ~ 3 mΩ, $R_{\rm s}$ is the detector resistance measured during the partial load curve, and C is a rescaling constant to make the medians of $\tilde{g}$ and g similar in numerical value. The rescaling constant is a matter of convenience so that data selection cuts (presented in Section 3.1.3) don't need to be altered, especially those which depend on the amplitude of the amplitude of the detector signal.

The value C is constant for an entire observing season, but it is allowed to change between years. The fractional term in the equation is the derivative of the power deposited in the TES with respect to the current; it takes care of the situation $R_s \not\gg R_{sh}$. To complete relative calibration for a scanset, we still divide each detector's signal by g, not $\tilde{g}$. We then multiply by the median of $\tilde{g}$ on a per-frequency basis. Since only the normalization value is calculated in units of power and modified with C to be similar magnitude to the pre-2014 calculation method, we still consider the timestreams to be in ADU after relative calibration. The normalization values for each scanset are shown for both calculation methods in Figure 3.3.

3.1.3 Data Selection

A final step before combining individual detector's data into maps is to remove compromised data. This is done through a series of data quality cuts. The purpose of these cuts is not to get rid of noisy data but to remove data which has glitches or does not match our assumptions and would therefore insert known systematics into our final data products. However, there is one cut which is a noise cut, scanset_std, which looks at the standard deviation of the entire scanning data, including the short amount of time between consecutive halfscans. This cut is a remnant from an old noise model that required stepless data, even while the mount was slowing and reversing direction. The scanset_std cut 0.9% of data uniquely for BICEP2 and uniquely cuts 1–2% of data in *Keck*.

Although the cuts are calculated before map coaddition, they are applied to the data in two separate steps, colloquially called "round 1" and "round 2" cuts. Round 1 cuts are applied on a per-halfscan basis, so they must be applied before the data is combined pair-wise into maps. The round 2 cuts involve statistics which indicate the entire scanset may be problematic for a given detector, so a failure of one of these cuts removes the detector's data for the

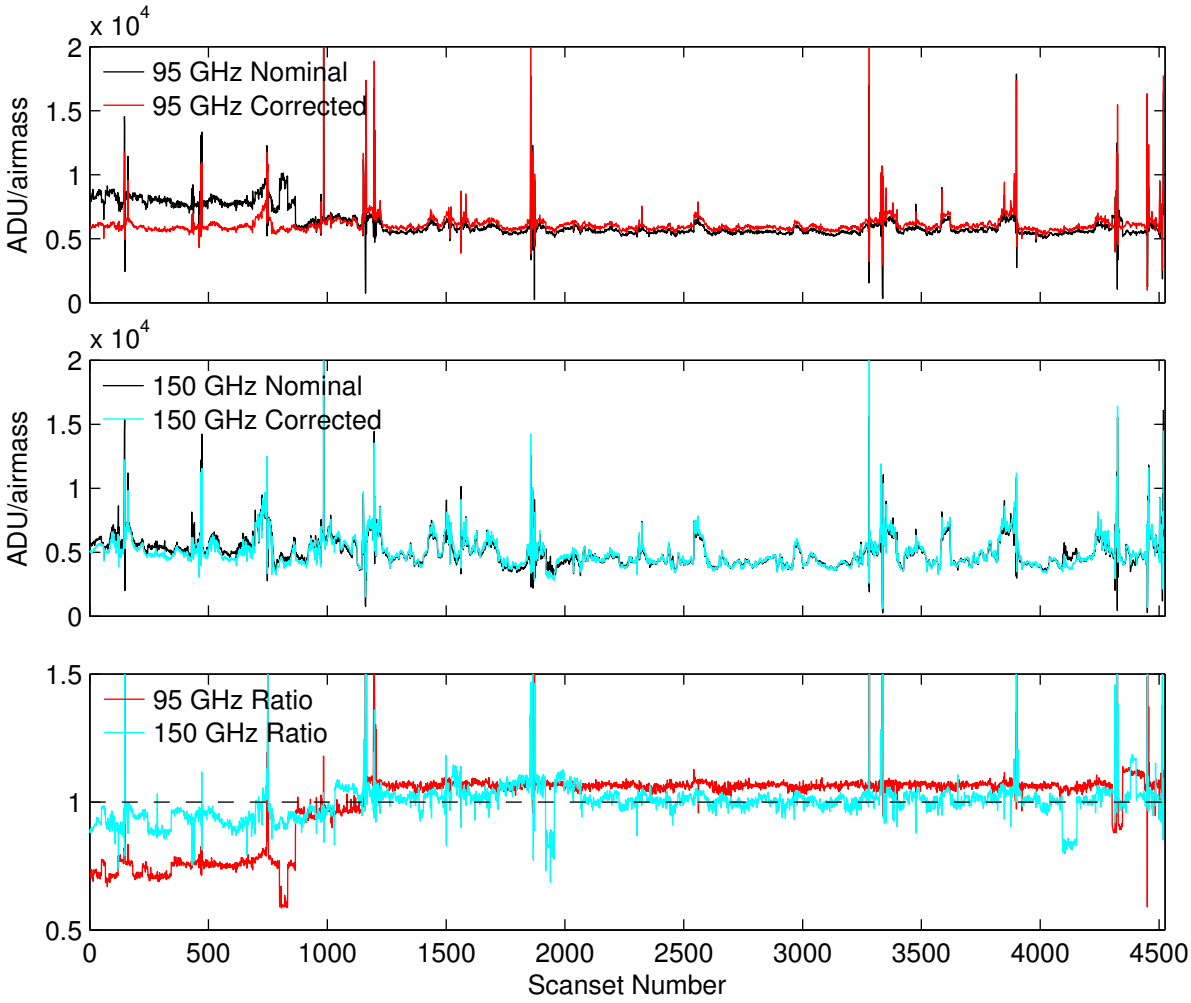

Figure 3.3: Comparison of the Elnod Median values (the value to which detectors responses are normalized) calculated in two ways. Most of the short timescale variations are due to changing weather conditions—i.e., changing atmospheric opacity. The method labeled "Nominal" is a simple median of elnods from all good pairs. The method labeled "Corrected" first converts the elnod values to arbitrary units of power before calculating the median. *Top*: Comparison for the 95 GHz receivers. The drop in the darker (black) line near scanset 900 is the result of changing the TES bias of many 95 GHz detectors. This drop is not present in the "Corrected" line. *Middle*: The same comparison for the 150 GHz receivers. *Bottom*: Ratios between the two methods of calculating the Elnod Medians for 95 and 150 GHz detectors. The places where the ratio drops below the general trend for tens of scansets, for example around scanset 800 for 95 GHz and before scanset 2000 for 150 GHz, is due to one or more receivers dropping out. The "Corrected" Elnod Median is more immune to these events.

entire scanset. In practice, these cuts are applied when creating the final maps, which will be discussed in Section 3.3. We should also note that both detectors in a pair must pass all cuts, or they will both be excluded from the final map. A summary of Round 1 and Round 2 cuts can be found in Tables 3.1 and 3.2, respectively.

A final data selection is the so-called channel cuts. These cuts remove detectors from consideration for the entire season based on detector characterization. We remove channels if they fail a consistency cut in the detector pointing analysis (see Section 3.2), if their absolute calibration values are outliers among others at the same frequency or very different between detectors of a pair, or if their measured beam shapes are outliers. The beam shapes are measured by scanning the telescope across a source located on a mast atop of a nearby building [48]. For the beam shape, we compare the beam width among all detectors at a common frequency (including the difference in beam width between detectors within a pair), the total ellipticity, and the differential ellipticity in a pair for both the plus and cross directions.

Table 3.1: Round 1 cuts for *Keck*. These cuts are applied before combining the time ordered data into pairmaps and can therefore remove individual half scans of data. Most of the Round 1 cuts are used for diagnostic purposes, not to remove data. Cut parameters which do not remove data have thresholds involving ∞.

Cut	Description	Threshold
fb_nancount	number of NaN values in scanning data	1
fb_std_p0	Std. Dev. of P0-filtered TODs	∞
fb_sd_p0_darks	Std. Dev. of P0-filtered dark channels	10
fb_std_p3	Std. Dev. of P3-filtered TODs	∞
fb_std_sd_p0	Std. Dev. of P0-filtered sum/diff TODs	∞
fb_std_sd_p3	Std. Dev. of P3-filtered sum/diff TODs	∞
fb_std_uncal	Std. Dev. before relative calibration	∞
is_fj_row	Is a flux jump present in any detectors of MUX row?	∞
is_fj_col	Is a flux jump present in any detectors of MUX column?	∞
syncsampnum_diff1	Flag if data sample is out of order (across time)	logical
syncsampnum_diff2	Flag if data sample are in different order among receivers	logical
passfrac_col	Fraction of detectors cut within a MUX column	0.7
passfrac_chan	Fraction of detectors cut within a receiver	0.7

Table 3.2: Round 2 cuts for *Keck*. These cuts are applied when coadding pairmaps into maps. Like the Round 1 cuts in Table 3.1, some of these cuts are for diagnostic purposes and are not used to discard data. Those cuts have thresholds of ∞.

Cut	Description	Threshold
elnod_mean	Average of leading and trailing elnod gains (in ADU/airmass)	1000 - 30000
elnod_fracdel	Fractional change in elnod gains over scanset	0.3
elnod_ab_ba	Ratio of ratio of gains in a pair before and after scanset	0.04
elnod_median	Elnod gain to which detectors are normalized (in ADU/airmass)	4500 - 10000 (95 GHz) 3000 - 9000 (150 GHz) 2000 - 8000 (220 GHz)
elnod_nancount	Number of NaN values during elnod	1
elnod_gof	Elnod goodness of fit	250
elnod_chisq_dif	χ^2 of pair difference of elnod	10
fb_wn_sd_p0	Average of sum/diff PSD in range 1.5 - 2.0 Hz	∞
fb_1f_sd_p0	Average of sum/diff PSD in range 0.1 - 0.3 Hz	∞
skewness_dif	Skewness of pair difference data	0.2
skewness_sum	Skewness of pair sum data	∞
satcom	Maximum χ^2 of AZ-fixed signal between consecutive halfscans	6
fp_corr	Average of off-diagonal detector-detector correlation matrix	∞
scanset_std	Std. Dev. over entire scanset (in ADU)	2.5
stationarity_ab	Std. Dev. of Std. Dev. of P3-filtered TODs	0.0 - 0.7
stationarity_dif	Std. Dev. of Std. Dev. of P3-filter pair difference	0.0 - 0.2
tfpu_mean	Average focal plane temperature (in K) during scanset	0.20 - 0.30
tfpu_std	Std. Dev. of focal plane temperature (in K) during scanset	5×10^{-5}
enc_az_diff	Difference in Δcounts between the 4 AZ encoders	30000 ($\sim 0.03°$)
az_range	Range of AZ angles (in degrees) recorded during scanset	100
num_fj	Number of flux jumps	5
num_destep	Number of discrete jumps removed in the TOD	5
max_fj_gap	Maximum flux jump step (in ADU)	1000
rtes_frac	TES fractional resistance	0.10 - 0.95
passfrac_halfscan	Fraction of half scans surviving Round 1	0.9
passfrac_scanset	Fraction of detectors in receiver surviving Round 2	0.3

3.1.4 Pairmaps

Once we have TODs with relative gain calibration applied, we can move on to binning the timestream data into maps. The first step of the process is to combine the data pair-wise into maps, which we call "pairmaps."

At this point, we are free to chose between filtering options. Typically, and for all released results, we first fit and remove a third order polynomial to the data in each halfscan, which excludes the portion of data where the telescope scan slows and reverses direction. The polynomial filter is regressed against telescope azimuth position, not time sample, and it removes a significant portion of the atmospheric 1/f signal. Colloquially, the next filter applied is called "ground subtraction" where we remove the average signal over all halfscans from each halfscan. This procedure most strongly filters any signal which is present at the same AZ coordinates during the scanset. Examples of ground-fixed signal which might be present in the data include radio and satellite communication at the South Pole and the Earth's magnetic field. Both polynomial filtering and ground subtraction filter real CMB signal in the direction of the telescope scan.

After filtering, we apply the round 1 cuts to the data. Then we calculate the pairsum and pairdiff data and calculate the weight to use with each pair. Again, there are several options, but we typically weight by the inverse variance of the TODs over all half scans. We then bin the data into map pixels by combining the telescope pointing with the detector pointings[3] to calculate which portion of the sky each detector is scanning at each time step. In practice, we calculate the average of the detector locations within each pair since we've already combined the detector data into pairsum and pairdiff timestreams. We also typically use 0.25° pixels when creating our maps.

[3]Until we've accumulated sufficient data to fit the detector pointings (see Section 3.2), we use nominal detector pointings and polarization angles.

The data product we now have is called a pairmap, and it contains the necessary values, in arrays of map pixels, to construct T, Q, and U maps. Although we can make a temperature map for a single scanset for each pair, we cannot do the same for the polarization maps because we can't simultaneously measure Q and U at a single telescope boresight orientation. Instead, we keep the necessary information to calculate Q and U when coadding the final map. A full list and description of the accumulated quantities can be found in appendix A of Grant Teply's thesis [63].

A parallel step in pairmap production is to calculate deprojection templates. Deprojection is a method for removing polarization contamination caused by unmatched beam shapes and locations on the sky for detectors within a pair. For a given observation band, we resample the nearest *Planck* frequency band temperature map (and its derivatives) that has been resmoothed with our average measured detector beam function. We form templates necessary to deproject the following possible mismatches between elliptical Gaussian beams of the detectors within a pair: (i) "relgain," which allows for the possibility that relative gain calculated off the atmosphere could be sub-optimal for the CMB, (ii) "diffpoint," which allows for the detector beam centers to be non-coincident on the sky, (iii) "differential beam width," which allows for the sizes of the beams to differ, and (iv) "differential ellipticity," which allows one of the beam's major axis to be rotated with respect to the other's.

3.2 Detector Pointings

To convert a detector's timestream data into a map of the sky, we need an accurate knowledge of the portion of sky the detector is sensitive to at any given time during a scan. The locations can be broken into two parts. The first comes from a pointing model for the telescope, which converts telescope pointing information to sky coordinates. To derive the pointing model,

we use an optical star camera rigidly attached to the telescope to periodically measure the mount position with respect to a set of stars, taking the measurements at multiple dk and AZ angles.[4] By recording the AZ and EL offsets necessary to center the stars, we fit a 10-parameter model that includes flexure, axis tilts, encoder offsets, and collimation error of the star camera [54]. So that we can interpolate between two pointing models, we take star pointing data at the beginning and end of each season (in addition to the star pointing data taken throughout the season). If no so-called "bracketed star pointings" exist, we use the pointing model from the most recent run.

The second part of the location breakdown requires a knowledge of the individual detector pointings with respect to the mount pointing. We begin with nominal pointings based on the designed physical locations of the detectors on the focal plane, plate scale of the telescope, and rotation angle of the cryostat within the mount. With these nominal pointings, we produce a special set of pairmaps for individual detectors, not pairs (see Section 3.3 for information on map production). We produce separate maps for left- and right-going scans for each dk angle and correlate the maps against a *Planck* map. The *Planck* map used is the one nearest the detector's observation frequency, and it's resmoothed to our average measured beam function for that frequency. For *Keck* data from 2013 until present, we have 16 measurements of the beam pointing for each detector. We average the 16 measurements and take the standard deviation as the uncertainty of the position. Detectors which are not well measured are not used in the CMB analysis (see Section 3.1.3). Figure 3.4 shows the pointing offsets measured for the *Keck* receiver Rx4 from the 2014 CMB data.[5] If we did not apply these offsets, our measurement of the CMB would be blurred. Figure 3.5 shows

[4]The elevations of stars change very little through the day at our observing site, but the azimuth of a star will change by the time it is revisited.

[5]We label the five *Keck* receivers Rx0–Rx4.

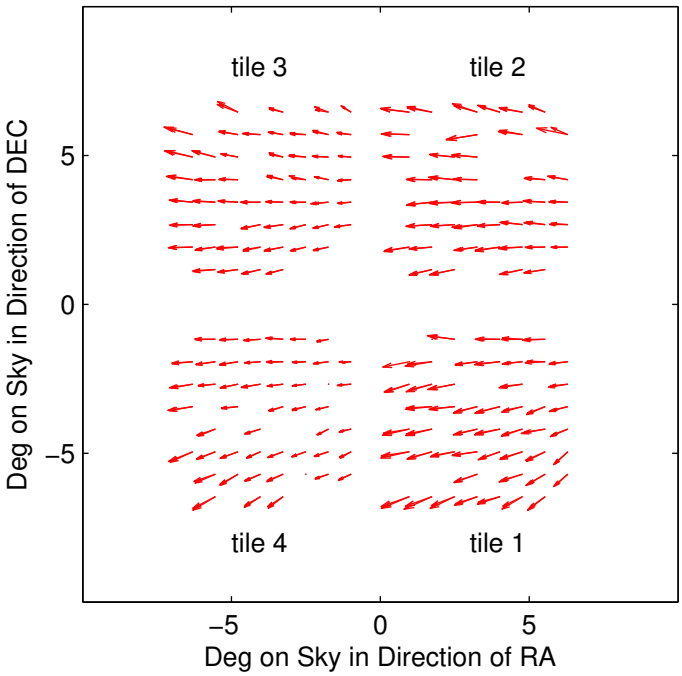

Figure 3.4: Mean of 16 measured beam pointing shifts from nominal for Rx4 in *Keck* 2014 data. Arrow lengths are 5 times the actual shift. If the standard deviation of the 16 beam pointing measurements for a given detector is larger than 0.°1, that detector is excluded from this plot.

the standard deviations of the 16 detector pointing measurements for all detectors in the *Keck* 2014 season.

Once we've calculated the detector pointings, we fit a four-parameter model to the pointing shifts for each receiver individually. The model includes two orthogonal translations, a rotation, and a scale factor. The rotation parameter is then applied to the nominal polarization angles in that receiver. We do this because we interpret an overall rotation of the detector pointings as a rotation of the focal plane within the telescope mount, likely from a small rotation of the cryostat within the telescope drum. The rotation angles are typically $< 1°$. We use the updated detector pointings and polarization angles to recreate pairmaps that are used in the final analysis.

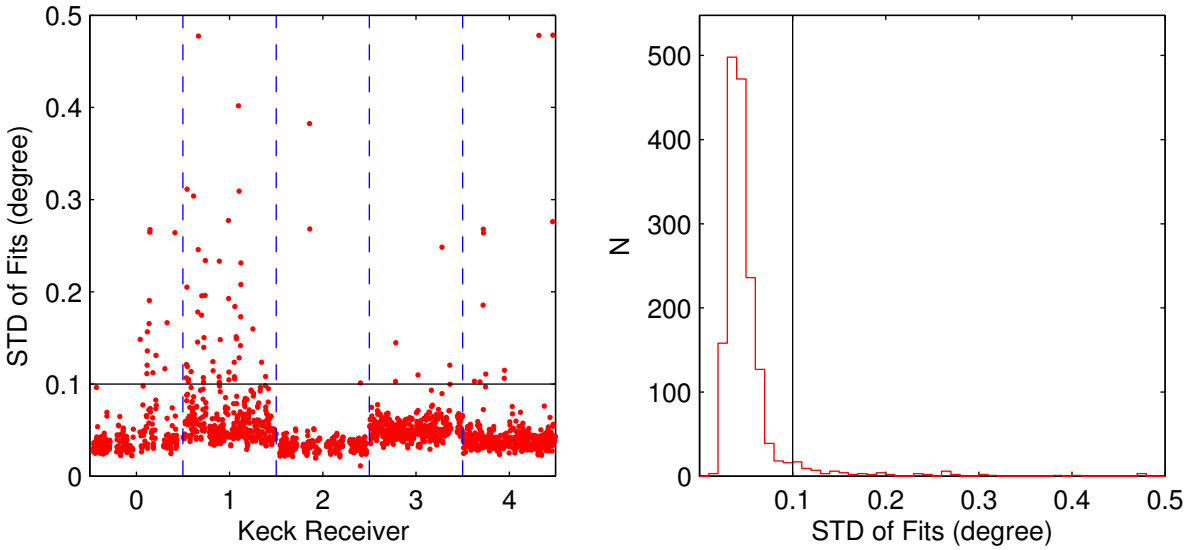

Figure 3.5: Standard deviations of beam pointing measurements using the full season of *Keck* data in 2014. The standard deviations are calculated from 16 measurements, eight deck angles and two scanning directions. *Left*: Values separated by receiver number. Only detectors below the horizontal solid black line are included in our analyses. *Right*: Histogram of all values, including a line to indicate the cut threshold of 0.°1 (this threshold was increased in subsequent years for the higher frequency detectors). Detectors with larger standard deviations are excluded from the CMB analysis.

3.3 Map Coaddition

The analysis in Section 3.1.4 produces a pairmap for each scanset that is written to disk. We can now combine the pairmaps over pairs and scansets to produce data products we call "coadded" maps. In our first combination, we typically combine detector pair data within a single receiver. With BICEP2 there was only one receiver, and we combined the data over all three years in single go. Since we changed the focal planes and frequencies in *Keck*, we produced separate coadded maps for each year of data. Other granularities for combining over sets of detectors are necessary for diagnostic and calibration purposes. Those granularities include single detector maps,[6] single pair,[7] and per tile.

One of the steps in map coaddition is to apply the round 2 cuts. These are applied at this stage so that we have the ability to change the cut thresholds without having to recompute the pairmaps. We also accumulate the deprojection templates and regress the chosen modes against the data on the time scale of a phase, which involves scaling the regression template to best fit the data. Deprojection is essentially a filtering operation and can remove real signal due to real TE and chance correlations. This creates a trade off in the choice of timescale over which to perform the regression. The longer we wait, the more pixels in the map will have been observed, which reduces the filtering of the CMB. However, if we wait too long, the detector qualities which produce the systematic leakage, such as relgain, may change. Rather than regress a template, we also have the option to remove a measured value from the data, which avoids filtering CMB signal in as much as the measured quantity is stable and matches reality. In our standard analysis, we use the measured differential ellipticity instead of the deprojection template. Whether we use templates or measured values, we

[6] These require special pairmaps where the pairsum and pairdiff are not calculated.

[7] These differ from pairmaps because they are combined over scansets.

combine the data over the deprojection timescale, subtract the desired modes, and add to the previously accumulated data, and move on to the next chunk of data.

In addition to combining all of the data into a single map, we also create "jackknife" maps. As the coaddition is occurring, the data are split between two maps. The jackknife maps are used to investigate possible systematic effects. They are constructed so that the systematic effect would affect only one of the two maps. Some of the jackknife maps are temporal, meaning all data from a scanset goes into one half or the other; some are pair selections, meaning a given pair goes into the same half over all scansets; and some are a mixture.

3.4 Absolute Calibration

In addition to relative gain calibration, we perform an absolute calibration, finding the value in units of $\mu\mathrm{K}_{\mathrm{CMB}}$/ADU necessary to convert our maps into CMB temperature units. We calculate the value by cross-correlating our TT maps with an external map we call the reference (ref) map. We also cross-correlate the reference map with another external map, called the calibration (cal) map in order to avoid noise bias from the external map. For the *Keck Array* we currently use *Planck* maps at two different frequencies for both the ref and cal maps, but we've also used WMAP maps for the early season of *Keck*. In Table 3.3, we show which *Planck* maps were used for reference and calibration to calculate the absolute calibration values for the different *Keck Array* frequencies. The gain as a function of multipole bin is calculated as

$$g_\ell = \frac{\langle m^{\mathrm{ref}} \times m^{Keck} \rangle_\ell}{\langle m^{\mathrm{ref}} \times m^{\mathrm{cal}} \rangle_\ell}. \tag{3.2}$$

Table 3.3: The *Planck* reference and calibration maps used for each of the *Keck Array* frequencies.

Keck Map	Ref Map	Cal Map
95 GHz	*Planck* 143 GHz [64]	*Planck* 100 GHz [65]
150 GHz	*Planck* 100 GHz	*Planck* 143 GHz
210/220 GHz	*Planck* 143 GHz	*Planck* 217 GHz [66]

In practice, $\langle m^a \times m^b \rangle_\ell$ is the cross correlation between map a and map b calculated in Fourier space after squaring and collapsing the 2-D Fourier transform in annular multipole bins ℓ. The subscript ℓ on the expectation value indicates that we calculate a gain for each multipole bin. The inverse of the gain is the absolute calibration, and we use the mean of the bins in the multipole range $50 < \ell < 200$ as our absolute calibration value.

3.5 Simulations

We perform an ensemble of signal and noise simulations called a simset. For the signal simulations we begin with T, Q, and U maps that are smoothed with our average measured beam function. Although we use the *Planck*-measured T map in every realization, we allow the Q and U maps to vary, which enables us to estimate uncertainties from cosmic and sample variance. We "observe" these maps by using the pointing information of the telescope and detectors at each time step to calculate the expected detector signal (without noise) if the input map represented the true sky. This process creates a timestream that is then processed in an identical way to the real data. Since the simulated timestream is an idealized detector signal, we use the weights and cut information from the real data to preserve the sky coverage.

The noise simulations are really pseudosimulations in that they're special coadditions of

the real data. We refer to these simulations as "sign-flip" noise sims, and the procedure is adapted from SPT [67]. We reverse the sign of the signal for roughly half of the pairmaps and coadd the results. Which pairmaps are sign-flipped is randomly assigned for each realization, but we ensure that the total weight is equal between the pairmaps which are sign-flipped and those which are not. The results of these pseudosimulations is that the real signal cancels, but the noise does not. We then add these noise sims to the signal sims to produce signal plus noise simulations.

The computing requirements for creating a simset are large. In our standard analysis, we create 499 realizations of each of four simulation types. The simulation types include unlensed-ΛCDM, lensed-ΛCDM, dust only, and B-modes only. These simulation types are discussed in more detail in the BICEP2 results paper [47]. We perform our simulations on the Odyssey cluster at Harvard. Given the average throughput our collaboration is allotted, it takes a couple of months of calendar time to complete a simset for a season of *Keck* data. This would take about twice as long without changes we implemented in our simulation procedure starting with the BICEP2 analysis. Since our scanning pattern is highly repetitive, it is not necessary to create a simulated pairmap for each scanset. Table 3.4 lists the number of unique scanning trajectories for each year of *Keck* data. This should be compared to the number of total scansets in a year, which averages 4,500 for *Keck*. For each of the unique scans, we simulate a pairmap that serves as a representative for all scansets with the same scanning trajectory. We do not apply cuts to the pairs at this step because the cuts for the representative scanset are not appropriate for every scanset. During the coaddition phase, we then load the appropriate representative simulated pairmap and apply the weights and cuts from the real pairmap. We have checked that the resulting variance maps agree with the real maps to very good precision. The amount of disk space required for a scanset scales

Table 3.4: Number of unique scanning trajectories for each year of *Keck* data. The number of unique scans is the product of the number of telescope deck (DK) and elevation (EL) angles and right ascension (RA) centers. The EL steps are separated by $0.^{\circ}25$ except in 2015, where they're $0.^{\circ}125$. Starting in 2015, we observed at the same elevation and between the same azimuth limits for two scansets in a row, which is the reason there are two RA centers for that and subsequent years.

Year	DK	EL	RA	Unique
2012	4	20	1	80
2013	8	20	1	160
2014	8	20	1	160
2015	8	40	2	640
2016	8	20	2	320
2017	8	20	2	320

almost linearly with the number of simulated pairmaps, and $\sim$100 TB of disk space were required for the 2015 *Keck* simset. If we made simulations for every pairmap, the 2015 *Keck* simset would have needed closer to 700 TB of disk space.

3.6 Power Spectra

With the absolute calibration applied, we can now perform the rest of our analysis in CMB temperature units. After we perform the calculations to convert our coadded data into T, Q, and U maps, we calculate the angular power spectrum (APS) of the maps, both real and simulated. A simple choice for an estimator is to apodize the maps with a smoothed version of the inverse noise variance map, calculate the 2-D Fourier transform, construct E and B from Q and U, square, and take the mean power within annuli in the Fourier plane. However, simulations showed there was an unacceptable level of E/B mixing [47]. We could remove the leakage in the mean from our data, but this leaves the sample variance of the leakage unchanged. This sample variance contributes to the uncertainty of our band powers and can

make a small-signal detection impossible even in the absence of noise.

We reiterate the construction of E and B from Q and U, which first appeared in Equations (1.17) and (1.18):

$$E(\ell_x, \ell_y) = +Q(\ell_x, \ell_y)\cos(2\phi) + U(\ell_x, \ell_y)\sin(2\phi) \tag{3.3}$$
$$B(\ell_x, \ell_y) = -Q(\ell_x, \ell_y)\sin(2\phi) + U(\ell_x, \ell_y)\cos(2\phi), \tag{3.4}$$

where $\phi_\ell = \arctan(\ell_x/\ell_y)$. This transformation is non-local, so anything which filters real modes on the sky will lead to mixing between E and B. In our case modes are filtered due to timestream filtering and our partial sky coverage. Smith suggested an algorithm which can correct for incomplete sky coverage [68], but we found this method did not provide sufficient improvement over the "simple" choice since it does not correct for mixing due to timestream filtering [47]. We have therefore turned to a matrix-based map purification.

3.6.1 Matrix Purification

Matrix-based map purification is a filtering operation. We are able to determine which of our measured B-modes are sourced from true B-modes and which are sourced from true E-modes on the sky. There are also modes which are ambiguous. We then filter out the B-modes sourced from E-modes and ambiguous modes, leaving a "purified" map. The complete method is described in the BICEP2 matrix paper [69].

3.7 TB/EB Fitting

In the standard cosmological model, we don't expect to find TB or EB cross correlation in the CMB, but we typically find non-zero TB and EB signals in our data. Using Equa-

tions (1.23) and (1.26), we can fit for the overall angle $\Delta\alpha$ necessary to produce the TB and EB correlations present in our data. This could then be interpreted as a detection of cosmic birefringence (see Section 1.5.1), an indication of a systematic error in our polarization angles, or some combination of the two. We examine the first two of these possibilities. Table 3.5 shows $\Delta\alpha$ with statistical uncertainties present in the combined BICEP2/*Keck* data through the 2015 season, labeled BK15. We also show the rotation angle for the 150 GHz *Keck* 2015 data (labeled $\mathrm{K2015}_{150}$), which is one receiver for one season, for comparison, and because it will be useful in Chapter 4. In principle the rotation angle measured for $\mathrm{BK15}_{150}$ is a nearly 5σ detection of a non-zero value. However, the systematic uncertainty on our polarization angles is at least as large as the measured value. Consequently, we rotate our Q and U maps by $2\Delta\alpha$ before calculating the angular power spectra in order to minimize the TB and EB cross correlations.

By applying the rotation angles to minimize our TB and EB spectra, a step we call "self-calibration," we assume that the level of cosmic birefringence is negligible. We give up the ability to constrain the true level of isotropic cosmic birefringence, thereby decreasing the science reach of our data. The main work of this dissertation is an attempt to measure the polarization angles of our detectors as projected on the sky. With an accurate knowledge of our detectors' polarization angles, we can remove this limitation imposed by self-calibration.

Table 3.5: Global polarization rotation angles in the BICEP2/*Keck* (BK) data through 2015. We also include the rotation angle for the 150 GHz data from 2015 alone because it will be useful in discussions in Chapter 4. The rotation angle, $\Delta\alpha$, is the angle by which we can rotate our Q and U maps to minimize the TB and EB spectra.

Data	$\Delta\alpha$ (deg)
$\mathrm{BK15}_{95}$	-0.19 ± 0.24
$\mathrm{BK15}_{150}$	-0.56 ± 0.12
$\mathrm{BK15}_{220}$	1.60 ± 0.82
$\mathrm{K2015}_{150}$	-0.03 ± 0.33

Chapter 4

CALIBRATOR

4.1 Polarization Calibration

An often tricky component of CMB polarization measurements is determining the polarization angles of the detectors as projected on the sky. Without an accurate knowledge of the polarization angles, leakage between EE and BB occurs, creating false EB and TB correlation. This false correlation diminishes the ability to search for parity-violating physics like a uniform polarization rotation from cosmic birefringence (see Section 1.5.1). Additionally, if the polarization angles within a pair of detectors are not orthogonal, there will be a loss in polarization efficiency. Below, we present a non-exhaustive list of calibration techniques used for measuring the polarization angles of CMB detectors.

4.1.1 Polarizing Grids

A polarizing grid is made of a series of parallel wires and can be used to produce a polarized calibration source. The portion of the radiation polarized along the wires is absorbed, and

the portion which is orthogonal is transmitted through the grid. One way in which such a grid can be used is in the apparatus shown in Figure 4.1. The pictured calibrator was used with BICEP1, mainly to measure the orthogonality and the cross-polar response of the detectors [70]. The aperture of the device is nearly bisected by the shadow in the image, and there is a blade lined with microwave-absorbing material which rotates in front of this aperture, alternating between radiation from the cold sky and this ambient temperature load. Below the aperture is the polarizing grid, and it's mounted on a rotation stage. An accurate knowledge of the polarizing grid orientation with respect to absolute coordinates is necessary to determine the individual detector polarization angles. However, this calibration device is highly non-ideal because the polarized radiation illuminates only a small fraction of the telescope aperture.

Another example of a polarizing grid in the near field was used with ACTPol [71]. In this case, an aluminum-coated plastic film was laser ablated to create an effective parallel wire pattern. The film was stretched and attached to an aluminum ring, mounted in place of their half-wave plate, and rotated at up to 2 Hz. This calibrator did not have an absolute reference point, so they used a single detector as a reference for the other detectors in the same cryostat. When comparing the calibrator-derived polarization angles of all detectors to their expected angles, the standard deviation of differences was 2° for this calibrator. Suggested sources for the scatter included vibration of the plastic film in the wind, wrinkles in the film arising from the mounting procedure, and a lack of uniformly straight wires across the grid due to small misalignments in the ablation process.

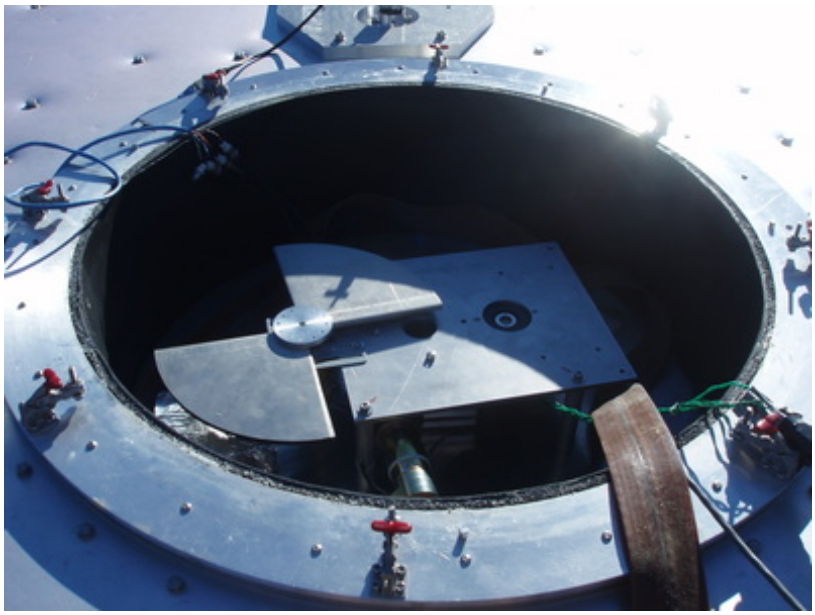

Figure 4.1: A calibration device used to measure the cross-polar response and orthogonality of the BICEP1 detectors. A wire grid (not visible) on a rotation stage is located below an entrance aperture. Above the aperture, a rotating blade covered in a microwave-absorbing material alternates the source radiation between ambient and the cold sky. This figure is taken from the BICEP1 instrument paper [70]

4.1.2 Rotating Polarized Source

Another polarization calibrator used in our collaboration is called the Rotating Polarized Source (RPS). This apparatus, and an example of recorded BICEP2 data, is shown in Figure 4.2. The RPS also uses a wire grid to create polarized radiation, but the calibrator is different from that presented in Section 4.1.1. Figure 4.2 shows the RPS in the lab. The rectangular box is attached to the rotating stage, and it contains a broad-spectrum noise source near the exit aperture. The wire grid is at the end of the metal cylinder opposite the box. When in use, the RPS is mounted on top of a mast $\sim$200 meters away from the telescope. Due to this geometry, the calibrator is located at a very large zenith angle as viewed by the telescope under calibration. Therefore, we place a large 45° flat mirror in front of the telescope so that the source is visible above the ground shield. The telescope then makes a raster scan of the source before the RPS is rotated to a new orientation angle.

In order to extract polarization angles from the RPS data, the wire grid orientation must be registered with respect to absolute coordinates. This is accomplished by measuring the level with respect to gravity with a digital level meter and by registering the wire grid orientation as it is mounted with respect to the encoder reading of the rotation stage. The second of these is accomplished with a portable microscope attached to a milling machine while using the machine's motion axis to move the grid under the microscope. A lack of accuracy in the wire grid orientation results in a systematic rotation of the measured polarization axes.

4.1.3 Dielectric Sheet

A dielectric sheet can be used to produce a partially polarized signal that can be modeled using the Fresnel coefficients. When a dielectric sheet is used in a polarization calibrator, it's important to keep track of both the reflected and transmitted radiation off and through

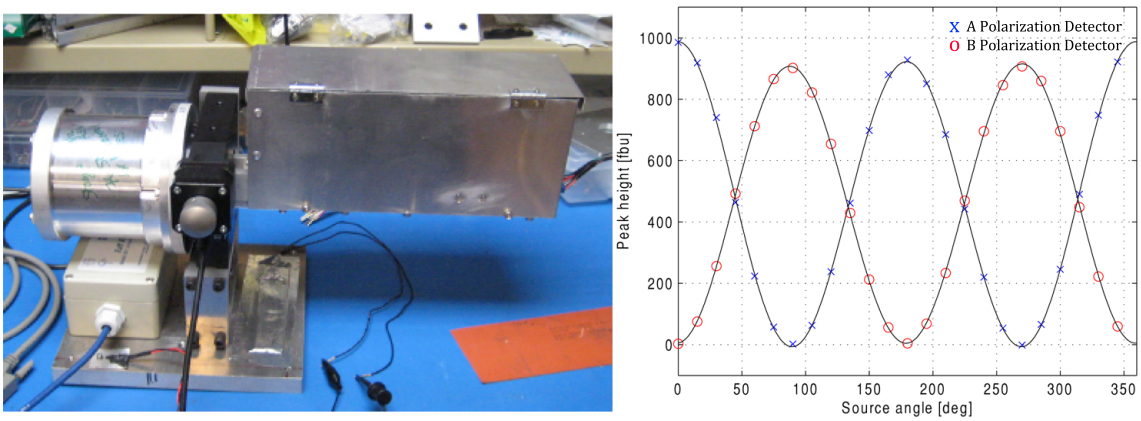

Figure 4.2: *Left*: The rotating polarized source. The metal box is attached to a rotation stage whose level with respect to gravity is measured with a digital level meter. Inside the box is a thermal broad-spectrum source, located near the exit aperture. The wire grid is on the end of the metal cylinder opposite the box. *Right*: An example of BICEP2 data taken with the RPS. The signal amplitude is recorded with respect to the source rotation angle for a pair of orthogonal polarization-sensitive detectors. This figure is taken from BICEP2/*Keck Array* IV [48].

the sheet. The fraction of incident radiation that is transmitted and reflected depends on the angle of incidence. However, not all polarization states are transmitted or reflected equally. That means a polarization sensitive detector under a dielectric sheet will "see" a modulated signal when the orientation of the plane of incidence changes with respect to the detector's polarization axis. We use a dielectric sheet in a calibrator we call the Dielectric Sheet Calibrator (DSC). The DSC is covered in detail in the rest of this chapter.

4.2 Dielectric Sheet Calibrator

The purpose of the Dielectric Sheet Calibrator is to measure the polarization angles of our detectors. We show the nominal polarization angles as projected on the sky for one *Keck* receiver in Figure 4.3. These are the angles which are currently used for this receiver when

analyzing the 2016 season of data. By calibrating with the DSC, we could potentially update the polarization angles shown in this figure. We can also use the DSC measurements to investigate any systematic error that results from using the nominal polarization angles, and this will be explored in Chapter 5.

The concept for the DSC was originally used with the POLAR experiment [72]. This type of calibrator uses a thin plastic film oriented at $\sim 45°$ to the telescope's optical axis and housed in an absorptive baffle to create a partially polarized beam-filling signal that modulates as the plastic film rotates about the optical axis. A version of the DSC was used with BICEP1 [73] and BICEP2 [74]. We redesigned the DSC for use with *Keck*, and we'll mainly focus on the *Keck* version in this dissertation.

A schematic for the DSC is shown in Figure 4.4, and two views of the DSC mounted on one of the *Keck* telescopes is shown in Figure 4.5. Nominally oriented at 45° to the cylindrical axis of the baffle is a 0.9 mil thick biaxially oriented polypropylene (BOPP) film, the dielectric sheet. The film, clamped in an elliptical ring, acts as a beam combiner. Most of the cold sky radiation is transmitted to the detectors, and a small amount of radiation from the warm baffle is reflected to the detectors. The baffle is lined with 10 mm thick microwave absorbing Eccosorb. The Eccosorb is covered with a closed-cell, thin polyethylene foam that provides an environmental shield. These materials are the same as those used in the *Keck* forebaffles. In fact, the DSC baffle replaces the *Keck* forebaffle during calibration. When in operation, the baffle and dielectric sheet rotate in front of a receiver, the telescope under test. This changes the plane of incidence with respect to the detector, which modulates the signal. Additionally, all of our detectors are slightly off-axis, which means the angle of incidence also changes when the calibrator rotates. This causes the signal to deviate from a sinusoid.

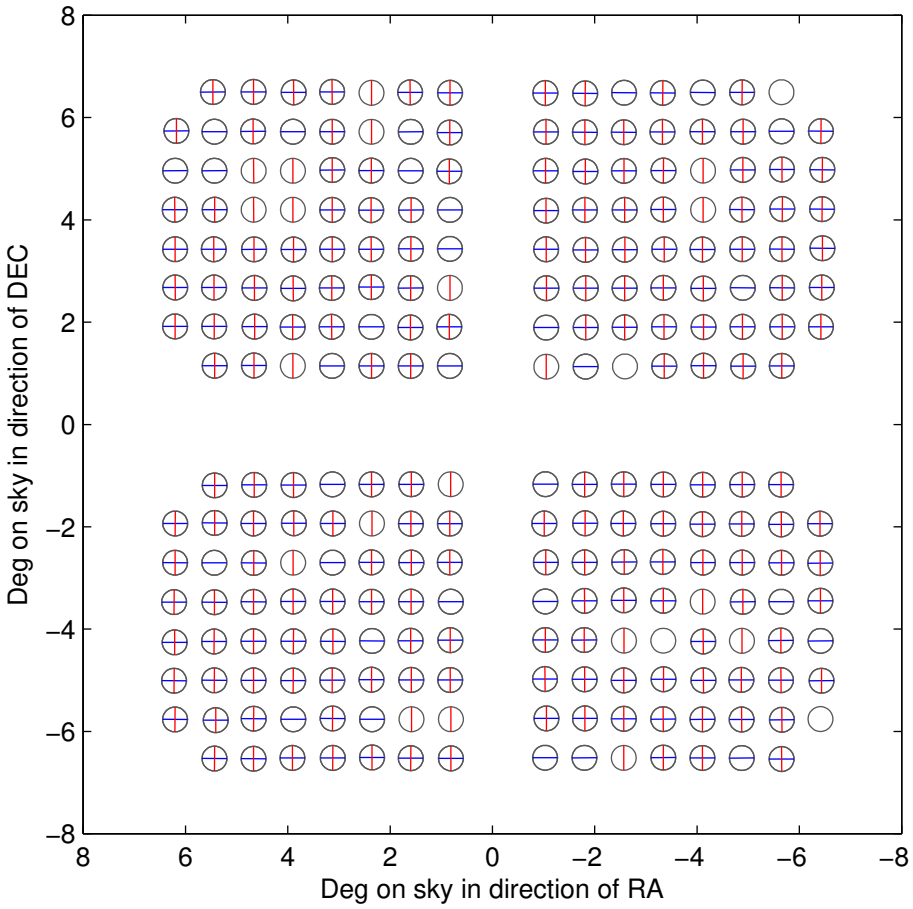

Figure 4.3: Polarization angles as projected on the sky, shown as red and blue orthogonal lines, for one *Keck* receiver. These are the nominal angles that were used to analyze the 2016 season of data for this receiver. We see that the polarization angles are nominally aligned with the rectangular grid of the detector locations. A primary goal of this dissertation is to measure the polarization angles of our detectors with the Dielectric Sheet Calibrator.

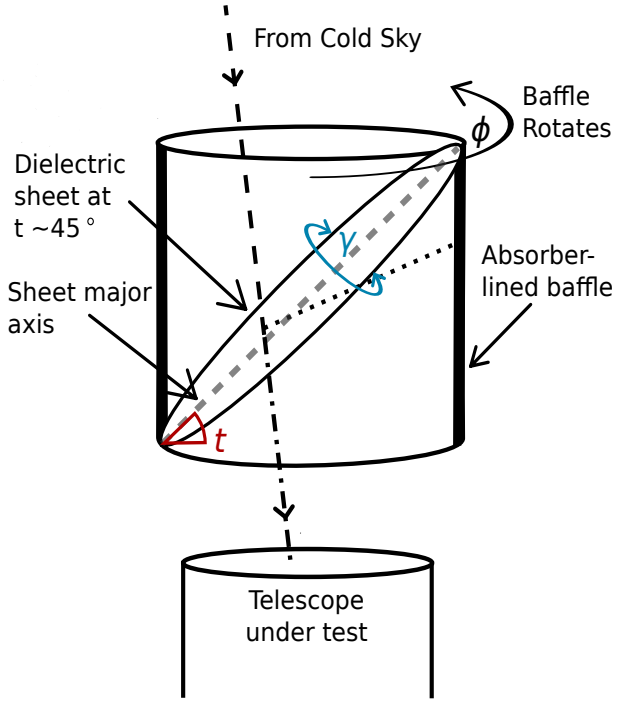

Figure 4.4: A schematic of the DSC. Most of the radiation from the cold sky is transmitted through the dielectric. A small amount of radiation from a "warm" absorber-lined baffle is reflected off the dielectric. The angles t, ϕ, and γ describe the orientation of the dielectric. During the measurement, only ϕ changes, which changes the plane of incidence for the transmitted and reflected radiation as well as the angle of incidence.

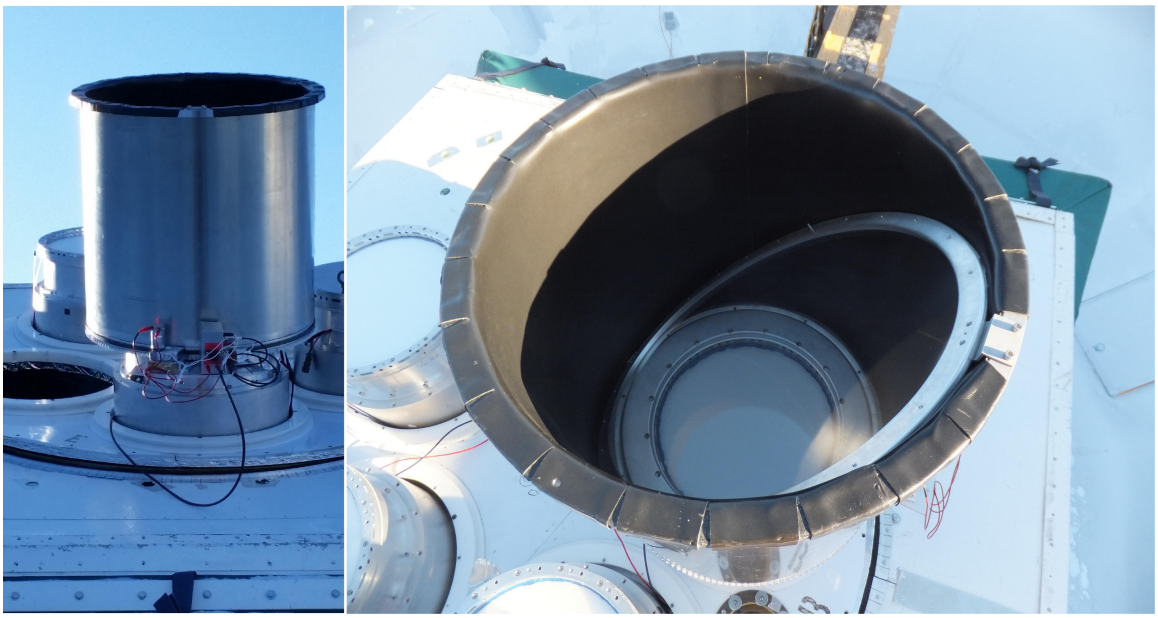

Figure 4.5: Two views of the Dielectric Sheet Calibrator on a *Keck Array* receiver. The image on the left shows the motor, gear, and magnetic scale of the encoder. The image on the right shows the dielectric sheet held in an elliptical ring clamp. In both pictures, the regular forebaffles have been removed for summertime operations. Two of the receivers have been removed for focal plane upgrades in the picture on the left.

4.2.1 Design Requirements

The mounts for BICEP1, BICEP2, and the *Keck Array* can slew in azimuth and declination. The mounts can also rotate about the boresight of the telescope, called a deck rotation. The calibrators in Refs. [73] and [74] were centered on the deck rotation axis, and the deck and azimuth axes counter-rotated to spin the calibrator while the detectors "saw" a fixed point on the sky. Because the *Keck* receivers are not centered on the deck rotation axis (see Figure 2.2), the mount axes can not be used to rotate the DSC in the same fashion. Instead, the calibrator was redesigned to rotate independently of the telescope mount.

To rotate independently, we added gears, a motor, and an encoder. The gears have semicircular teeth because it's a simple and effective design that is easy to machine. The driven gear is a 24 inch diameter, $\sim$1 in. wide annulus made of aluminum. The driving gear is made of high-density polyethylene. We chose a plastic driving gear to reduce wear on the larger driven gear. The gear ratio in this system is 11.3. For the motor, we use a 0.02 hp compact gearmotor with a maximum continuous speed of 25 rpm, though we typically operated at 20–25% of maximum. To record the angle of the DSC as it rotates, we affixed a magnetic tape[1] to the rotating stage and an encoder readhead[2] to a stationary support. The scale is $\sim$2 m in length with a 5 μm resolution, corresponding to $\sim$0.1 millidegrees when wrapped into a complete circle.

Another design requirement is that the DSC must operate outdoors at the South Pole. Even though we only use the calibrator during the austral summer, temperatures can drop to -40 °C. Differential thermal contraction is therefore a concern. The DSC baffle, dielectric sheet clamping ring, and the mounting structure are all machined from aluminum to match the shell of the cryostat. As pointed out in reference [73], the BOPP has a larger coefficient

[1] Renishaw model MS10B www.renishaw.com
[2] Renishaw model LM13 www.renishaw.com

of thermal expansion (CTE) than aluminum. However, in reference [73], they found that the plastic film would contract quicker than the aluminum. When the aluminum was equilibrated with the ambient temperature, the film would be loose. We implemented a simple stretching device, shown in Figure 4.6. The film is first taped to a plywood frame. One half of the elliptical clamping ring for the dielectric sheet is placed on blocks so that the plywood frame with film hangs under gravity. The weight of the wooden frame is enough to make the film taut interior to the ring. When the two pieces of the ring are fastened together, the film is clamped and further tightened. This method produced a tighter, flatter dielectric sheet than we were able to obtain through hand-stretching. With this method, the plastic remained tight both indoors and outdoors.

Another concern of differential thermal contraction arises between the magnetic encoder scale and the aluminum ring to which it's mounted. At -40 °C, the circumference of the aluminum ring is expected to contract 2 mm more than the scale. During the 2014/2015 austral summer, the scale was applied to the ring with a high-strength adhesive backing. We expected the failure point of adhesion to occur where the tape ends join, so we applied an epoxy at the joint. After it was outside for an hour, the scale buckled off the ring over a length of about 50 mm. The scale returned to normal after we brought it back inside. Then it lost adhesion again, though in a different location, when we returned it outside. This creates an error in the absolute angle of the calibrator where the angle from the encoder changes too fast over the buckled-out portion and too slow over the rest. We therefore were only able to do a single calibration run before bringing the DSC inside to warm.

For the 2015/2016 summer, we upgraded the magnetic scale mounting method. A metal strip with many spring elements[3] and an adhesive backing was attached to the aluminum

[3]Renishaw Spring Wrap-up www.renishaw.com

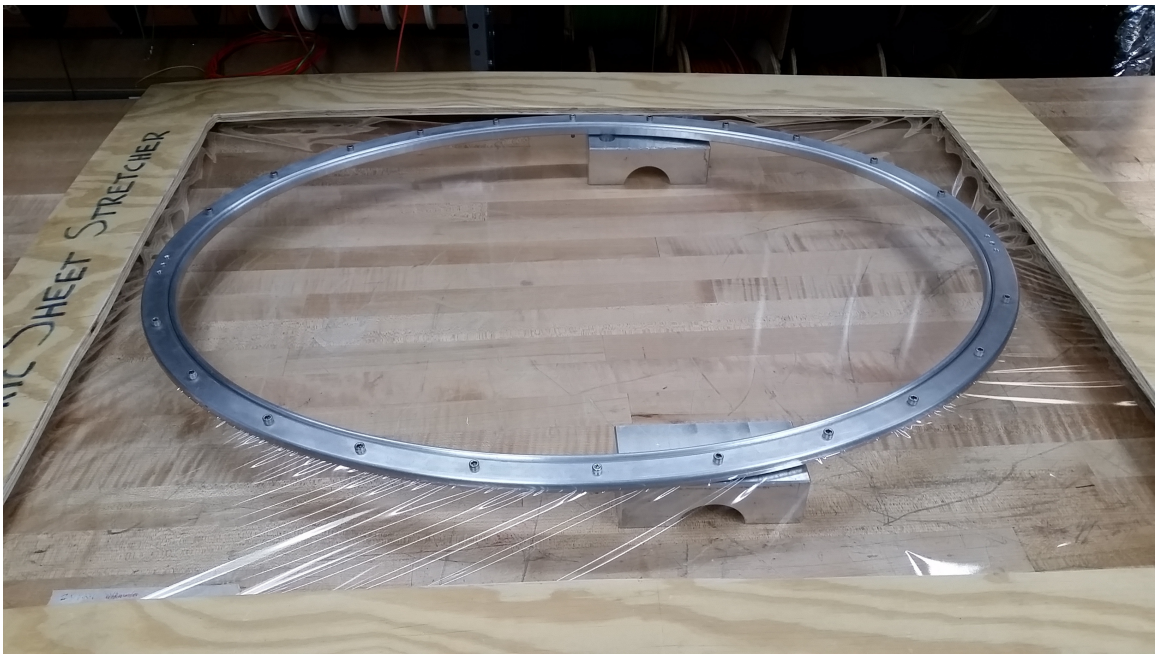

Figure 4.6: The apparatus for stretching the dielectric sheet taut. The sheet is first taped on the plywood frame and then hung over the elevated elliptical ring.

ring. The magnetic scale was then applied over the springs, compressing them slightly. The compression was enough to take up the differential thermal contraction between the scale and aluminum ring, even when operated at -40 °C.

4.2.2 Calibration Procedure

The DSC is mounted to a *Keck* receiver in two stages. The first stage is the base with the turntable, driven gear, motor, and encoder system. The inner ring of the turntable attaches to an adapter plate which mounts to the front of the cryostat. The second stage is the baffle with the dielectric sheet, which mounts on the outer ring of the turn table. With the DSC attached to a receiver, the telescope is slewed to an elevation of about 45°. Then the calibrator is rotated with the gear and motor until the minor axis of the dielectric sheet is nearly perpendicular

to the local gravity vector. We then take a series of angle measurements using a digital protractor[4] that we nominally align with the sheet's minor axis using a special measuring bar so that we don't touch the dielectric sheet. We record these angle measurements along with the current encoder reading so that we can later convert encoder counts to the DSC rotation angle. We then place the protractor on the elliptical ring, align it with the sheet's major axis, and record another series of measurements. These measurements are used to determine an aspect of the dielectric sheet orientation, which will be explained in Section 4.3.

With the initial position of the DSC measured, we now record the detector data. The telescope performs a nod in elevation to inject a signal of calculable amplitude. This is done to measure the differential gain between the two detectors of a pair, as described in Section 3.1.2. Then we slew the telescope in elevation to point near Zenith, and then rotate the DSC at a rate of about 0.5 rpm for 3 revolutions. Afterwards, we capture another nod in elevation to verify consistency with the first elnod. Both of the elnods are centered at a zenith angle of 30°. Lastly, we again slew the telescope to $\sim$45° elevation, rotate the DSC until the dielectric sheet is nearly horizontal, record the minor axis angle and encoder position, and measure the sheet tilt. The angle measurements recorded before and after the DSC rotation are averaged.

4.3 Calibrator Geometry

In order to fit the detector polarization angles using the DSC, we need an accurate model for the orientation of the dielectric sheet and the detector pointings. With such a model, we can calculate the expected transmitted and reflected power through and off the sheet. The detector pointings are straight-forward and come from the CMB-derived pointings

[4]Mitutoyo Pro 3600 www.mitutoyo.com/

discussed in Section 3.2. Calculating the orientation of the dielectric sheet is the subject of the following sub-sections. Calculating the expected calibration signal will be discussed in Section 4.4.

4.3.1 Matrix-Based Model

We will define two methods for calculating the dielectric sheet orientation. The first is presented in this sub-section and uses rotation matrices to rotate a set of initial vectors that define the orientation of the dielectric sheet at each step during the calibration. This model is slightly revised from that used in Randol Aikin's thesis [74]. The second model, which can rotate the initial vectors about arbitrary vectors, will be presented in the next sub-section.

We begin by defining our coordinate frame for this first model. The coordinate axes $\hat{\mathbf{x}}, \hat{\mathbf{y}}, \hat{\mathbf{z}}$ are fixed to the telescope mount and are shown in Figure 4.7. The axis $\hat{\mathbf{x}}$ is aligned with the elevation axis of the telescope, $\hat{\mathbf{z}}$ is aligned with the deck axis, and $\hat{\mathbf{y}} = \hat{\mathbf{z}} \times \hat{\mathbf{x}}$. It is also useful to define the elevation angle e of the telescope, where $e = 90°$ anti-aligns $\hat{\mathbf{z}}$ with gravity, $\hat{\mathbf{g}}$. An increase in e is a negative rotation about $\hat{\mathbf{x}}$ in this coordinate system. We also define three vectors which are fixed to the dielectric sheet. $\hat{\mathbf{n}}$ is the sheet's normal vector, $\hat{\mathbf{M}}$ is aligned with the sheet's major axis, and $\hat{\mathbf{m}}$ is aligned with the sheet's minor axis. These vectors are shown on the right side of Figure 4.7.

Angles used in our model are also shown in Figure 4.7. The angles t, γ, and ϕ are rotations about $\hat{\mathbf{x}}$, $\hat{\mathbf{M}}$, and $\hat{\mathbf{z}}$, respectively. We can apply the following rotation matrices to orient the dielectric sheet.

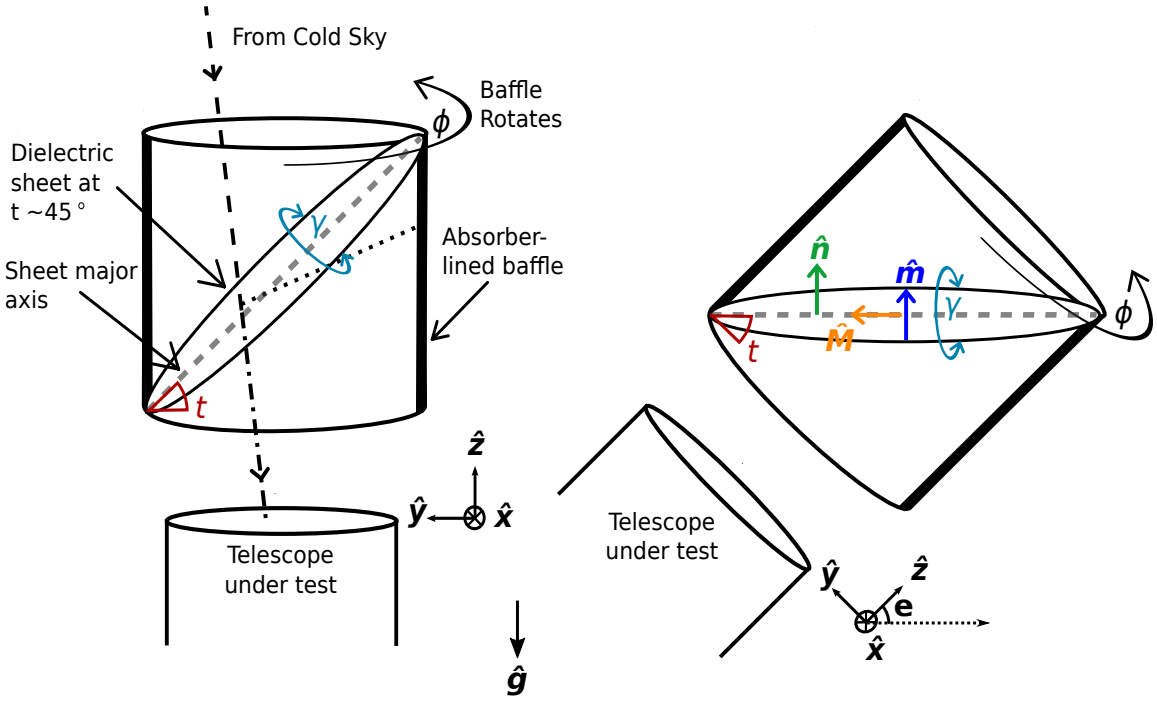

Figure 4.7: *Left*: Schematic of the DSC, similar to Figure 4.4, with the telescope pointing to Zenith. *Right*: Telescope elevation at $e = 45°$ showing that the coordinate system is fixed to the telescope in this model. This also shows the three angles and three vectors that describe the orientation of the dielectric sheet.

$$\mathrm{R}_t = \begin{bmatrix} 1 & 0 & 0 \\ 0 & \cos t & -\sin t \\ 0 & \sin t & \cos t \end{bmatrix}, \mathrm{R}_\gamma = \begin{bmatrix} \cos\gamma & 0 & \sin\gamma \\ 0 & 1 & 0 \\ -\sin\gamma & 0 & \cos\gamma \end{bmatrix}, \mathrm{R}_\phi = \begin{bmatrix} \cos\phi & \sin\phi & 0 \\ -\sin\phi & \cos\phi & 0 \\ 0 & 0 & 1 \end{bmatrix} \tag{4.1}$$

We are free to choose any starting orientation for the sheet, but the angles t, γ, and ϕ must then reference this orientation. When these three angles are all 0°, our choice aligns $\hat{\mathbf{n}}$ with $\hat{\mathbf{z}}$, $\hat{\mathbf{M}}$ with $\hat{\mathbf{y}}$, and $\hat{\mathbf{m}}$ with $\hat{\mathbf{x}}$. The angles t and γ are set during installation, so the only angle that changes[5] during a calibration is ϕ. The complete set of rotations is

$$\hat{\mathbf{v}} = \hat{\mathbf{v}}_0 \mathrm{R}_\gamma \mathrm{R}_t \mathrm{R}_\phi, \tag{4.2}$$

where $\hat{\mathbf{v}}_0$ is one of the vectors $\hat{\mathbf{n}}$, $\hat{\mathbf{M}}$, or $\hat{\mathbf{m}}$ before applying any rotation matrix. With the order of Equation (4.2), we keep the coordinate system fixed and follow $\hat{\mathbf{v}}_0$ as it rotates in the coordinate frame. R_t and R_γ are left-handed rotations of $\hat{\mathbf{v}}_0$ about $\hat{\mathbf{x}}$ and $\hat{\mathbf{y}}$, respectively. A positive angle in R_ϕ is a right-handed rotation of $\hat{\mathbf{v}}_0$ about $\hat{\mathbf{z}}$. The vectors after rotation are then

$$\hat{\mathbf{m}} = \begin{bmatrix} \cos\gamma\cos\phi - \sin\gamma\sin\phi\sin t \\ \cos\gamma\sin\phi + \cos\phi\sin\gamma\sin t \\ \cos t\sin\gamma \end{bmatrix}^T \tag{4.3}$$

$$\hat{\mathbf{M}} = \begin{bmatrix} -\cos t\sin\phi \\ \cos\phi\cos t \\ -\sin t \end{bmatrix}^T \tag{4.4}$$

$$\hat{\mathbf{n}} = \begin{bmatrix} -\cos\phi\sin\gamma - \cos\gamma\sin\phi\sin t \\ \cos\gamma\cos\phi\sin t - \sin\gamma\sin\phi \\ \cos\gamma\cos t \end{bmatrix}^T. \tag{4.5}$$

To determine the reflected and transmitted powers, we need only keep track of $\hat{\mathbf{n}}$, assuming

[5] in a perfect system

the sheet is planar. However, with *Keck* we use a digital protractor to measure t and the starting (and ending) value of ϕ by aligning the protractor with $\hat{\mathbf{M}}$ and $\hat{\mathbf{m}}$ when the telescope is rotated to an elevation of 45° as is shown on the right side of Figure 4.7. We'd also like to measure γ, but the obvious method of aligning the protractor with $\hat{\mathbf{m}}$ when $\hat{\mathbf{M}}$ is perpendicular to gravity doesn't work because γ and ϕ are degenerate in this orientation. Typically we don't directly measure t, or the starting ϕ for two reasons. First, the protractor measures angles with respect to gravity,[6] not $\hat{\mathbf{z}}$. Second, applying R_t after R_γ changes the orientation of $\hat{\mathbf{m}}$ with respect to gravity, even if $\hat{\mathbf{z}}$ is aligned with gravity.[7] The discrepancy can be accounted for by keeping track of the vectors $\hat{\mathbf{M}}$ and $\hat{\mathbf{m}}$, as well as the gravity vector $\hat{\mathbf{g}}$ in our coordinate frame. In our coordinate system, $\hat{\mathbf{g}}$ depends only on the elevation of the telescope mount, depicted as e in Figure 4.7. Then

$$\hat{\mathbf{g}} = \begin{bmatrix} 0 & -\cos e & -\sin e \end{bmatrix}, \quad 0° \leq e \leq 90°. \tag{4.6}$$

.

To calculate the expected protractor measurement θ of a vector $\hat{\mathbf{v}}$ in the plane of the sheet, we can use the angle between it and $\hat{\mathbf{g}}$. The expected protractor measurement is

$$\theta = \cos^{-1}(\hat{\mathbf{v}} \cdot \hat{\mathbf{g}}) - 90°. \tag{4.7}$$

The subtraction of 90° arises because the protractor reads the angle from horizontal, not $\hat{\mathbf{g}}$.

[6] For the protractor we use, this is strictly only true when the cross-axis is near level. At a 5° cross-axis tilt, the protractor reading changes by $\sim 0.^\circ 1$.

[7] One may want to change the order of R_t and R_γ, which is fine, but then the second rotation changes the orientation of $\hat{\mathbf{M}}$ with respect to gravity.

For the minor and major axes, the expected protractor measurements are then

$$\theta_m = \cos^{-1}\left(-\cos e\left(\cos\gamma\sin\phi + \cos\phi\sin\gamma\sin t\right) - \sin e\cos t\sin\gamma\right) - 90° \tag{4.8}$$

$$\theta_M = \cos^{-1}\left(-\cos e\cos\phi\cos t + \sin e\sin t\right) - 90°. \tag{4.9}$$

In the case where $\phi = 0$ and[8] $e = 90° - t$, we then expect to measure $\theta_m = \gamma$ and $\theta_M = 0°$. If instead $\phi = 0$ and $e = 90°$, Equations (4.8) and (4.9) reduce to $\theta_m = \cos^{-1}(-\cos t\sin\gamma) - 90°$ and $\theta_M = t$. To avoid ambiguity in the sign of the angle we measure, we must be careful to reckon between the rotation of the protractor with respect to gravity and the effect of a positive or negative ϕ or γ rotation.

It is not practical to make measurements of t and γ for every value of ϕ, so we only use one value for those two angles throughout the calibration. That means this model constrains the rotation axis of the DSC to $\hat{\mathbf{z}}$. If we wish to allow for a different rotation axis, we'd need to calculate a new, more complex rotation matrix for $\boldsymbol{R}_\phi$. Therefore, the use of rotation matrices is less flexible than the model we'll present next. On the other hand, the use of rotation matrices allows us an easier method of calculating the dependence of the protractor measurements on the elevation of telescope and the three orientation angles of the dielectric sheet, t, γ, and ϕ, as shown in Equations (4.8) and (4.9).

4.3.2 Vector-Based Model

The second method for tracking the orientation of the dielectric sheet uses a system of vectors to describe components of the *Keck Array*. We break down each vector into a unit vector, a length, and a starting or hanging point. Cylindrical components, which include the telescope

[8]This takes care of the interaction between e and t. If $\gamma = 0°$, $\phi = 0°$, and $t = 30°$, then we expect we'd need to rotate the telescope to an elevation of 60° to make $\hat{\mathbf{n}}$ parallel with $\hat{\mathbf{g}}$ and get a protractor measurement of 0°.

drum (see Figure 2.2), cryostat shells for the five receivers, and DSC baffle, are represented by vectors aligned with their cylindrical axis, and the lengths are chosen to reflect the relative heights of the the physical telescope and calibrator. The beam pointings are also represented by vectors. The dielectric sheet in this model has the same vectors ($\hat{\mathbf{n}}$, $\hat{\mathbf{m}}$, and $\hat{\mathbf{M}}$) as the previous model as shown on the right side of Figure 4.7.

We use Rodrigues' rotation formula to rotate the appropriate vectors about another vector:

$$\mathbf{v} = \mathbf{v_0}\cos\theta \ + (\hat{\mathbf{a}} \times \mathbf{v_0})\sin\theta \ + \hat{\mathbf{a}}(\hat{\mathbf{a}} \cdot \mathbf{v_o})(1 - \cos\theta), \tag{4.10}$$

where $\mathbf{v_0}$ is the initial vector to be rotated by angle θ about unit vector $\hat{\mathbf{a}}$. So that we can make a 3-D rendering of the telescope and calibrator, we also rotate the starting points[9] of the vectors about $\hat{\mathbf{a}}$ by inserting the point into $\mathbf{v_0}$ in the above equation. The 3-D rendering allows us to verify that all of the model components are rotated about a vector as expected, both in magnitude and direction. For example, changing the elevation of the telescope model should rotate every component, but rotating the calibrator should only rotate the DSC baffle and dielectric sheet (including the major and minor axes).

Another difference between this model and the one presented in the preceding sub-section is that the coordinate frame is external to the telescope. The z-axis is anti-aligned with gravity, but the x- and y-axes are somewhat arbitrary. All vectors are set up in this coordinate frame. Changing the elevation of the telescope model is done about the x-axis, and the telescope is not allowed to move in azimuth. This is acceptable since an azimuth rotation doesn't alter the relative orientation of the dielectric sheet vectors (or the detector pointing vectors, which will be introduced in Section 4.4) with respect to gravity (if we wanted that capability, we would keep track of an additional vector that we would align with the

[9]The starting point is actually another vector, but we don't break it down into a unit vector.

telescope's elevation rotation axis).

In this model, t is a rotation of the dielectric sheet about $\hat{\mathbf{m}}$, γ is a rotation about $\hat{\mathbf{M}}$, and ϕ is a rotation about DSC baffle's cylindrical axis. In standard usage of this model, the cylindrical axis of the baffle is aligned with the telescope's boresight, in which case ϕ has the same effect on the dielectric sheet's orientation as it did in the matrix-based model.

The model presented in this sub-section is a new take on tracking the geometry of the DSC. It offers an easier exploration of systematic uncertainties, which we'll discuss in Section 4.5, than the pre-defined rotation matrices. We therefore use this new model in our analysis of the DSC calibration data acquired on the *Keck Array* telescope.

4.4 Polarization Signal

As the DSC rotates, the incident angles of the beams with the dielectric sheet vary, changing the amount of reflected and transmitted power that couples to a given detector. In the previous section, we showed our method for tracking the dielectric sheet's orientation. We now use that information to determine the expected reflected power of radiation off the front, r_1, and back, r_2, of the dielectric sheet by using the Fresnel equations (see, e.g., [25]):

$$r_{1,\mathrm{s}} = \frac{\cos\theta_\mathrm{i} - n_\mathrm{d}\cos\theta_\mathrm{t}}{\cos\theta_\mathrm{i} + n_\mathrm{d}\cos\theta_\mathrm{t}}, \quad r_{2,\mathrm{s}} = -r_{1,\mathrm{s}} \tag{4.11}$$

$$r_{1,\mathrm{p}} = \frac{n_\mathrm{d}\cos\theta_\mathrm{i} - \cos\theta_\mathrm{t}}{n_\mathrm{d}\cos\theta_\mathrm{i} + \cos\theta_\mathrm{t}}, \quad r_{2,\mathrm{p}} = -r_{1,\mathrm{p}}, \tag{4.12}$$

where r_s and r_p are the reflected portions of the beam polarized perpendicular and parallel to the incidence plane, n_d is the index of refraction of the dielectric sheet, θ_i is the angle between the beam and the dielectric sheet plane, θ_t is the angle in the dielectric sheet, and the index of refraction for air has been taken as 1 and is omitted from the equations. Some

texts use the symbols $\perp$ and $\parallel$ or equivalently TE and TM in place of s and p to represent the polarization states that are perpendicular and parallel to the plane of incidence. The letter s comes from the German word for perpendicular, "senkrecht." The total reflection, R, for the s- and p-polarizations is the superposition of all reflections off the front and back surfaces of the dielectric:

$$R = \frac{r_1^2 + r_2^2 + 2r_1 r_2 \cos\beta}{1 + r_1^2 r_2^2 + 2r_1 r_2 \cos\beta}. \tag{4.13}$$

Using the relation between r_1 and r_2 in Equations (4.11) and (4.12), we can simplify R to

$$R = \frac{2r^2(1 - \cos\beta)}{1 + r^4 - 2r^2 \cos\beta}, \tag{4.14}$$

where $r_{1,\mathrm{s}}$ and $r_{1,\mathrm{p}}$ can be plugged in for r to determine R_s and R_p, respectively. The angle β is the phase shift between the reflections off the front and back surfaces of the dielectric sheet:

$$\beta = \frac{4\pi n_\mathrm{d} d \cos\theta_\mathrm{t}}{\lambda}, \tag{4.15}$$

where d is the thickness of the sheet and λ is the wavelength of the radiation.

We also need to calculate the coupling of R_s and R_p to our detectors. We begin with a unit vector for a given detector's pointing, $\hat{\mathbf{b}}_0$. The reflected vector $\hat{\mathbf{b}}_\mathrm{r}$ is

$$\hat{\mathbf{b}}_\mathrm{r} = \frac{\hat{\mathbf{b}}_0 - 2\left(\hat{\mathbf{b}}_0 \cdot \hat{\mathbf{n}}\right)\hat{\mathbf{n}}}{|\hat{\mathbf{b}}_0 - 2\left(\hat{\mathbf{b}}_0 \cdot \hat{\mathbf{n}}\right)\hat{\mathbf{n}}|}. \tag{4.16}$$

During the calibration, $\hat{\mathbf{b}}_0$ is constant for a given detector, but $\hat{\mathbf{b}}_\mathrm{r}$ changes due to its dependence

on the normal vector of the dielectric sheet. We now calculate the unit vectors $\hat{\mathbf{s}}$ and $\hat{\mathbf{p}}$ for the s- and p- polarizations in the plane of incidence:

$$\hat{\mathbf{s}} = \frac{\hat{\mathbf{b}}_0 \times \hat{\mathbf{b}}_\mathrm{r}}{|\hat{\mathbf{b}}_0 \times \hat{\mathbf{b}}_\mathrm{r}|} \tag{4.17}$$

$$\hat{\mathbf{p}} = \frac{\hat{\mathbf{b}}_0 \times \hat{\mathbf{s}}}{|\hat{\mathbf{b}}_0 \times \hat{\mathbf{s}}|}. \tag{4.18}$$

Note that $\hat{\mathbf{s}}$ is normal to the plane of incidence and $\hat{\mathbf{p}}$ is perpendicular to $\hat{\mathbf{s}}$, meaning it's in the plane of incidence. Both vectors are orthogonal to $\hat{\mathbf{b}}_0$. Now we project a detector's polarization vector $\hat{\mathbf{g}}$ into the $\hat{\mathbf{s}}$–$\hat{\mathbf{p}}$ basis:

$$\mathbf{g}_\mathrm{s} = (\hat{\mathbf{g}} \cdot \hat{\mathbf{s}})\,\hat{\mathbf{s}} \tag{4.19}$$

$$\mathbf{g}_\mathrm{p} = (\hat{\mathbf{g}} \cdot \hat{\mathbf{p}})\,\hat{\mathbf{p}}. \tag{4.20}$$

We now couple the vectors in Equations (4.19) and (4.20) to the total reflected power (subscript r) and transmitted power (subscript t) in the s- and p-polarization states using the assumption that the radiation is only transmitted or reflected:

$$\mathbf{A}_\mathrm{s,r} = \mathbf{g}_\mathrm{s}\sqrt{R_\mathrm{s}} \tag{4.21}$$

$$\mathbf{A}_\mathrm{s,t} = \mathbf{g}_\mathrm{s}\sqrt{1 - R_\mathrm{s}} \tag{4.22}$$

$$\mathbf{A}_\mathrm{p,r} = |\mathbf{g}_\mathrm{p}|\sqrt{R_\mathrm{p}}\left(\hat{\mathbf{s}} \times \hat{\mathbf{b}}_\mathrm{r}\right) \tag{4.23}$$

$$\mathbf{A}_\mathrm{p,t} = \mathbf{g}_\mathrm{p}\sqrt{1 - R_\mathrm{p}}. \tag{4.24}$$

The cross product in Equation (4.23) is necessary since the reflected p-polarization vector changes direction. $\mathbf{g}_\mathrm{p}$ is orthogonal to $\hat{\mathbf{s}}$ and $\hat{\mathbf{b}}_0$, but $\mathbf{A}_\mathrm{p,r}$ is orthogonal to $\hat{\mathbf{s}}$ and $\hat{\mathbf{b}}_\mathrm{r}$.

The expected signal for a single detector is

$$U = T_{\rm b}|\mathbf{A}_{\rm s,r} + \mathbf{A}_{\rm p,r}|^2 + T_{\rm sky}|\mathbf{A}_{\rm s,t} + \mathbf{A}_{\rm p,t}|^2, \tag{4.25}$$

where $T_{\rm b}$ and $T_{\rm sky}$ are the temperatures of the calibrator's baffle and the sky. U is the signal for a single rotation angle. The complete signal over all ϕ is denoted as S.

We want to rotate $\hat{\mathbf{g}}$ about $\hat{\mathbf{b}}_0$ until the model best matches the "per-detector" signal. However, we found that S doesn't account for the full "per-detector" signal recorded during the calibrations. The signal in excess of our model appears to be mostly common-mode between the detectors within a pair, so we fit the "per-pair" signal instead. The disagreement between the per-detector signal and model is discussed in Appendix A, and example per-detector signals and fits are shown in Figures A.2 to A.7.

To perform per-pair fits, we use the pair differenced signal. We simultaneously calculate S for both detectors (and take their difference) in the pair using separate vectors $\hat{\mathbf{b}}_0$ and $\hat{\mathbf{g}}$ for each detector that are based on their beam parameters. $\hat{\mathbf{b}}_0$ is similar for the detectors within a pair, but it's not required to be identical. The model allows the detectors in a pair to have any relative polarization angle, but we use the design value of 90°. Then we rotate each detector's $\hat{\mathbf{g}}$ about its pointing vector $\hat{\mathbf{b}}_0$ by the same amount, called the polarization rotation angle (or offset), to find the best fit. This means the polarization angles remain orthogonal. The full model has five parameters: baffle temperature, sky temperature, polarization rotation angle, a DC offset, and a nuisance parameter that allows for a linear drift in the bolometer data with time. However, the sky temperature and DC offset are highly degenerate, so we fix the sky temperature parameter at an approximate value and allow the DC offset parameter to vary.

Example calibration data with the best fit model is shown in Figure 4.8 for three detector pairs over approximately three revolutions of the calibrator. The top panel of this figure

shows the necessity of the linear nuisance parameter in the fit. This figure also shows that there are two local maxima (peaks) and two local minima (troughs) per revolution. The detector pair closest to the boresight has a nearly sinusoidal signal. Detector pairs at larger radii deviate from a sinusoid because the angle of incidence changes by a noticeable amount as the calibrator rotates. Figure 4.9 shows data from the same calibration run but for all of the well-behaved detector pairs and ordered by the detector pair's azimuthal angle in the focal plane. The signal for each pair is normalized by the fitted forebaffle temperature (fits are not shown), which serves as a proxy for the signal amplitude. For clarity, this figure only shows data for the first two revolutions of the DSC. We see that the troughs and peaks occur near the same DSC rotation angle for all detector pairs. This is due to the alignment of the polarization axes of the detectors in the focal plane. The axes are nominally aligned with the rectangular grid of the detector locations (see Figure 4.3). The s-polarization state couples with half of the detectors at similar DSC rotation angles, and it couples with the other half of the detectors when the DSC rotates by 90°. This figure also shows that the peak with the larger signal occurs at a rotation angle near 360° for pairs with azimuthal angles between 0° and 180° and occurs at a rotation angle near 180° for the other pairs. This makes sense because for pairs at azimuthal angles separated by 180° and the same radii, the geometry of the polarization axes, beam pointings, and dielectric sheet will be identical when the calibrator rotates 180°.

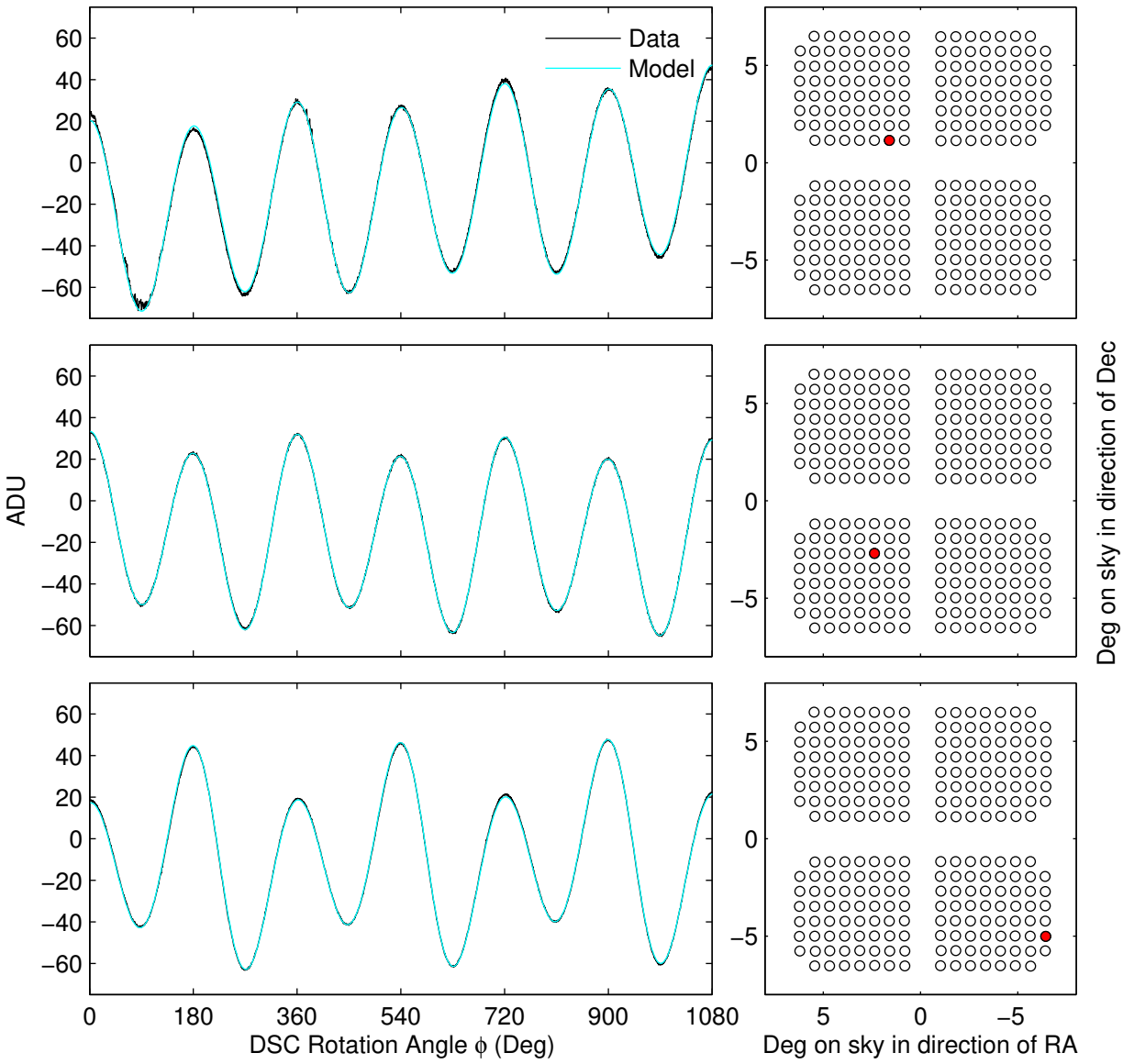

Figure 4.8: Example calibration data for three detector pairs over three revolutions of the DSC. The underlying dark (black) lines are the recorded data binned into about 0.°3 bins in ϕ. The lighter (cyan) lines are the best fit models. The right panels show the location of the detector pair on the sky with respect to the telescope boresight.

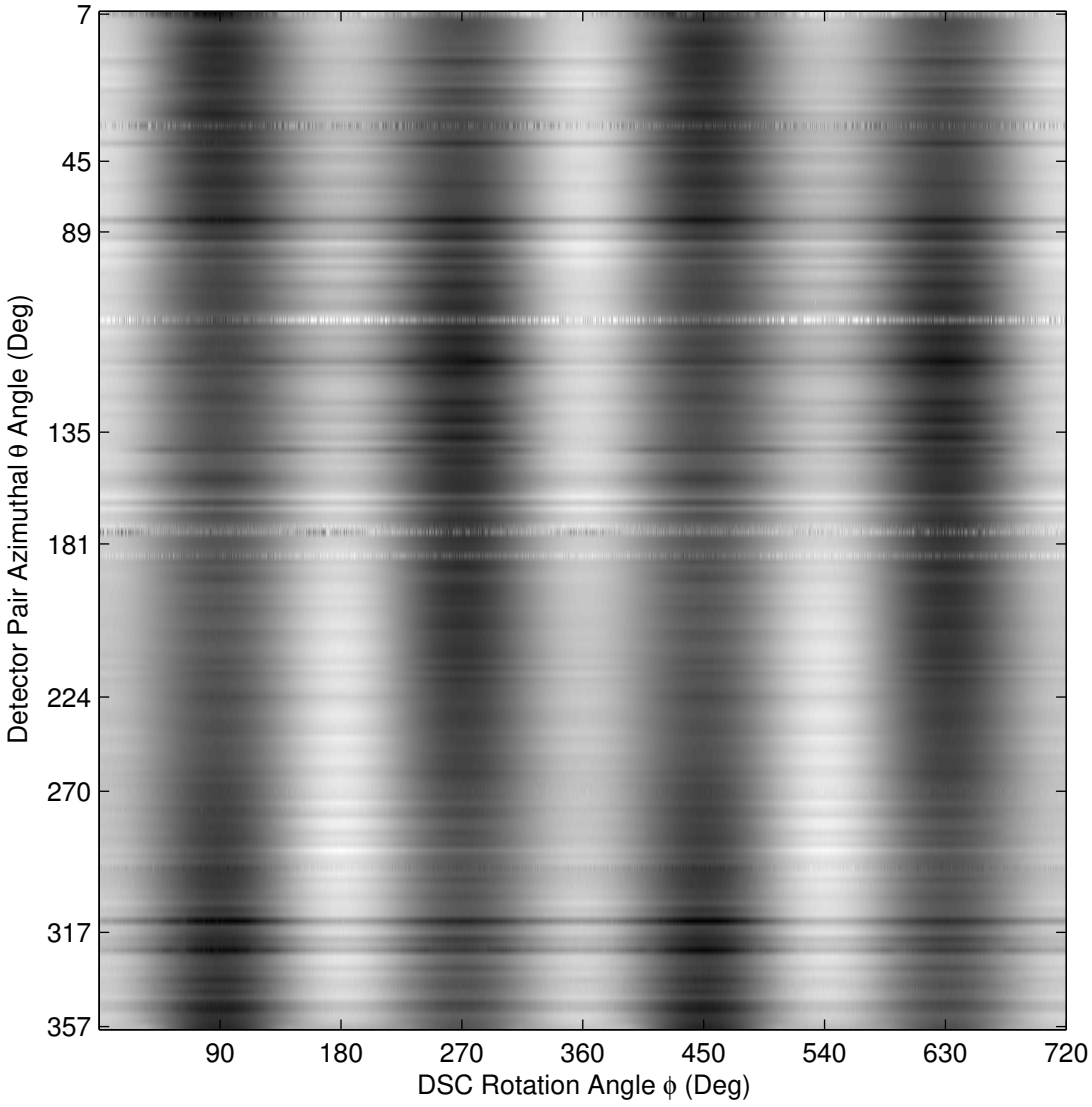

Figure 4.9: Example calibration data for most detector pairs of one receiver, ordered by their azimuthal angle. Two revolutions of data are shown.

4.5 Uncertainty Propagation

To exploit the full statistical power of the BICEP/*Keck* data, we want to measure our polarization angles to better than 0.1 degrees.[10] In this section we explore different measurement uncertainties and their effects on the derived polarization angles. For all except "Fit Uncertainty," we alter one physical aspect of the DSC, simulate the measurement without noise, and fit the simulation assuming the physical aspect is unaltered. We then calculate the difference between the simulated and fit polarization angles. We do this for all detector pairs in the focal plane. We also performed the simulations for 95 GHz, 150 GHz, and 220 GHz, but the results were nearly identical, so we only present the results of the 150 GHz simulations.

4.5.1 Fit Uncertainty

With this simulation we test the fitting algorithm, which is the Minuit fitting routine [75]. In this case, we simulate and fit the data using the same physical aspects. With a maximum difference between simulation and fit of $1\overset{\circ}{.}6 \times 10^{-5}$, the fitting routine is deemed acceptable.

4.5.2 Encoder Angle Uncertainty

We only have the magnetic encoder system to derive the relative angles of the calibrator as it rotates. If there is not a linear relation between encoder counts and rotation angle, the calculated DSC rotation angle will be inaccurate. Given the geometry of the DSC, the encoder manufacturer quoted a maximum angle error amplitude of $0\overset{\circ}{.}014$ when the outside temperature is $-30\ ^{\circ}C$. To test the effect of the angle error uncertainty, we round up the

[10] This is an ultimate goal, but measuring the polarization angles to better than 0.5 degrees would be an improvement over current methods.

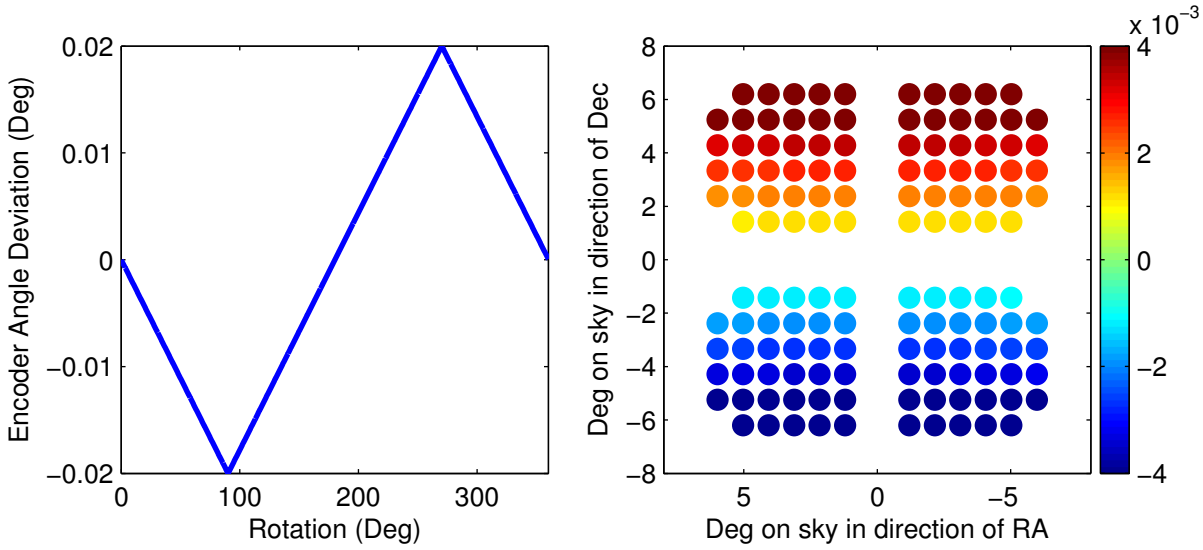

Figure 4.10: *Left*: Example of an error profile of the calculated DSC rotation angle ϕ. The extrema are based on the expected angle accuracy of the encoder as quoted by the manufacture. *Right*: The resulting fit errors for each detector pair in degrees, showing an edge-to-edge gradient. The errors are negligible.

quoted error amplitude to 0.°02 and choose an error profile that linearly increases or decreases between the extrema. The profile must start and end at 0°, and the integral must be 0, since we begin the measurement with the sheet in an externally measured position and know how many encoder counts are required to complete exactly one rotation of the DSC.[11] The simulated encoder angle error profile and the resulting fit errors are shown in Figure 4.10. There is a gradient in the fit errors across the focal plane that we expect is present because the polarization axes of the detectors are aligned in the focal plane, but the maximum fit error is only ±0.°004.

[11] We know the length and resolution of the encoder tape, and we verified that we record the expected number of counts between successive crossings of a reference mark.

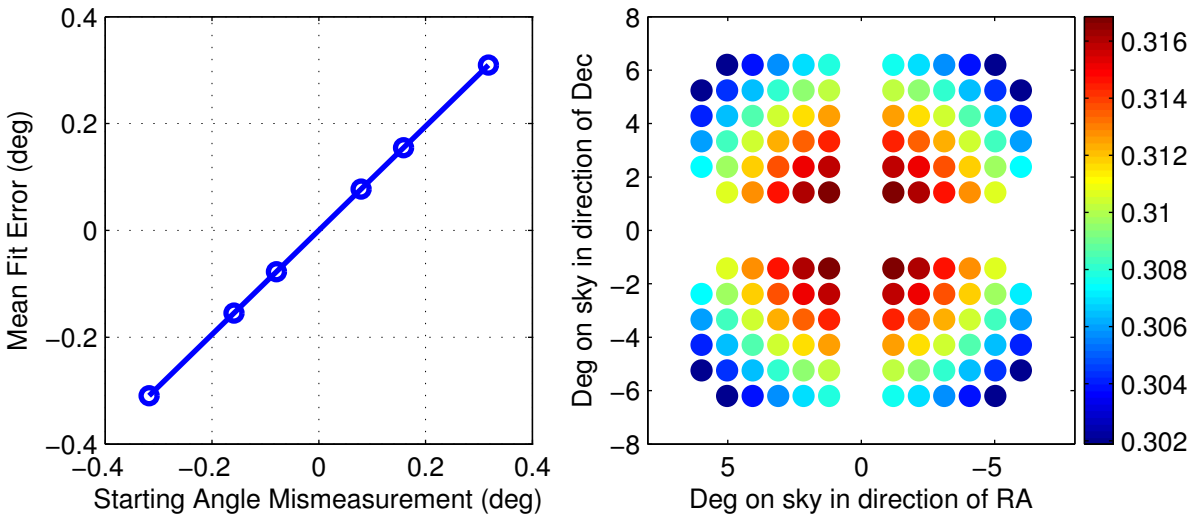

Figure 4.11: *Left*: Mean polarization fit error over all detector pairs from mismeasuring the starting ϕ angle. *Right*: The fit errors for each detector pair in degrees when the starting angle is mismeasured by $\sim 0.^{\circ}32$. Detectors closer to the center of the focal plane are affected slightly more, and the errors are significant.

4.5.3 Protractor Uncertainty

We use a digital protractor to determine the starting rotation angle of the DSC, and this may be a source of systematics in measuring our detectors' polarization angles. On the left side of Figure 4.11 we show the average fit error as a function of a mismeasurement in the starting angle due to the protractor uncertainty. The slope of the line is 0.97. The slope is smaller than 1 because the shape of the signal for an off-axis pair changes when the polarization axis is rotated, meaning that an offset in the DSC rotation angle can't be compensated for by rotating the polarization angle. This is the source of the small radial gradient where the detectors close to the center of the focal plane have the largest absolute error resulting from the protractor uncertainty.

We measure ϕ with a digital protractor and aim to minimize the statistical uncertainty by taking multiple measurements. We also aim to minimize the systematics by calibrating the

protractor often, taking measurements with the protractor display facing toward and away from us, and taking measurements with the cross axis of the protractor perpendicular (to within a degree or two) to gravity. With these precautions, we estimate that the uncertainty in ϕ from the protractor measurements is likely $< 0.^{\circ}01$ and certainly $< 0.^{\circ}05$, which results in similar errors on the average polarization angle across the detectors in a focal plane.

4.5.4 Tilt Uncertainty

In these simulations, we test the uncertainty of the tilt angle, t. The tilt is measured with a digital protractor, so we expect it's accurate to much better than 1° given the accuracy of the protractor, which the manufacturer states is $0.^{\circ}05$. We nonetheless investigate the effects of a mismeasurement over a range of $\pm 2^{\circ}$. Figure 4.12 shows the results and demonstrates that if we mismeasure the tilt of the dielectric sheet, we can still accurately fit the average polarization angle over a focal plane. Even if we mismeasure the tilt by an unrealistic -2°, the maximum polarization angle fit error for a single pair is still negligible at $0.^{\circ}002$.

4.5.5 Thickness Uncertainty

In the *Keck* DSC we use a 0.9 mil (0.0009 in.) thick BOPP film for the dielectric. In this section we check for any errors that result if the actual thickness were between 0.7 and 1.2 mil. We produce the simulated data with these ranges of thickness and fit the data assuming the thickness is 0.9 mil. Figure 4.13 shows the average error. The maximum error for a single detector is 1.1×10^{-4} degrees and occurs when the actual thickness is 1.2 mil. The simulations for thickness effects assume a uniform thickness. We did not test the effect of thickness variations in the dielectric sheet. Since the detectors receive radiation transmitting through and reflecting off a large area of the sheet, we expect any effects from random

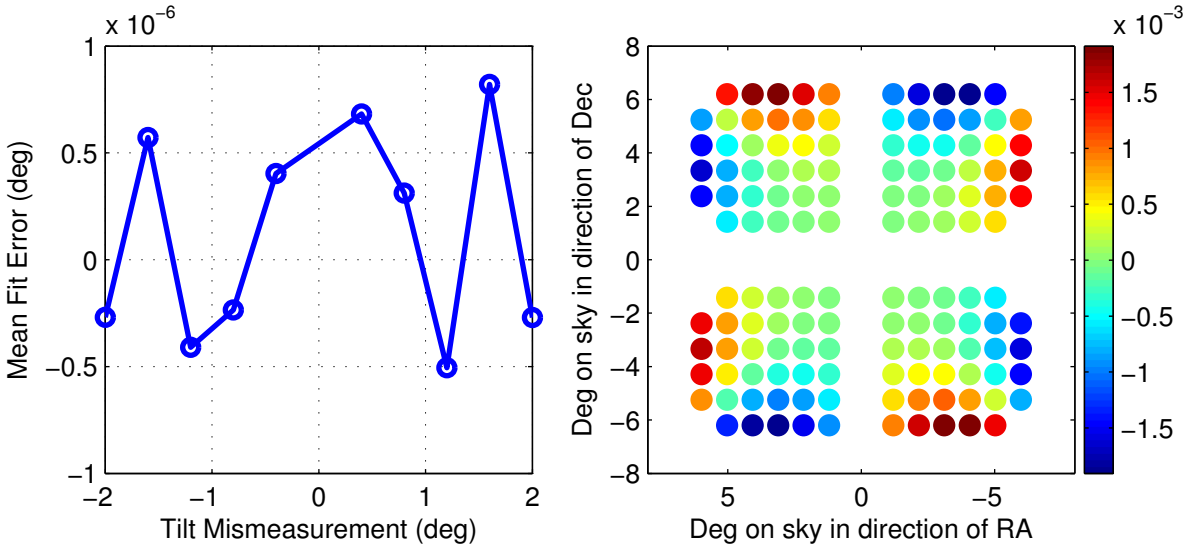

Figure 4.12: *Left*: Mean polarization fit error over all detector pairs when the tilt, t, of the dielectric sheet is mismeasured. *Right*: The fit errors for each detector in degrees when t is mismeasured by $-2°$. The errors are negligible.

thickness variations will average down.

4.5.6 Gamma Uncertainty

In this sub-section, we investigate the errors in the polarization angle fits that are caused by mismeasuring the angle γ, the rotation of the dielectric sheet about its major axis (see Figure 4.7). We don't yet have a reliable method to measure this angle, which is 0° by design. A mismeasured γ angle affects the dielectric sheet's modeled normal vector, but it also affects the starting angle measurement of the DSC. Both of these effects are included in this test. Figure 4.14 shows the average fit error versus γ angle mismeasurement. The slope is 0.17. From machining accuracy, we estimate that $|\gamma| < 0.^{\circ}6$, which results in a maximum fit error of $\pm 0.^{\circ}1$.

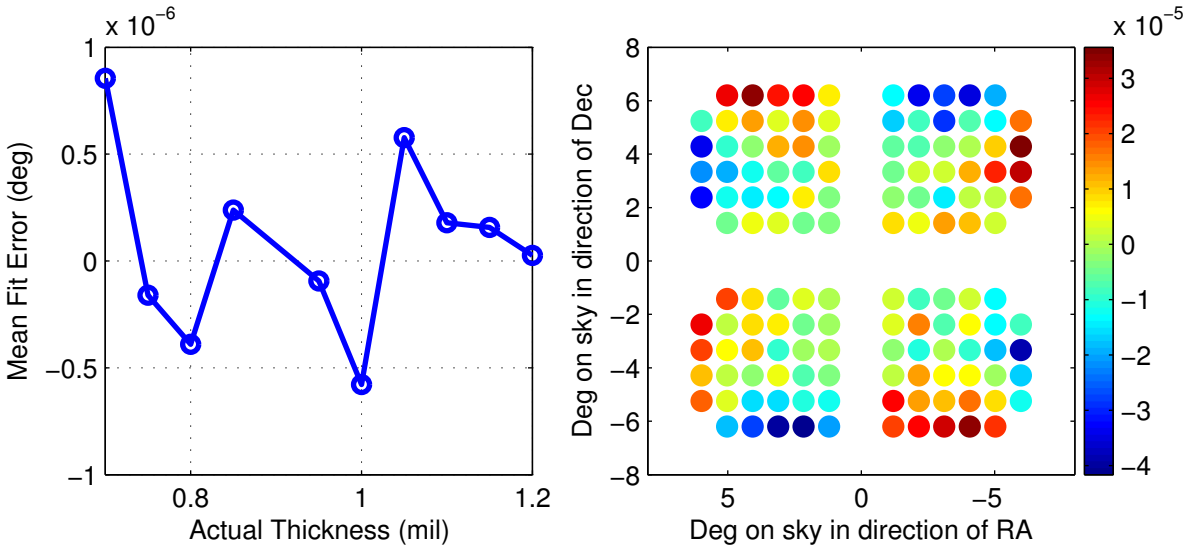

Figure 4.13: *Left*: Mean polarization fit error across the focal plane when an incorrect dielectric thickness is used in the fit model. *Right*: The fit errors for each detector pair in degrees when the dielectric thickness is really 1.2 mil but the model uses a thickness of 0.9 mil. There is no clear pattern across the focal plane because the errors are small enough that we see the contribution of the fitting routine uncertainty.

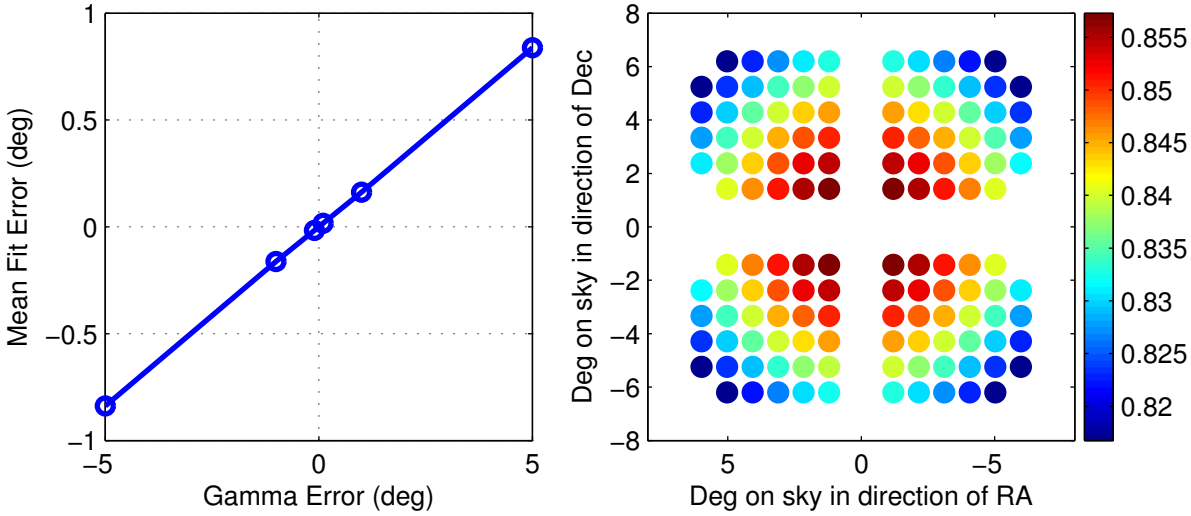

Figure 4.14: *Left*: Mean polarization fit error across the focal plane when γ is assumed to be 0° but is really between −5° and 5°. The slope of the line is 0.17. *Right*: The fit errors for each detector in degrees when γ is assumed to be 0° but is really 5°. This source of error is potentially significant.

4.6 Consistency Tests

During the 2015/2016 summer, we ran a set of consistency tests to see if changing some aspect of the DSC changed the polarization angle fits. Any change in the fits could indicate that the measurement procedure does not adequately measure the starting orientation of the dielectric sheet. Table 4.1 outlines the tests (as well as additional information that will be explained later in this section). Test 1 was the initial test. Between tests 1 and 2, the DSC was removed from the telescope and reinstalled a day later. Tests 2 and 3 were performed back-to-back without changing the calibrator setup. With test 4, we rotated the baffle 80° with respect to the encoder tape. In test 5, we rotated the baffle back to the same position as all of the other test and rotated the telescope mount deck angle by 20°. For test 6, we disassembled and reassembled the sub-components of the DSC base. For test 7 we rotated the telescope mount in Azimuth by 90°. Finally in the 8$^{\text{th}}$ test, we replaced the dielectric sheet with another piece of BOPP film from the same stock, which also means we removed and reinstalled the sheet holder. Example data and fits from test 1 are shown for three detector pairs in Figure 4.8, and data for all well-behaved detector pairs from test 1 is shown in Figure 4.9.

As described in Section 4.4, we fit a five-parameter model to the binned data. We use a chi-square minimization routine, and we use the standard deviation of the points within each bin as an estimate of the uncertainty on each bin. With these uncertainties, the fit code returns an uncertainty estimate for each parameter in the model. For each detector pair i, and each of the consistency tests j, we then have an array E_{ij} of uncertainties on the polarization angle offsets from nominal. We assign a weight to each polarization angle fit,

$$w_{ij} = \frac{1}{E_{ij}^2}. \tag{4.26}$$

Table 4.1: Description of what was changed in each of the consistency tests and the weighted means of the data points in Figure 4.15. Any changing systematic errors between the tests should show a shift in the mean. Test 8 shows the largest shift among the tests at 0.°08. With the exception of test 3, the aspect changed is compared with test 1, not the previous test.

Test	Weighted Mean (Deg)	Aspect Changed
1	0.000006	initial measurement
2	0.003	remove and reinstall calibrator
3	0.01	no changes from 2
4	−0.04	rotate baffle 80° w.r.t. encoder tape
5	0.008	baffle back in same position as test 1, telescope rotated 20° in deck
6	−0.01	base stage disassembled and reassembled, encoder tape remounted
7	0.02	telescope rotated +90° in Azimuth
8	0.08	dielectric sheet replaced

The first consistency test ($j = 1$) contained the least noisy timestreams, which resulted in the smallest uncertainties and the largest weights on the polarization angle fits. In the median across detector pairs, test 1 has three times the weight of any other test. Tests 7 and 8 have the smallest weights at 20 and 14% (respectively) the weight of test 1. The low weights are the result of an unfortunate increase in detector noise in the later tests.

4.6.1 Checking the Consistency

Before combining polarization angle fits across the 8 consistency tests into a final result, we first check their compatibility. We calculate the weighted means of the fits for each detector pair across the consistency tests with

$$\bar{\psi}_i = \frac{\sum_j \left(\psi_{ij} w_{ij}\right)}{\sum_j w_{ij}}, \tag{4.27}$$

where ψ is the polarization angle fit. Figure 4.15 shows the difference between ψ_{ij} and $\bar{\psi}_i$ for the j consistency tests. Each detector pair is compared to its weighted mean because we only want to show overall offsets between the consistency tests. If we instead plotted the ψ_{ij}, any real pattern between the detectors would make the plots harder to interpret. We also calculate the weighted mean, $\mathcal{M}$, across pairs for each consistency test j:

$$\mathcal{M}_j = \frac{\sum_i \left(\psi_{ij} - \bar{\psi}_i\right) w_{ij}}{\sum_i w_{ij}}. \tag{4.28}$$

This produces a single number for each consistency test which is listed in Table 4.1 in the "Weighted Mean" column and shown in each panel of Figure 4.15 with a solid red line. The weighted mean shifts range between $-0.^{\circ}05$ and $+0.^{\circ}08$, and the largest shift occurred in test 8 when the dielectric sheet was replaced. From these consistency tests, we estimate a systematic uncertainty of $0.^{\circ}1$ in our polarization calibration measurements.

From the investigation above, we determine that the consistency of the data is sufficient to combine over the eight tests, and we combine the measurements with Equation (4.27). The results are shown in Figure 4.16. There is a clear tile-dependent effect in the polarization angle offsets. Tiles 1 and 3 appear consistent with an overall rotation, but tiles 2 and 4 show a slight gradient from top to bottom as plotted at the bottom of the figure, which produces a general slope across detector pair number, as shown at the top of the figure. These tile-wise gradients are inconsistent with any of the uncertainties investigated in Section 4.5, so we interpret the effect as real. Calculation of the error bars is explained in the next sub-section.

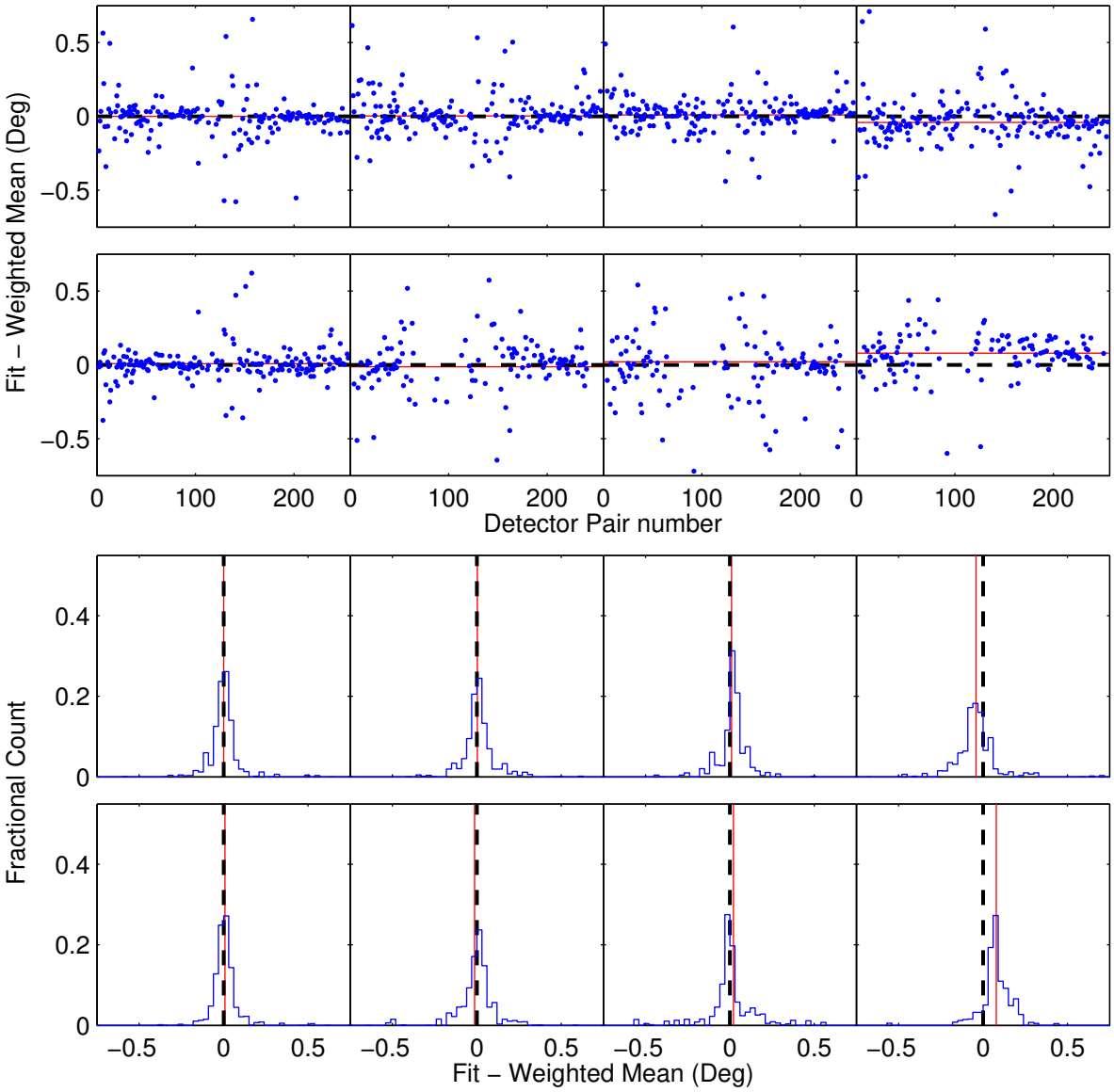

Figure 4.15: *Top*: The difference of the measured polarization angle offset for all eight consistency tests to the weighted mean over the eight consistency test, ordered 1 to 4 from left to right on the top set of panels and 5 to 8 on the bottom set. A dashed black line is drawn at 0°, and a red solid line is drawn at the weighted mean of the points. *Bottom*: Weighted histograms of the points in the scatter plots. The panels are arranged in the same order as the plots on top. Test 8 shows a small shift of 0.°08, providing possible evidence of a small systematic effect in that test.

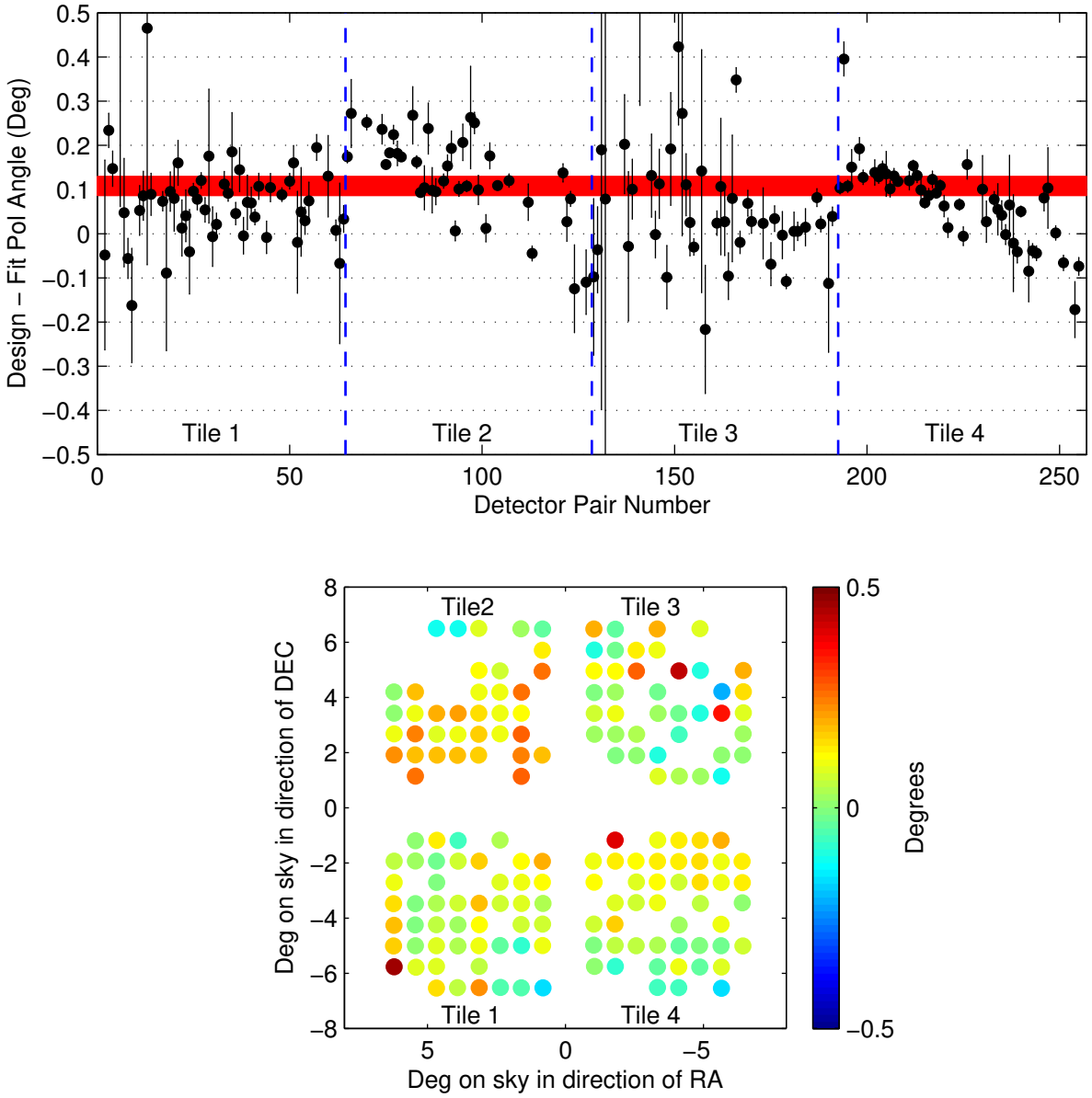

Figure 4.16: *Top*: The difference between the design and fit polarization angles plotted against pair number. The points are the weighted mean of the fit values over the consistency tests, and the error bars are the uncertainties on the weighted mean. The underlying red region is centered on the weighted mean of the points, and the width is a conservative estimate of the uncertainty on the weighted mean. *Bottom*: The same data plotted as a function of sky location with respect to the telescope boresight.

4.6.2 Calculating the Weighted Variance

In Chapter 5, we'll show that the mean polarization rotation angle has a much more significant impact on our B-mode measurements than the pattern across the focal plane. Before calculating the average rotation angle across detector pairs, we estimate an uncertainty on each $\bar{\psi}_i$. For the i detector pairs, we calculate the weighted variance V with a bias correction, but we first rescale the weights for each pair so that they sum to one:

$$w'_{ij} = \frac{w_{ij}}{\sum_j w_{ij}}. \tag{4.29}$$

We then use

$$V_i = \frac{\sum_j \left(\psi_{ij} - \bar{\psi}_i\right)^2 w'_{ij}}{1 - f_i}, \tag{4.30}$$

where $f_i = \sum_j w'^2_{ij}$ and is used as the effective number of measurements. We then estimate the uncertainty on each $\bar{\psi}_i$ as

$$\mathcal{E}_i = \sqrt{\frac{V_i}{f_i}}, \tag{4.31}$$

which we call the weighted standard deviation. The $\mathcal{E}_i$ are the values used for the error bars in Figure 4.16, and Figure 4.17 shows $\mathcal{E}_i$ for each detector pair.

We now estimate the average polarization rotation angle, $-\Delta\alpha$ as the weighted mean of the $\bar{\psi}_i$ over the detector pairs. The calculation is similar to Equation (4.27):

$$-\Delta\alpha = \frac{\sum_i \bar{\psi}_i \frac{1}{\mathcal{E}_i^2}}{\sum_i \frac{1}{\mathcal{E}_i^2}}. \tag{4.32}$$

The negative sign is placed in front of $\Delta\alpha$ is a result of our definition of polarization angles. If $-\Delta\alpha$ is not subtracted from our detector's polarization angles, then we expect that the underlying CMB polarization power spectra will be rotated by $+\Delta\alpha$ as in Equations (1.22) to (1.26). The uncertainty on $-\Delta\alpha$ is calculated with Equations (4.30) and (4.31) by substituting ψ_{ij}, $\bar{\psi}_i$, and w_{ij} with $\bar{\psi}_i$, $-\Delta\alpha$, and $\frac{1}{\mathcal{E}_i^2}$, respectively. This is not necessarily the correct thing to do. If the $\bar{\psi}_i$ were assumed to be drawn from the same mean, we would calculate a more aggressive uncertainty. However, we need some value, so we chose this more conservative estimate and obtain the results; $-\Delta\alpha = 0.11 \pm 0.03$ degrees.

4.7 Discussion

The eight consistency tests appear to produce polarization angle fits that are consistent (over the tests) to within $\sim 0.^{\circ}1$. This does not, however, eliminate the possibility of a larger systematic. In Section 4.5, we saw that the angle ϕ is the most important angle to know correctly. We've aimed to minimize this uncertainty by taking multiple measurements with the protractor in two opposing orientations and by calibrating the protractor often. The consistency of the eight tests verifies that the statistical uncertainty of the protractor measurements is small. The tests also offer some evidence that the systematic uncertainty is small since we would expect that the systematic could change each time the protractor is calibrated.

We are also concerned that there may be a systematic offset in our absolute polarization angle measurements since we haven't measured the angle γ, the rotation of the dielectric sheet about its major axis. We have instead assumed the design value $\gamma = 0°$. From machining tolerances, we might expect the dielectric sheet to be twisted such that one edge of the sheet is at most 3 mm higher than the design position and the other edge is 3 mm lower. With

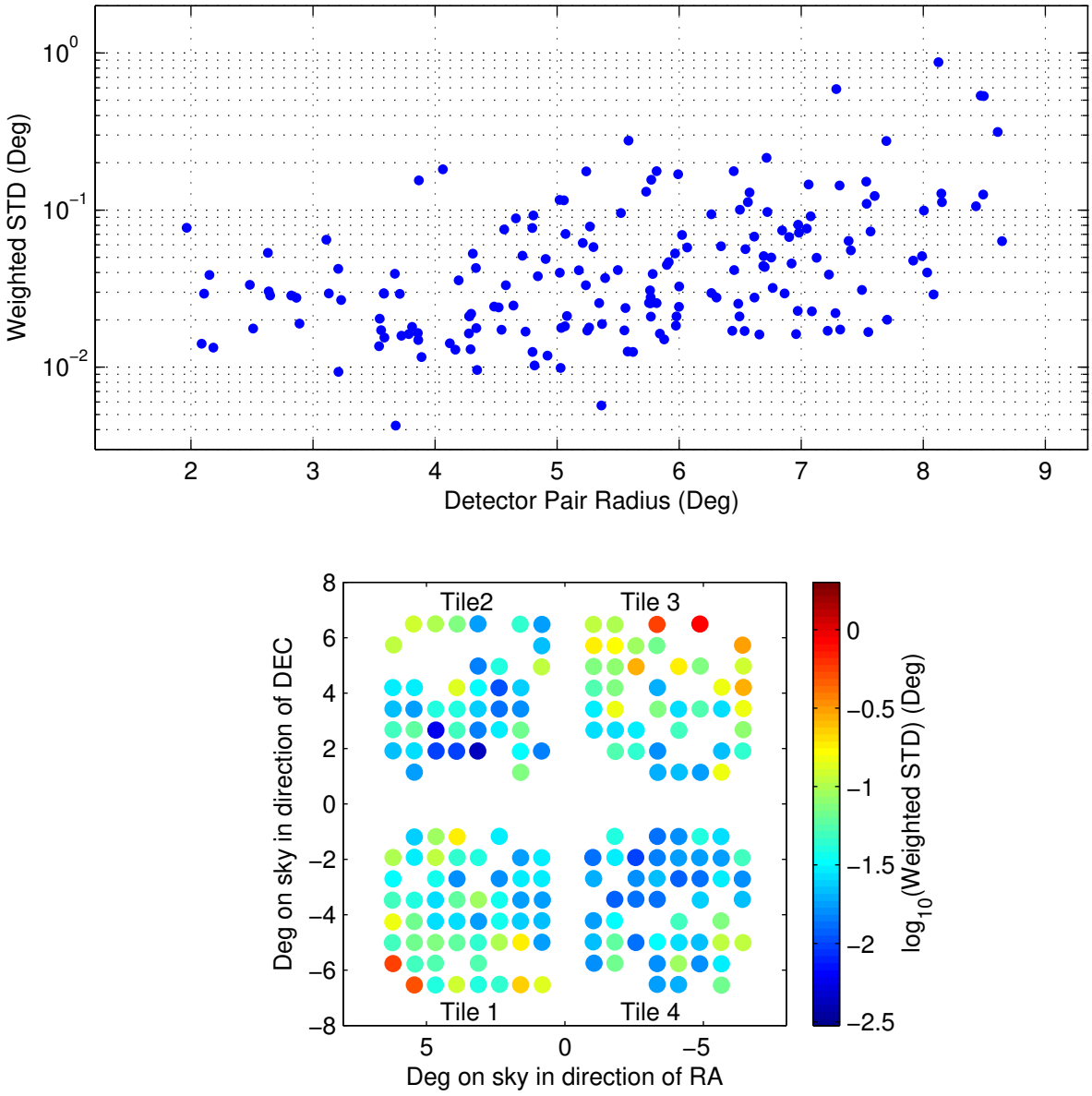

Figure 4.17: *Top*: Uncertainty estimate of $\bar{\psi}_i$, the weighted mean polarization angle fits, as a function of detector pair radius from the telescope boresight. *Bottom*: The same data plotted as a function of sky location with respect to the telescope boresight. In both plots, we see evidence for increased standard deviations among the measurements for pairs at large radii from the boresight.

a minor axis length of $\sim$610 mm, the true value of γ would be $\pm 0.^{\circ}6$. Our use of $\gamma = 0^{\circ}$ would then introduce a systematic shift of $\pm 0.^{\circ}1$. If we are instead very conservative and allow an angle rotation of $\sim$1 cm, then $\gamma = 2^{\circ}$, and we introduce a systematic shift of $\pm 0.^{\circ}3$ by using $\gamma = 0^{\circ}$. This systematic is not inherent to the DSC calibrator; it's a result of assuming the design value of γ. Using the estimate of the systematic from the consistency tests and the realistic upper limit on the systematic that comes from not measuring γ, we put a conservative upper limit on the total systematic in our polarization angle calibrations of $\pm 0.^{\circ}2$. Combined with our stated statistical uncertainty of $\pm 0.^{\circ}03$, we meet our minimum goal of measuring the global polarization rotation to better than $\pm 0.^{\circ}5$.

In Section 3.7, we discussed the process of fitting the TB and EB angular power spectra to determine an angle by which the polarization fields are rotated. We concluded that the rotation in our data is consistent with a systematic shift in our detectors' polarization angles. To undo the rotation, we rotate our Q and U maps by $2\Delta\alpha$. In Table 3.5, we included the angle necessary to minimize the TB and EB spectra in the $\mathrm{K2015}_{150}$ data, which is data from a single receiver for the 2015 observing season. Around two months after that observing season ended, we performed the DSC measurements on the same receiver. From self-calibration of the $K2015_{150}$ data, we found $\Delta\alpha = -0.^{\circ}03 \pm 0.^{\circ}33$. With the DSC data, we found $-\Delta\alpha = 0.^{\circ}11 \pm 0.^{\circ}03$ ($\pm 0.^{\circ}2$ syst). Under the no cosmic birefringence hypothesis, there is no conflict between these two methods of determining the average absolute polarization angles of our detectors. This is in contrast with the BICEP2 results,[12]

[12] In the BICEP2 model, γ was defined as a lateral tilt (a rotation about the y-axis after applying the tilt rotation matrix) of the dielectric sheet, which differs from our definition in this dissertation as a rotation about the sheet's major axis. Therefore, the order of multiplying the rotation matrices was $R_t R_\gamma R_\phi$ in BICEP2 instead of that presented in Equation (4.2). After slewing the telescope in elevation to make $\hat{\mathbf{M}}$ close to horizontal, γ was measured with a digital protractor aligned with $\hat{\mathbf{m}}$. We believe the BICEP2 DSC results did not take into account the fact that the protractor measures angles with respect to gravity (see Equation (4.7)) and was therefore not directly measuring the angle γ in the model. We believe this might account for half of the discrepancy between the DSC- and CMB-derived angles.

where self-calibration of the BICEP2 data resulted in[13] $\Delta\alpha = -0.^{\circ}9 \pm 0.^{\circ}17$ and the DSC results were $-\Delta\alpha = -0.^{\circ}2 \pm 0.^{\circ}04$ [74].

Although the estimated systematic uncertainty in our DSC measurements meet our goals for measuring the absolute polarization angles of our detectors, there are improvements which could be made. Currently, at least half[14] of our systematic uncertainty results from not measuring the angle γ in our model. Possibilities for measuring γ include the use of a 3-D mechanical measuring arm and/or photogrammetry.

Another area for improvement is in understanding and/or eliminating the source of excess signal in the per-detector DSC signal. In either case, we should then be able to fit the polarization angles of individual detectors instead of pairs. One theory for the excess signal is that the aluminum ring that holds the dielectric sheet enters and exits the detector beams or their sidelobes as the calibrator rotates. We can add the same microwave absorbing material that lines the baffle to the aluminum ring. Doing so won't eliminate the excess signal, but it might make it predictable. If the ring is the problem, a better solution would be to increase the major and minor axes of the ring, which requires a larger diameter baffle, and/or decrease the tilt angle, t.

[13]The value $-0.^{\circ}9$ is the difference of $\Delta\alpha$ from the global rotation fit ($-1.^{\circ}1$) and $-\Delta\alpha$ from the DSC results ($-0.^{\circ}2$) since the polarization angles used in the BICEP2 data analysis used the DSC results.

[14]We say at least half because it's possible γ changed in test 8, which could be part of the reason for the discrepancy.

Chapter 5

IMPACT OF POLARIZATION ANGLE UNCERTAINTY

5.1 Simulating Polarization Angle Uncertainties

Although we'd like to precisely know the polarization angles of our detectors as projected on the sky, we accept that there is some uncertainty. This uncertainty has the potential to rotate measurements of the real-sky Q and U patterns, which leaks E-modes into B-modes.[1] In this chapter, we investigate the impact of polarization angle systematics on measuring B-modes.

The uncertainty on our polarization angles can be broken down into three classes: (i) all of the polarization angles are rotated by the same amount, (ii) the polarization angles are rotated randomly with some level of rms, (iii) the polarization angles are rotated in some pattern. An example of the third class is the angles measured with the DSC, covered in

[1] It also leaks B-modes to E-modes. However, the B-mode signal is much weaker, so this leakage is less important.

Chapter 4 and shown in Figure 4.16. However, the DSC measurements may also contain contributions from the first two classes.

Table 5.1 lists all of the polarization angle "dither" simulations that are presented in this dissertation, including a column noting how they are labeled in figures and referred to in this chapter. For each type, 49 realizations are simulated using the telescope configuration and data from the 2014 observing season for the *Keck Array*. These simulations are based on the unlensed-ΛCDM model, meaning they contain zero B-modes. It's important that the inputs to the simulations are free of B-modes so that we can attribute any calculated B-modes[2] to the polarization angle uncertainties. The first simulation type in the list,"5.00rot," rotates all polarization angles by 5° and falls into class (i). We choose to simulate this large rotation to make the effect prominent in this baseline case. The next four types of simulations in the table, "0.14rms," "1.00rms," "5.00rms," and "10.00rms," fall into class (ii). Because our scan strategy ensures most map pixels are observed by many detectors, we expect Gaussian random polarization angle systematics to average down. The 1°, 5°, and 10° rms simulations investigate how effective this averaging is. The 0.̊14 rms is chosen since it is the standard deviation over one of the 150 GHz focal planes as measured with the DSC (see Chapter 4). In all of these "rms" simulations, a new draw is made for each realization, and the mean of the Gaussian is 0°. The last two simulation types, "DSC" and "5×DSC," fall into class (iii) and are based on the measured polarization angles from the DSC analysis (see Figure 4.16). In these two simulations, we subtract the mean angle to isolate the pattern of polarization angle deviations across the focal plane. To exacerbate any effect of the pattern, the offsets in the "DSC" simulations are multiplied by a factor of five to create the "5×DSC" simulations. Since we only had reliable measurements with the DSC on one of the 150 GHz receivers, we

[2] in excess of a fiducial set of simulations that contain no B-modes and no polarization angle uncertainties

treat the angle differences as representative and apply them to all of the 150 GHz receivers. Because the 95 GHz focal planes have larger detector spacings and lower detector counts than the 150 GHz focal planes, we did not simulate any polarization angle offsets for the 95 GHz receivers in these last two simulation types. Another caveat is that some detectors in the 150 GHz receiver were not well measured with the DSC. Rather than discard the simulated data from these detectors, we set them to the mean of the nearby detectors in an effort to maintain any patterns across the focal plane. The offsets used in the "DSC" set of simulations is shown in Figure 5.1. The points in this figure came from an earlier analysis of DSC data than that presented in Chapter 4. In addition to the interpolated points and mean subtraction, there are differences between the angle dithers used in the "DSC" simulations and the points in Figure 4.16, but the general pattern across the focal plane is very similar.

Table 5.1: List of the polarization rotation simulations presented in this dissertation. For all cases, input maps based on the unlensed-ΛCDM model were used. The column titled "Label," indicates how each simulation type is typically referenced in this document.

Label	Magnitude and Type of Simulated Rotation
5.00rot	5.00° shift to all
0.14rms	0.14° rms shift
1.00rms	1.00° rms shift
5.00rms	5.00° rms shift
10.00rms	10.00° rms shift
DSC	DSC results
5×DSC	5 times the DSC results

5.2 Angular Power Spectra

For each simulation realization, we calculate the APS in the same way as described in Section 3.6. Figure 5.2 shows the BB, TB, and EB spectra for three of the simulation types,

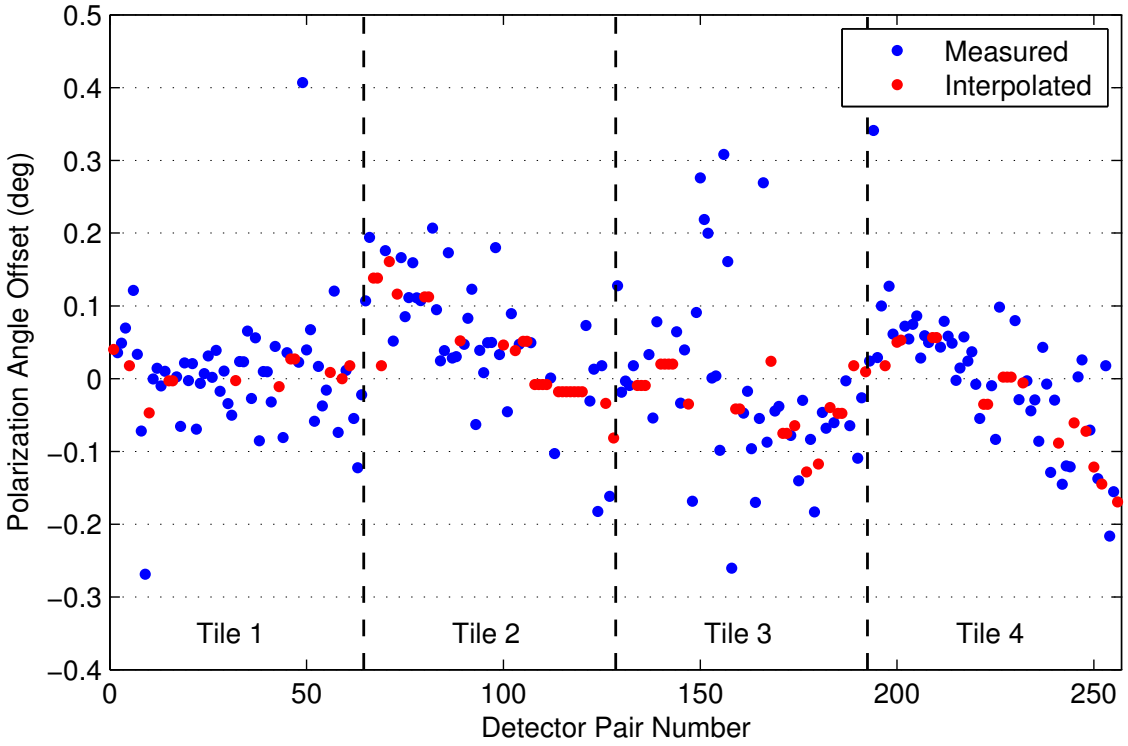

Figure 5.1: Measured values added to the nominal polarization angles to make the "DSC" simulations. Multiplying these values by five gives the values added in the "5×DSC" simulations. The blue points are based off the DSC-measured angles from an earlier but similar version of Figure 4.16 but with the mean offset subtracted. Detectors with poorly measured polarization angles are set to the mean of the surrounding well-measured detectors, and they are plotted with red points. The red points follow the general tile-dependent shape of the blue points.

and Figure 5.3 shows the TB and EB spectra for the "5.00rot" case with a larger vertical range. The error bars represent the standard deviations across the 49 realizations for each band power, and the points are plotted at the mean. We also include the standard set of unlensed-ΛCDM simulations where no polarization angle offsets were simulated, giving it the label "None." This sets the minimum expected threshold from using a purification matrix that was calculated for multi-year data with these single-year simulations. For the BB panels, we include an $r = 0.05$ model that does not include lensing contributions. We also include the model lines in the TB and EB panels, which are identically zero at all multipoles. As expected, the "5.00rot" simulations show a large excess of power above the model expectation. The simulations from the DSC results are consistent with the "None" case. Even the "10.00rms" simulations show little effect in BB above the "None" case. In the mean, there is also little effect in TB and EB. This confirms the claim from Chapter 4 that an overall rotation of polarization angles is more important to the measurement of B-modes than a pattern across the focal plane. Though they are not shown here, we compared the spectra for all simulation types. The "5.00rms" spectra are about halfway between the "None" and "10.00rms" spectra. The spectra for the rest of the simulation types in Table 5.1 are almost indistinguishable from the "None" spectra on the scale of these plots.

5.2.1 Fitting for Global Rotation

For each simulation realization, we now find the rotation angle which minimizes the EB signal for that realization using the same procedure we currently perform in the standard analysis of the real CMB data (see Section 3.7 for discussion of this procedure). Histograms of the resulting global rotation angles for all of the simulation types in Table 5.1 are shown in Figures 5.4 and 5.5 for 95 GHz and 150 GHz, respectively. For comparison, we include a

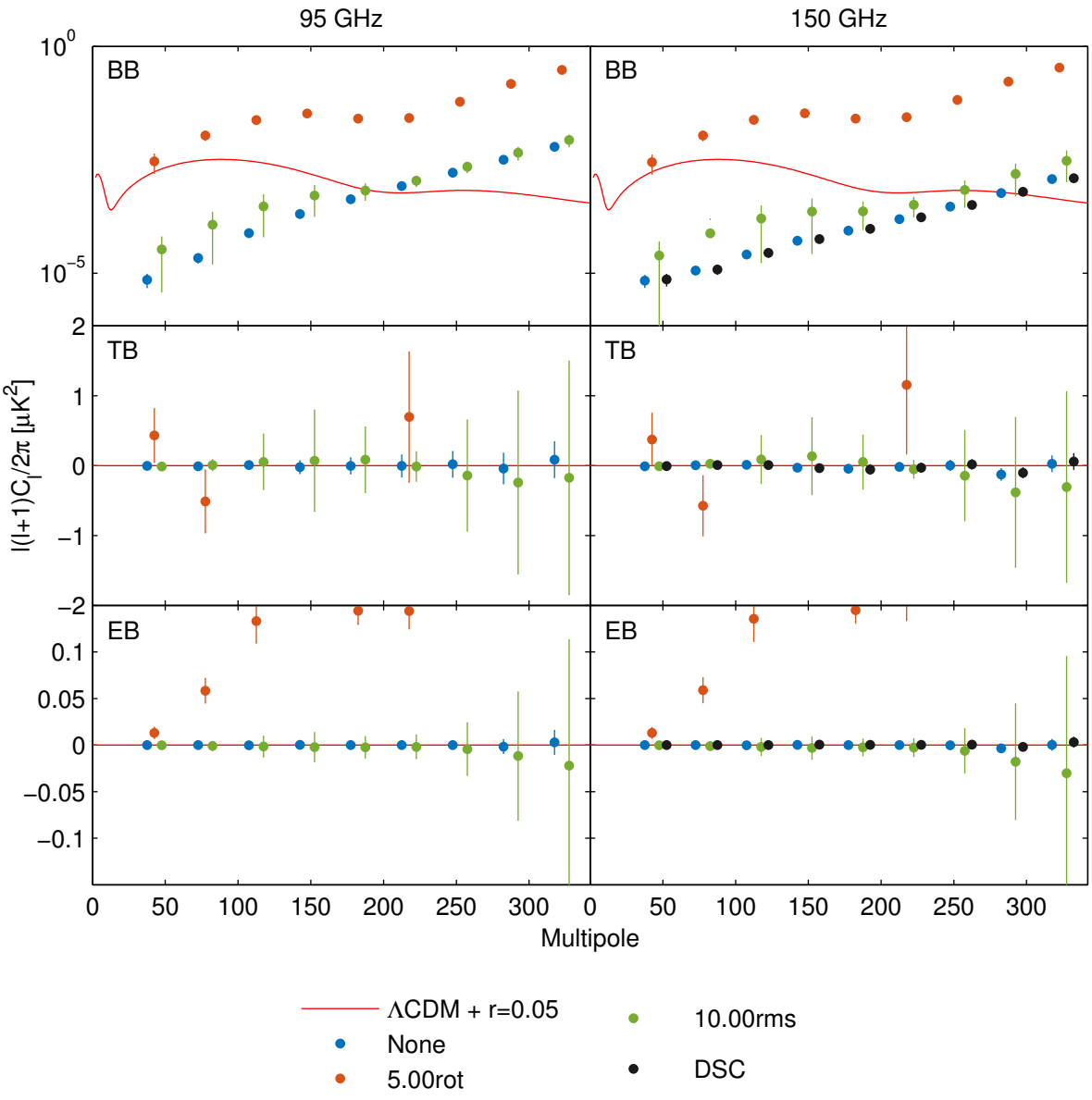

Figure 5.2: First nine band powers of the angular power spectra for three of the polarization rotation angle simulations listed in Table 5.1 and our standard simulations (labeled as "None"). The red lines are the expectation values for an unlensed-ΛCDM + $r = 0.05$ model. The sizes of the error bars indicate the standard deviations at each band power over the realizations. The "5.00rot" simulations have introduced a large level of leakage, as expected, and the TB and EB spectra are replotted in Figure 5.3

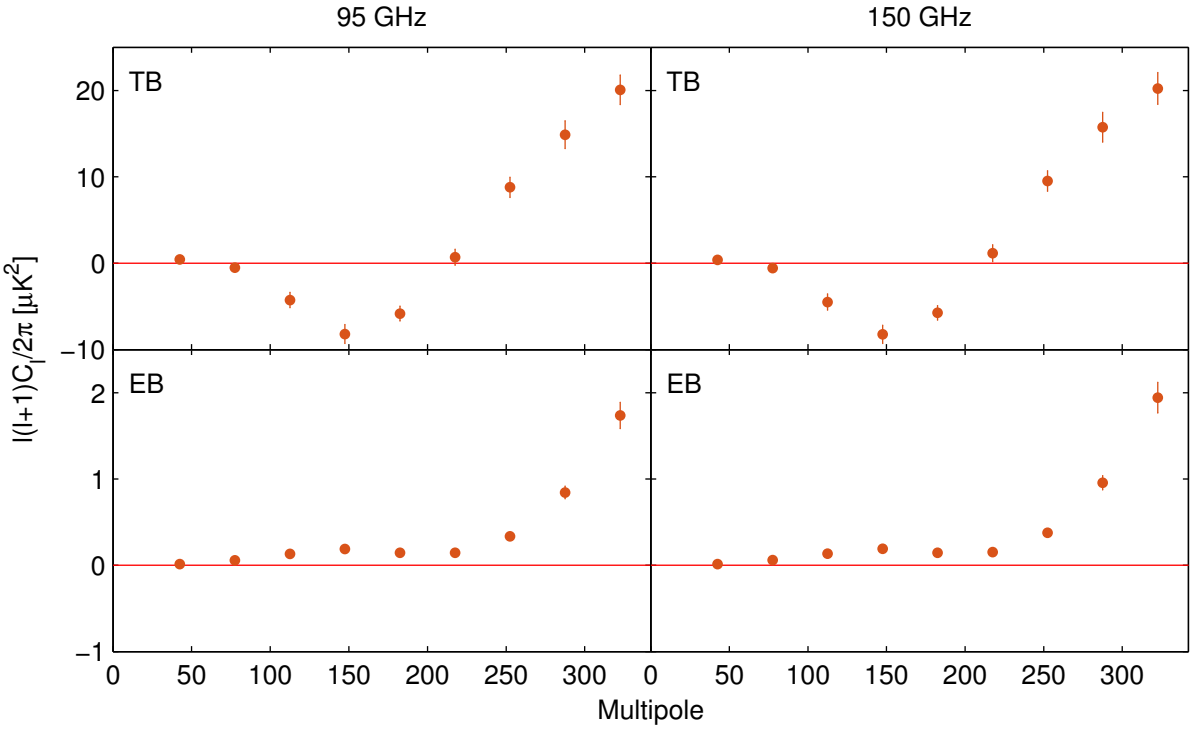

Figure 5.3: Angular power spectra of the "5.00rot" polarization angle rotation simulations. This shows the same data for this simulation as Figure 5.2 but with larger ranges on the vertical axis in order to show the full shape of the spectra.

histogram of the best fit rotation angles of the first 49 realizations of the standard analysis[3] ("None"), but we don't rotate the standard simulated maps. The mean rotation angle for "5.00rot" is 4.9° for both 150 and 95 GHz. The "10.00rms" has a mean rotation angle of $\sim 10^{-3}$ degrees and a standard deviation of ~ 0.1 degrees.

We rotate each simulated map by the best fit global rotation angle and recalculate the APS. Figure 5.6 shows the resulting power spectra for each simulation type. There's a large improvement to the level of false BB power for the "5.00rot" simulations, and the TB and EB spectra now fit on the same axes as the other simulation types. Also, the fluctuation decreases for the band powers of the "10.00rms" simulations.

5.2.2 Iterating the Fit

Although there is large improvement in the amount of false BB power in the "5.00rot" simulations after rotating the maps by the best fit global rotation angles, there is still excess power above the other simulation types. This is not surprising since a five-degree rotation was simulated but the mean (among the 49 realizations) best fit global rotation is $\sim 4.9°$. To test if there is a breakdown in the assumptions made in the global rotation fitting code, we rotated each of the simulation realizations by exactly 5° and calculated their APS. This resulted in identical spectra to the same realizations of the standard unlensed-ΛCDM simulations (labeled "None" in the figures). We therefore perform an iterative global rotation fit as described in the following list:

[3] We restrict the histograms to the first 49 realizations because the set of input maps is then identical to the rest of the simulation types.

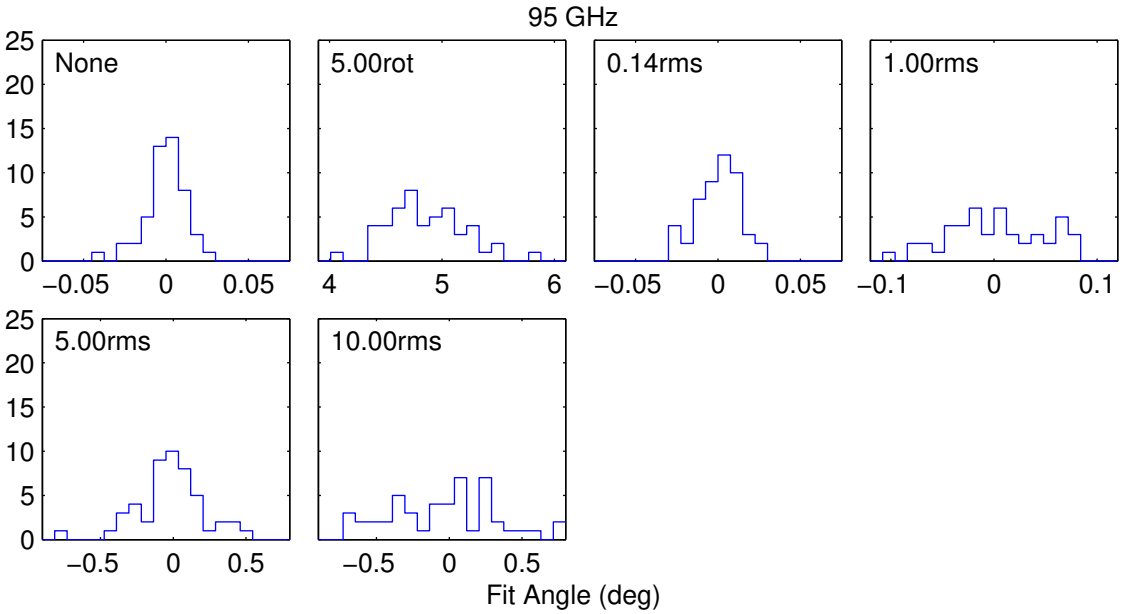

Figure 5.4: Histograms of the global rotation fit values for all simulations types listed in Table 5.1 for 95 GHz, as well as the first 49 realizations of our standard analysis simulations that have no simulated polarization angle offsets. Note that there are four different ranges used in these histograms, but the number of bins is unchanged. Also, there were no simulations made with DSC-derived polarization angles for the 95 GHz receivers, so those simulation types are not shown.

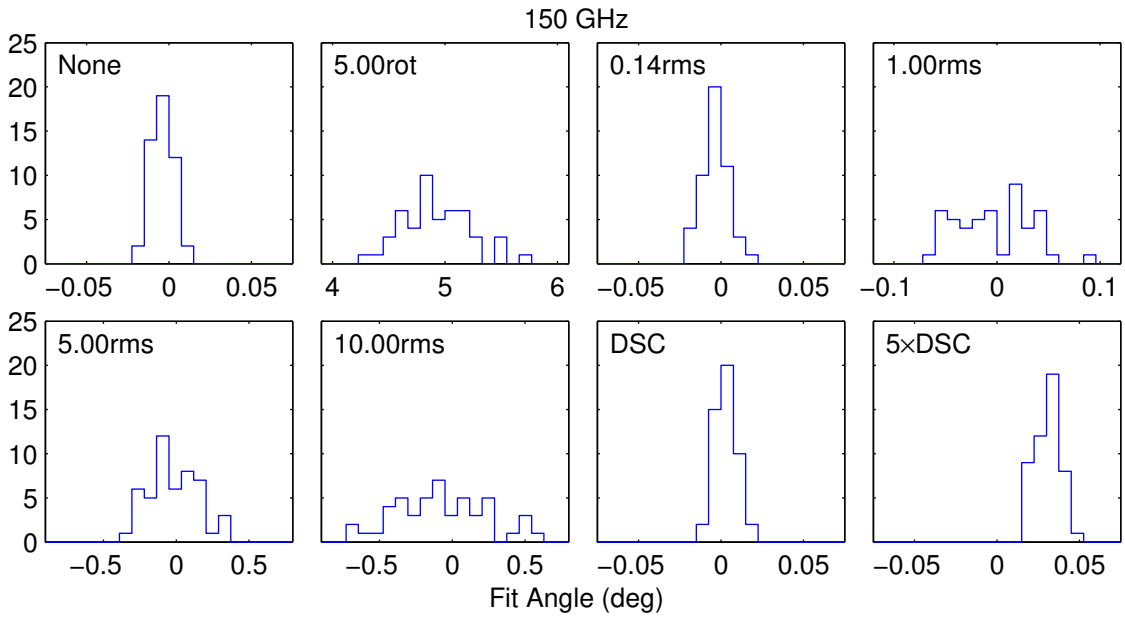

Figure 5.5: Histograms of the global rotation fit values for all simulations types listed in Table 5.1 for 150 GHz, as well as the first 49 realizations of our standard analysis simulations that have no simulated polarization angle offsets. Note that there are four different ranges used in these histograms, but the number of bins is unchanged.

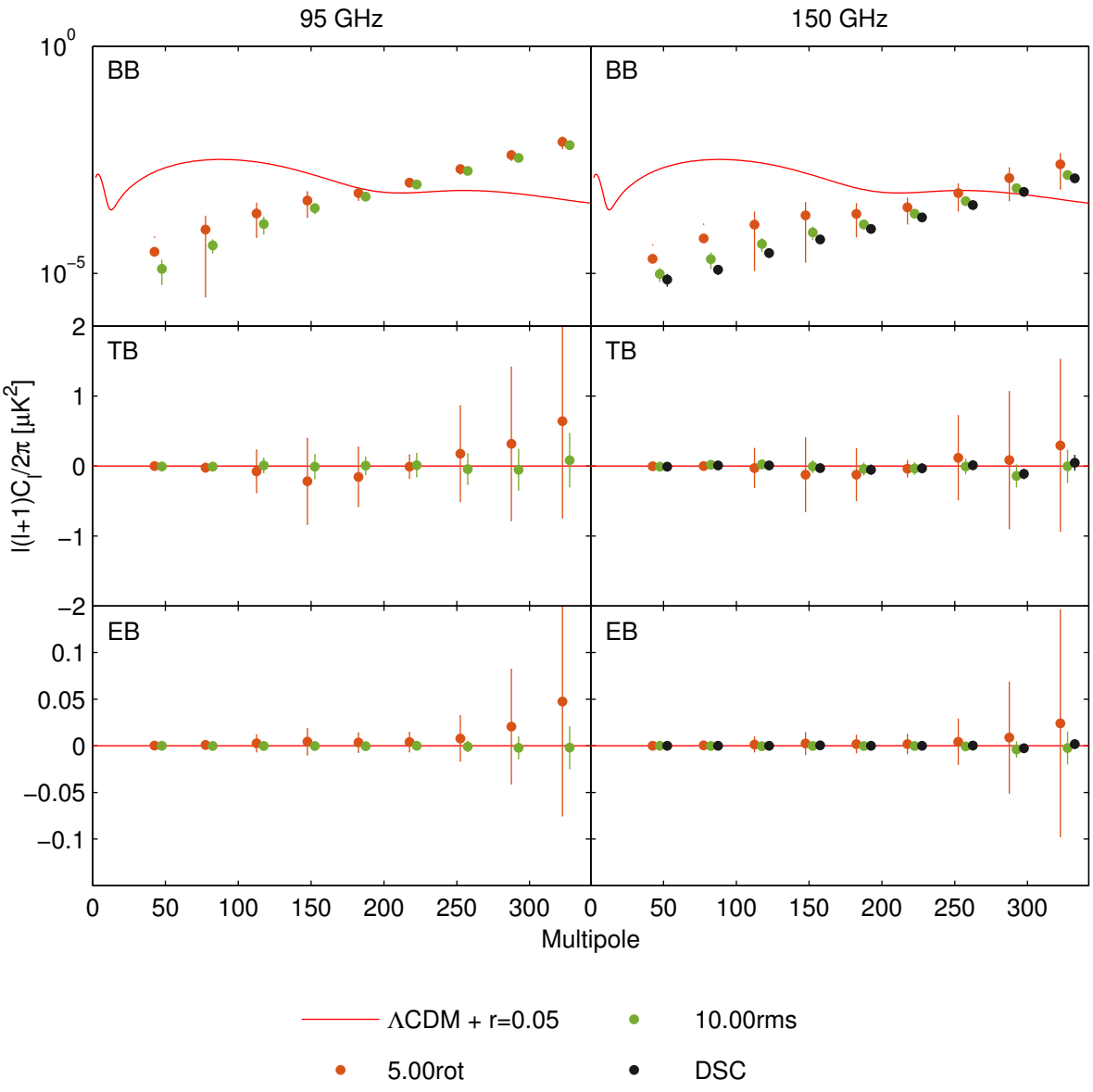

Figure 5.6: Angular power spectra for three of the polarization angle rotation simulations in Table 5.1 after the maps are rotated by the global rotation fit angles. This figure shows the effectiveness of the global fit rotation procedure in reducing the overall EE/BB leakage and the standard deviation across the realizations of each simulation.

1. Calculate the APS for each simulated map (APS were shown in Figures 5.2 and 5.3).

2. Minimize the EB spectrum to obtain a global rotation angle on a realization-by-realization basis (angles were shown in Figures 5.4 and 5.5).

3. Rotate the simulated Q and U map by the best fit rotation angle found in step 2 and recalculate the APS (was shown in Figure 5.6).

4. Obtain a new set of global rotation angles on these new APS.

5. Use the sum of all previously calculated rotation angles to rotate each simulated map and recalculate the APS.

We can repeat steps 4 and 5 until additional iterations change the accumulated rotation angle by less than the uncertainty. We call steps 2 and 3 iteration 1. The first cycle through steps 4 and 5 is iteration 2, and each additional cycle is another iteration.

For the real data, the initial rotation angles are typically less than 1°, and the uncertainties are a few tenths of a degree. We therefore aren't yet motivated to implement iteration on the global angle rotation fitting procedure applied to the real data. However, since the simulations presented in this chapter are noiseless, we test the iteration procedure on them. Figure 5.7 shows the progression of the cumulative rotation angles for the "5.00rot" simulations as the fitting procedure is iterated. Figure 5.8 shows the spectra after the second iteration, meaning the initial simulated maps are rotated by the sum of two separate best fit rotation angles. This is one iteration beyond what was shown in Figure 5.6. The spectra of the "5.00rot" simulations agree much better with the other simulation types, and the error bars, indicating the STD of the band powers across the 49 realizations, are also of comparable size to the other simulation types. This is not surprising since the distribution of applied rotation angles, shown under "Iteration 2" in Figure 5.7 is close to the simulated five-degree rotation.

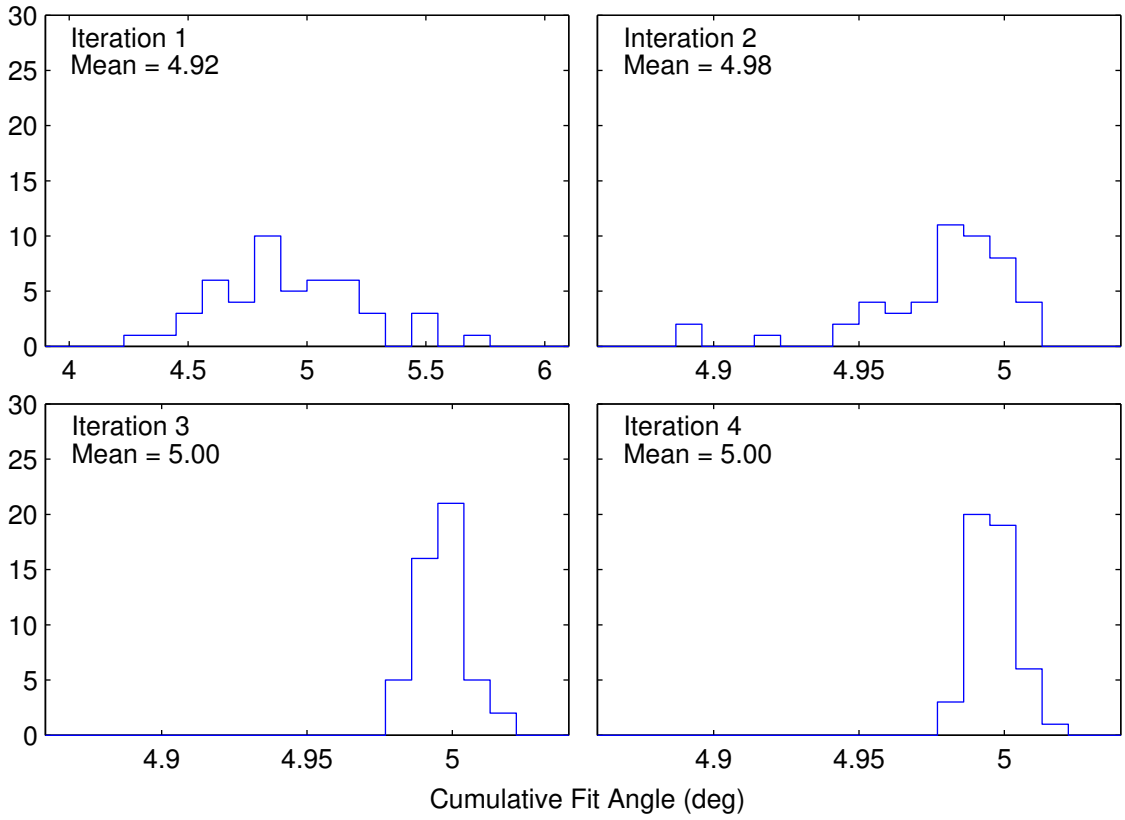

Figure 5.7: Histograms of the global rotation fit angles for each of the 49 realizations of the "5.00rot" simulations. The Iteration 1 plot contains the angles based on APS calculated from the simulated maps. The Iteration 2-4 plots are the cumulative fit angles after rotating the same simulated maps by the previous iteration's cumulative angles. We did not use the angles in Iteration 4 to make another set of APS since the change from Iteration 3 is marginal. Note also that the Iteration 1 plot has a larger horizontal range than the rest.

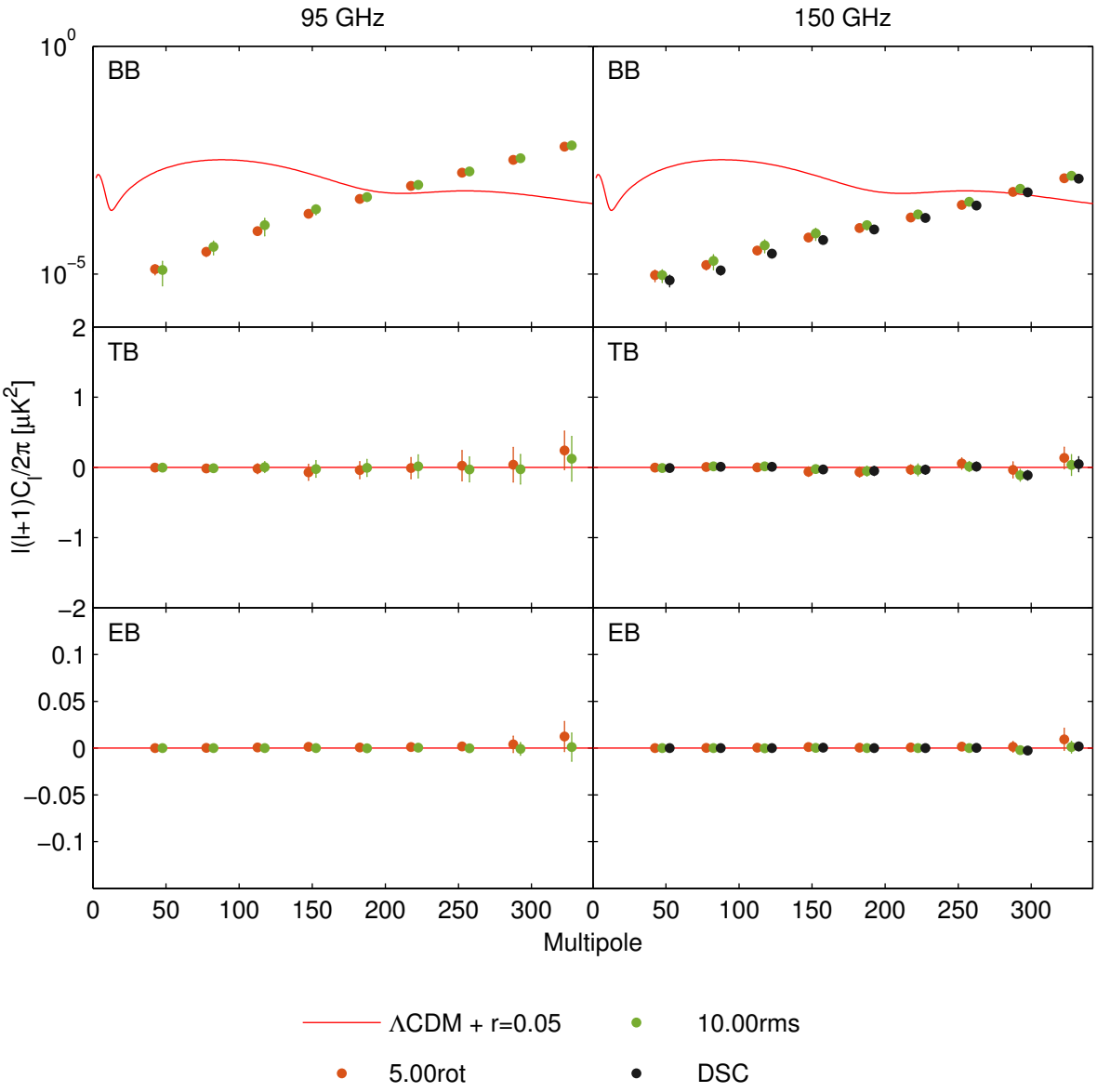

Figure 5.8: Angular power spectra for the polarization angle rotation simulations after the maps are rotated by the cumulative global rotation fit angles from the first two iterations as described in the text. The angles used in rotating the "5.00rot" simulated maps are shown in Figure 5.7 in the panel titled "Iteration 2." Iteration 3 rotation angle fits are then calculated from these EB spectra.

5.3 Bias on Tensor-to-Scalar Ratio

For each of the simulations, we estimate the level of false B-modes, which we call the ρ parameter. We first calculate the APS in the usual manner. For each band power of the APS, we calculate a weight as

$$w_n = \frac{R_n}{N_n^2}, \tag{5.1}$$

where R_n is the mean of the n^{th} BB band power over an ensemble of noiseless unlensed-ΛCDM $+ r = 0.1$ simulations,[4] and N_n is the standard deviation of the same band powers. Note that the simulations used in the ρ estimation contain B-modes, unlike the simulations presented in the previous sections of this chapter. This is necessary to account for the cosmic and sample variances. Using only the first five band powers, we calculate the following two quantities:

$$S_R = \frac{\sum_{n=1}^{5} R_n w_n}{\sum_{n=1}^{5} w_n} \tag{5.2}$$

$$S_C = \frac{\sum_{n=1}^{5} B_n w_n}{\sum_{n=1}^{5} w_n}, \tag{5.3}$$

$$\tag{5.4}$$

where the B_n are the differences of the BB band powers between the polarization rotation simulations and our standard simulations. By taking the difference, we make an estimate of the bias on r that is due only to a polarization angle systematic. That estimate is

$$\rho = 0.1 \frac{S_C}{S_R}, \tag{5.5}$$

[4] The choice of the value of r will be accounted for in a later step.

where the factor of 0.1 arises because that is the value of r contained in the standard simulations.

For each of the simulation realizations we calculate ρ, and the mean values over the 49 realizations for each simulation type are listed in Table 5.2. The mean bias values are shown for Iterations 0–3, where the Iteration 0 values are calculated on the initial APS of the simulations, meaning the simulated Q and U maps weren't rotated. If we allow random rotations with $0.^{\circ}14$ rms, there is very little bias on our B-mode measurement. If instead the polarization angle offsets have a pattern (with the mean subtracted) across the focal plane as measured with the DSC (see Figure 5.1), the bias is only a factor of two higher. Even if the real pattern were five times stronger than the DSC measurements indicate, the bias on r is only 4×10^{-5}. However, a 5-degree global rotation of the polarization angles would bias r by 0.3. The bias on B-modes is a quadratic function of the rotation angle, so we can estimate that a 1-degree global rotation would bias r by 0.01. From these values of ρ, we reaffirm the impression from Figures 5.2 and 5.3; uniform instrumental polarization rotations are more import to know than random or patterned (both with 0° mean) offsets, at least with the BICEP/*Keck* scanning strategy.

Table 5.2: Biases on the tensor to scalar ratio from each of the polarization rotation simulations listed in Table 5.1 for the 150 GHz band. These are the mean values over the 49 simulation realizations. The biggest improvement in this list occurs between Iteration 0 and Iteration 1 for the "5.00rot" simulation, where a five-degree global rotation was simulated. For the other simulation types, only the "10.00rms" simulation show a problem in the iteration 0 column when compared to our future sensitivity goals. However, a 10-degree rms is extremely unlikely in a real focal plane. Iteration 0 means the APS used in the ρ parameter calculation were not rotated. The rest of the iterations are explained in Section 5.2.2.

Label	Iteration 0	Iteration 1	Iteration 2	Iteration 3
5.00rot	3×10^{-1}	1×10^{-3}	8×10^{-5}	7×10^{-5}
0.14rms	2×10^{-6}	2×10^{-6}	2×10^{-6}	2×10^{-6}
1.00rms	2×10^{-5}	6×10^{-6}	6×10^{-6}	6×10^{-6}
5.00rms	4×10^{-4}	6×10^{-5}	6×10^{-5}	6×10^{-5}
10.00rms	2×10^{-3}	2×10^{-4}	2×10^{-4}	2×10^{-4}
DSC	4×10^{-6}	4×10^{-6}	4×10^{-6}	4×10^{-6}
5×DSC	4×10^{-5}	3×10^{-5}	3×10^{-5}	3×10^{-5}

Chapter 6

Keck 2015

To determine whether a B-mode signal is cosmological in origin or due to foregrounds, it is necessary to take measurements at multiple frequencies. In CMB temperature units, a cosmological B-mode signal has the same spatial pattern and amplitude at all frequencies, but foregrounds such as synchrotron and dust emission change amplitude. Since we released a result detecting a B-mode signal at 150 GHz in 2014 [47], we upgraded two receivers of the *Keck Array* to observe at 95 GHz (in 2014 and 2015) and two more receivers to observe at 220 GHz (in 2015). We continued observing at higher frequencies in 2016 and 2017 with *Keck* and observed at 95 GHz in 2016 and 2017 with BICEP3, but those data are not yet at a mature enough stage of analysis to present here. Therefore, this chapter deals only with BICEP2 data and *Keck* data through 2015 (collectively referred to as "BK15").

6.1 Maps

We begin by looking at E-mode maps of the 2015 *Keck* data, shown in Figure 6.1. The process for creating these maps is described in Chapter 3. With data from only 2015, these

maps contain two receiver-years of data at 95 GHz, a single receiver-year at 150 GHz, and two receiver-years at 220 GHz. Nonetheless, we see that the E-mode maps are highly correlated at the three frequencies, which indicates ΛCDM E-modes are the dominant signal at all of these frequencies, and noise is sub-dominant.

Next we look at BK15 maps. These are presented in Figures 6.2 to 6.4, and show T, Q, and U signal maps as well as a noise realization for the three observation frequencies. At all frequencies, the patterns characteristic of ΛCDM E-modes are visible in the Q and U maps. Also, as we move to higher frequency, the size of the beam decreases, which increases the resolution of the map. This is most clear when comparing the T maps at the different frequencies.

6.2 BK15 Spectra

We next calculate the power spectra of the BK15 maps by apodizing with a smoothed version of the inverse variance maps, calculating the two-dimensional Fourier transform, converting from Q and U to E and B, squaring, and collapsing to one-dimensional power spectra by taking the mean within annular bins in the Fourier plane. The procedure is more fully explained in Section 3.6. A purification matrix (explained in Section 3.6.1), calculated for each frequency, is applied in the process of calculating the power spectra. The first five band powers of these spectra are shown in Figure 6.5 for the three frequencies of BK15 data and for the *Planck* 353 GHz spectra. Error bars are derived from the standard deviation of 499 realizations of lensed-ΛCDM+dust+noise simulations. Red solid and dashed curves represent expectation values for two different dust models that will be explained in Section 6.3.

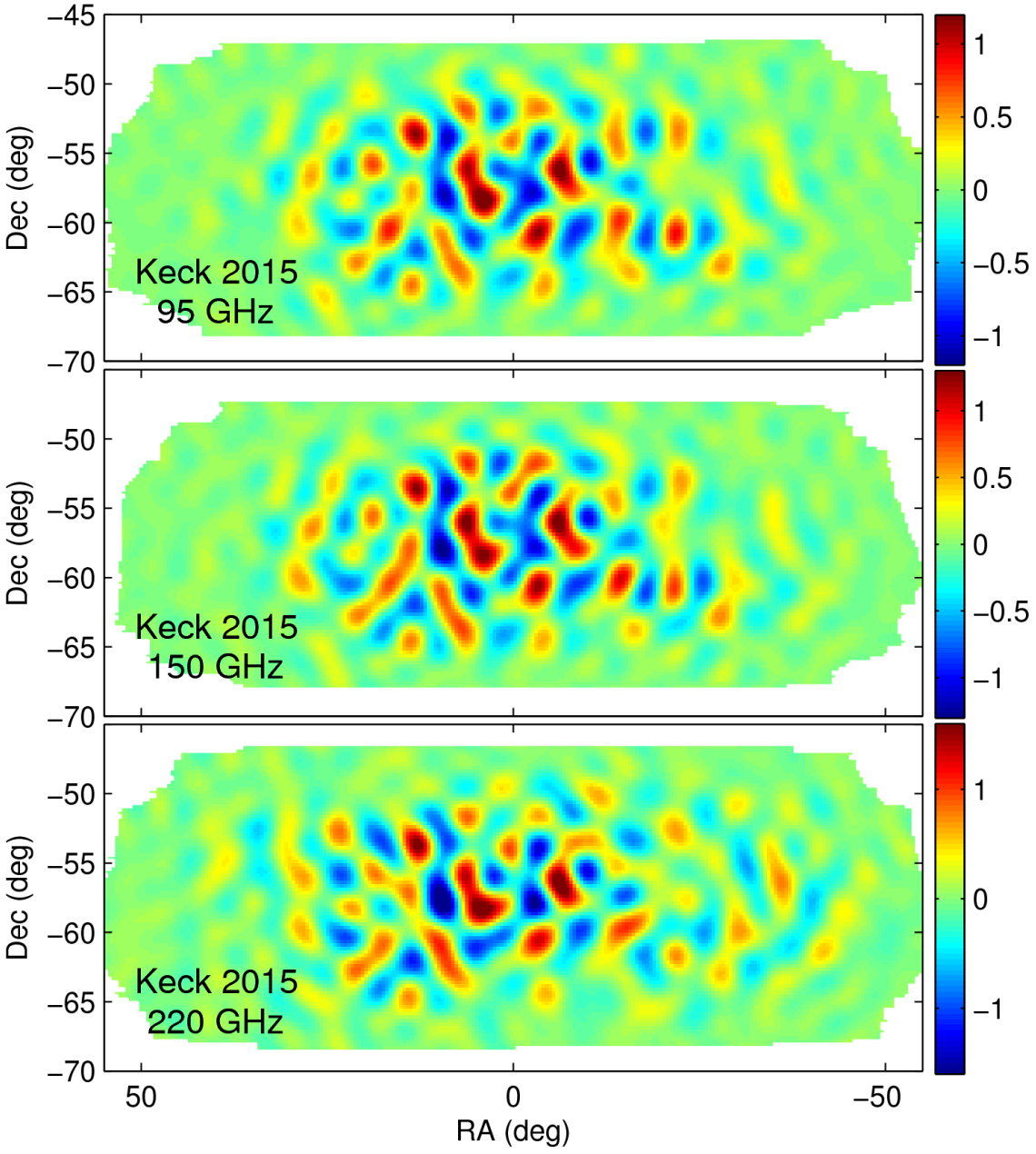

Figure 6.1: Maps of E-modes at the three frequencies recorded with the *Keck Array* telescopes during the 2015 season. These maps are filtered to include only multipoles in the range $50 < \ell < 120$. The correlation between the maps indicates a strong detection of ΛCDM E-modes. The color scale is in units of μK_{CMB}, and the range varies slightly between panels to compensate for the decreasing beam size at higher frequencies. This figure is courtesy of the BICEP2 and *Keck Array* collaborations.

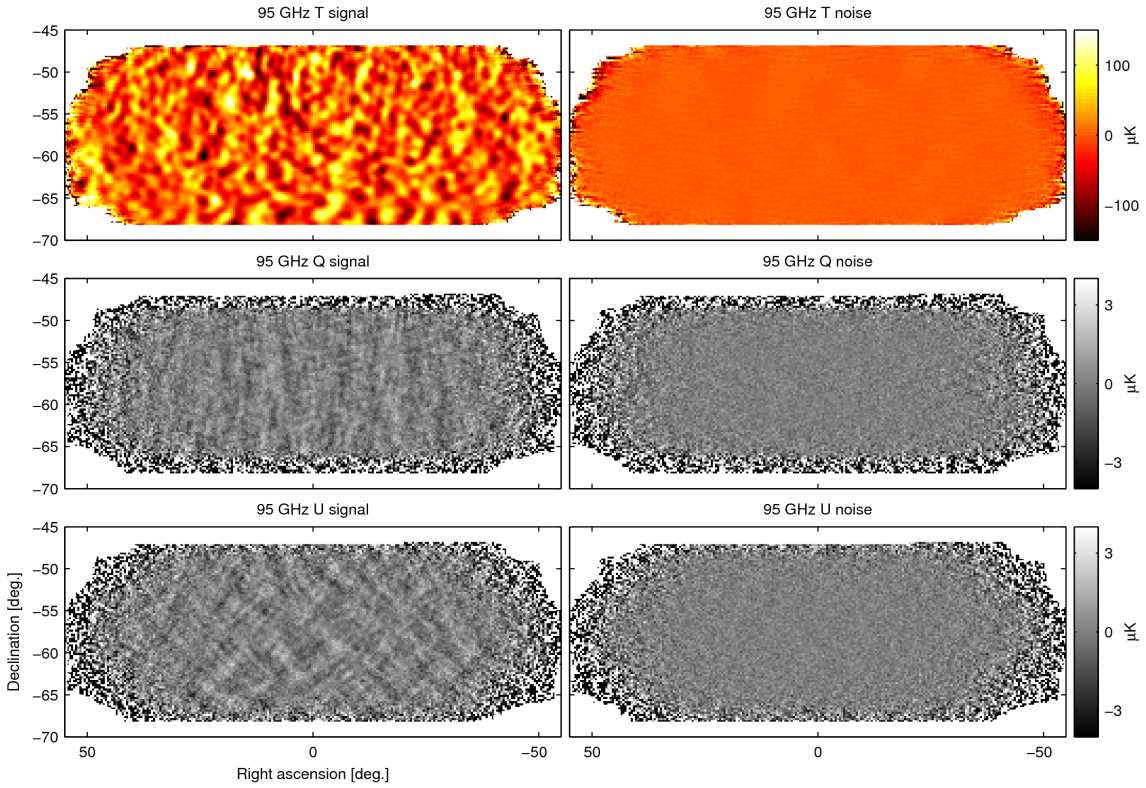

Figure 6.2: The T, Q, and U maps for all 95 GHz data through 2015, which includes two receivers for two years. The left column contains the signal maps, and the right column shows a sign-flip noise realization (see Section 3.5). The horizontal/vertical stripes in Q and crosshatch pattern in U indicate an E-mode-dominated sky. The FHWM size of the *Keck* 95 GHz beams is $\sim 43'$. This figure is courtesy of the BICEP2 and *Keck Array* collaborations.

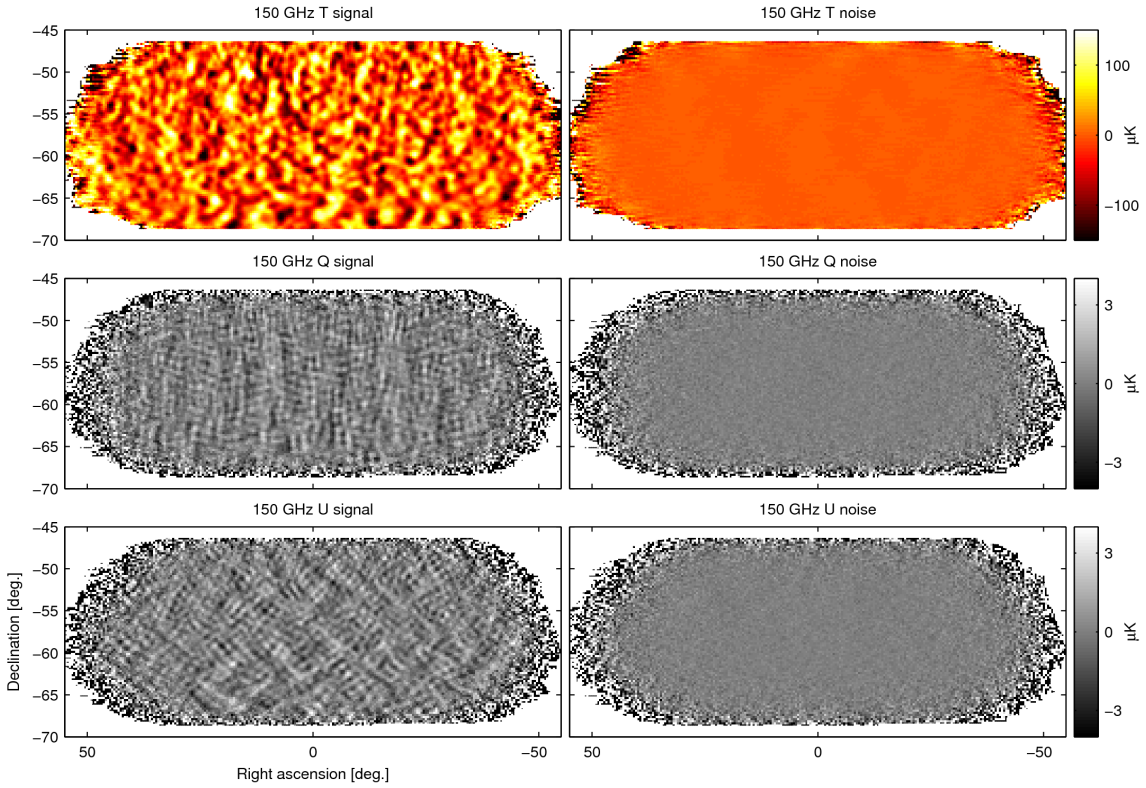

Figure 6.3: The T, Q, and U maps for all 150 GHz data through 2015, which includes 17 receiver-years. These maps are analogous to those shown for 95 GHz in Figure 6.2. Visually, we can see that the 150 GHz maps are deeper than the 95 GHz since the Q and U noise maps are lower. Also, we see more detail in the signal maps due to the smaller beam, $\sim 30'$ FWHM. This figure is courtesy of the BICEP2 and *Keck Array* collaborations.

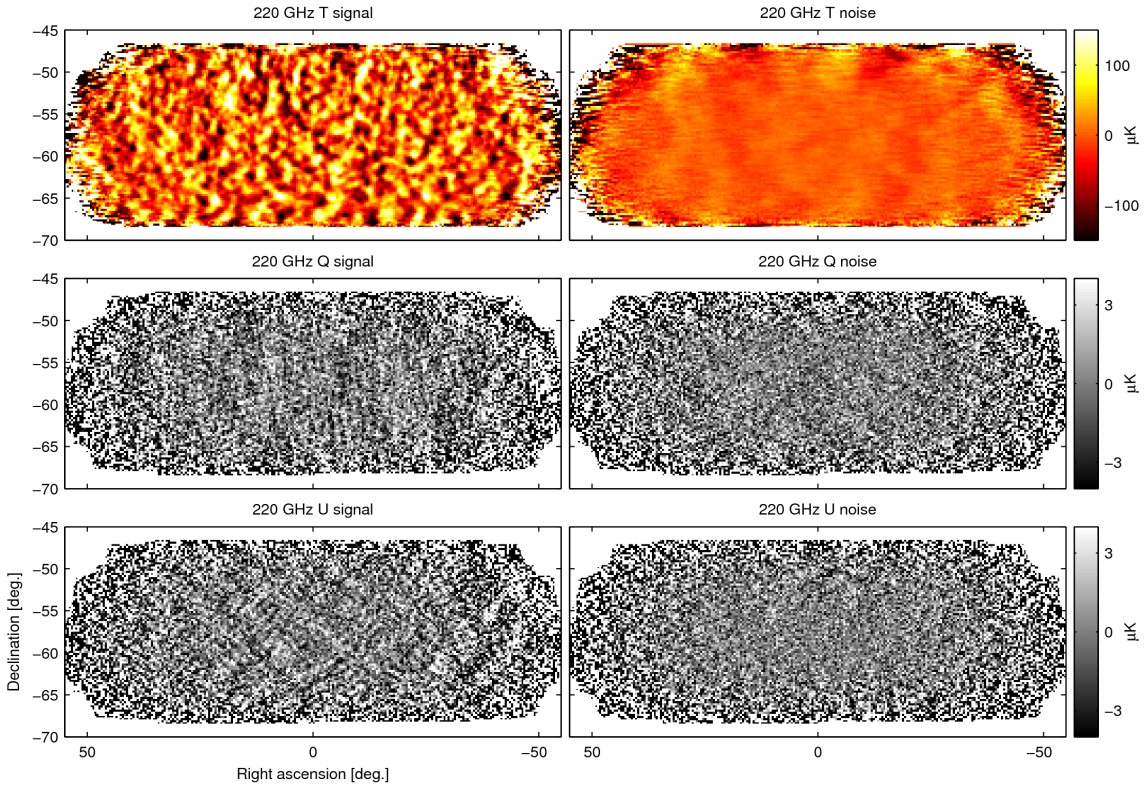

Figure 6.4: The T, Q, and U maps for all 220 GHz data through 2015, which includes two receivers for one year. These maps are analogous to those shown in Figures 6.2 and 6.3. The smaller beam size ($\sim 21'$) clearly reveals finer-scale structure in temperature anisotropies. Even though the signal-to-noise is lower, the predominant E-mode-pattern is visible in Q and U. This figure is courtesy of the BICEP2 and *Keck Array* collaborations.

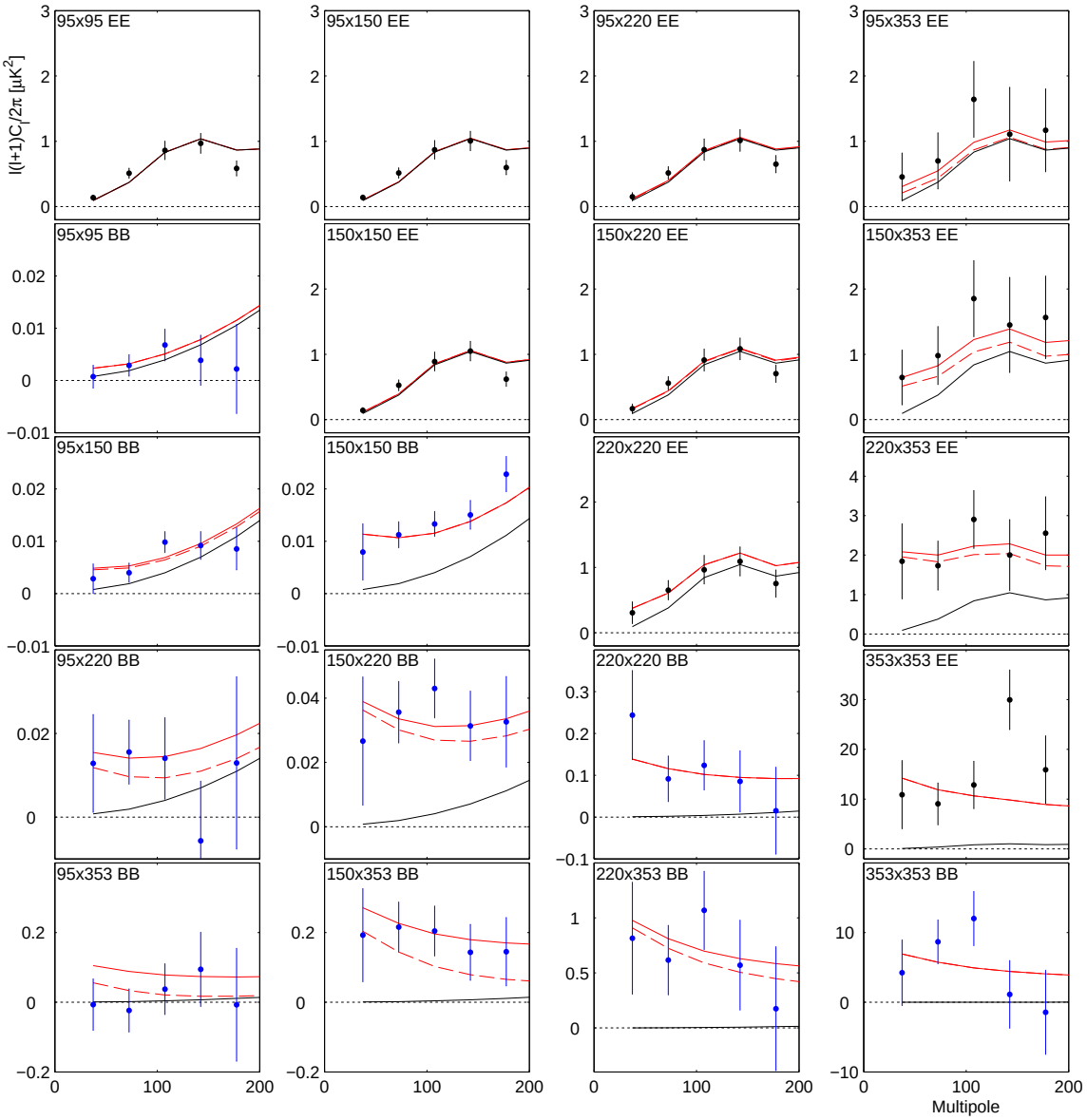

Figure 6.5: Preliminary auto and cross spectra for EE (black points) and BB (blue points) using all BICEP2/*Keck* data through 2015 as well as the *Planck* 353 GHz map. The frequency coverage of BICEP2/*Keck* is 95, 150, and 220 GHz. Black solid lines indicate the expectation values for a lensed-ΛCDM model. The solid red lines are the expectation values for the baseline lensed-ΛCDM+dust model from our BK14 analysis, which includes BICEP2 and *Keck* data for all years to 2014, ($A_{\rm d,353} = 4.3\mu{\rm K}^2, \beta_{\rm d} = 1.6, \alpha_{\rm d} = -0.4$) [76]. The dashed red lines are the modification to the solid red lines when decorrelation of dust between the frequencies is introduced and has a parameter $\mathcal{R}_{\ell=80}^{217\times353} = 0.85$ as suggested in reference [77]. This figure is courtesy of the BICEP2 and *Keck Array* collaborations.

6.3 Likelihood Analysis

In order to separate components which contribute to our measured signal, we perform a multi-component likelihood analysis based on the Hamimeche-Lewis approximation (HL) [78]. We marginalize over varying models using the auto and cross spectra of the data and their covariances. A breakdown of the model, composed of lensed-ΛCDM+r+foregrounds, is displayed in Figure 6.6. The lensing amplitude is captured by the parameter $A_{\rm L}$, while the foregrounds have separate parameters for dust and synchrotron. Both synchrotron and dust have an amplitude parameter A specified at the $\ell \simeq 80$ band power at 353 GHz for dust and 23 GHz for synchrotron. Both also have parameters β and α for a frequency spectral index and spatial spectral index, respectively. Dust also has two more parameters to describe the greybody temperature, $T_{\rm d}$ and decorrelation of the dust signal between frequencies, $\mathcal{R}$. A final parameter, ϵ, specifies the level of spatial correlation between synchrotron and dust.

In our BICEP2 results paper [47], we used WMAP K-band (23 GHz) and BICEP1 100 GHz maps, which placed strong constraints on the amount of synchrotron radiation in our detected signal. We then collaborated with a team from the *Planck* satellite experiment [18], which added measurements at 30, 40, 70, 100, 143, 217, and 353 GHz. It is the higher frequency data, in conjunction with BICEP2/*Keck* 150 GHz data which allowed a determination that most of the B-mode-signal reported in the BICEP2 results paper is due to foreground dust.

After the 2014 season, which added the first two receiver-years at 95 GHz for the *Keck Array*, we were able to constrain $r_{0.05} < 0.07$ at 95% confidence [76]. These are the strongest constraints on r in released analyses to date, surpassing what is possible with temperature anisotropies alone [18]. Figure 6.7 shows the results of the baseline analysis that was presented in BICEP2/*Keck Array* VI [76] using BK14 data (all BICEP2 and *Keck* data up to and including 2014) with external frequency bands from WMAP and *Planck*.

Now we move on to the inclusion of the 2015 season of *Keck*, which adds two receivers at 220 GHz for the first time. Though the analysis is in an advanced state, the final results have not yet been released. Thefore, any results presented that involve this dataset are preliminary. Figure 6.8 shows the noise levels of various data sets for the multipole $\ell \sim 80$ BB bandpower. We can see that with a single season of *Keck* 220 GHz data, we are able to constrain the dust signal in our field to a similar precision as the *Planck* 353 GHz data. Even though the auto spectrum is noisier at 353 GHz than 220 GHz, the dust signal is also much stronger at 353 GHz.

One concern with the multi-frequency analysis is that dust may have a spatially varying frequency spectrum. If that's the case, then the dust power in the frequency cross spectra will be suppressed relative to the auto spectra. This in turn could bias a detection of r high. In the *Planck* intermediate paper XXX [50], no evidence was found for any significant decorrelation in our patch of sky. More recently, *Planck* intermediate results L [77] claimed evidence for dust decorrelation in our field. This paper was followed up by Sheehy and Slosar [79], who showed that the claims for dust decorrelation are not statistically significant in the available *Planck* data. More recently, the *Planck* collaboration released paper LIV stating there is no evidence on large scales for dust decorrelation [80]. We will be able to better constrain the level of dust decorrelation as the prescion of our multi-frequency measurements improves.

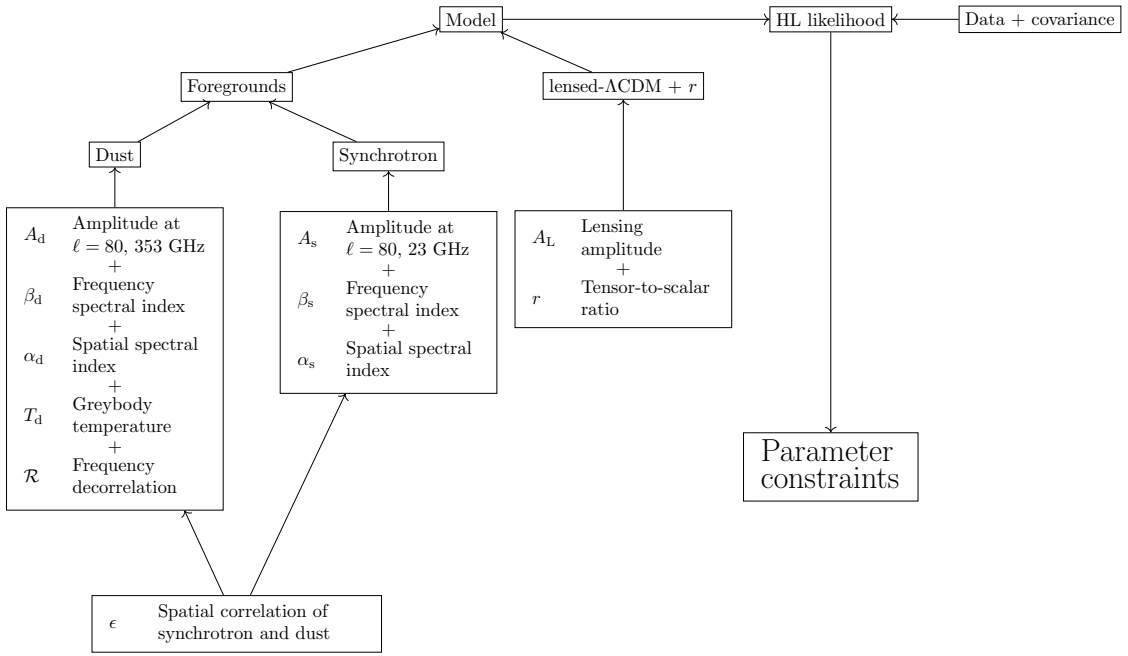

Figure 6.6: Flowchart of the likelihood analysis. Internal and external spectra, as well as their covariances, are simultaneously fit against the likelihood model. The model contains 11 parameters, any of which may be held at a constant value. The parameters can be broken up into categories of foregrounds, which includes dust and synchrotron, and lensed-ΛCDM. There are an additional two parameters that characterize the relative power in E-modes to B-modes for synchrotron and dust. Since we do no typically use the EE power spectra in our likelihood analysis, those two parameters are unused and are omitted from this flowchart.

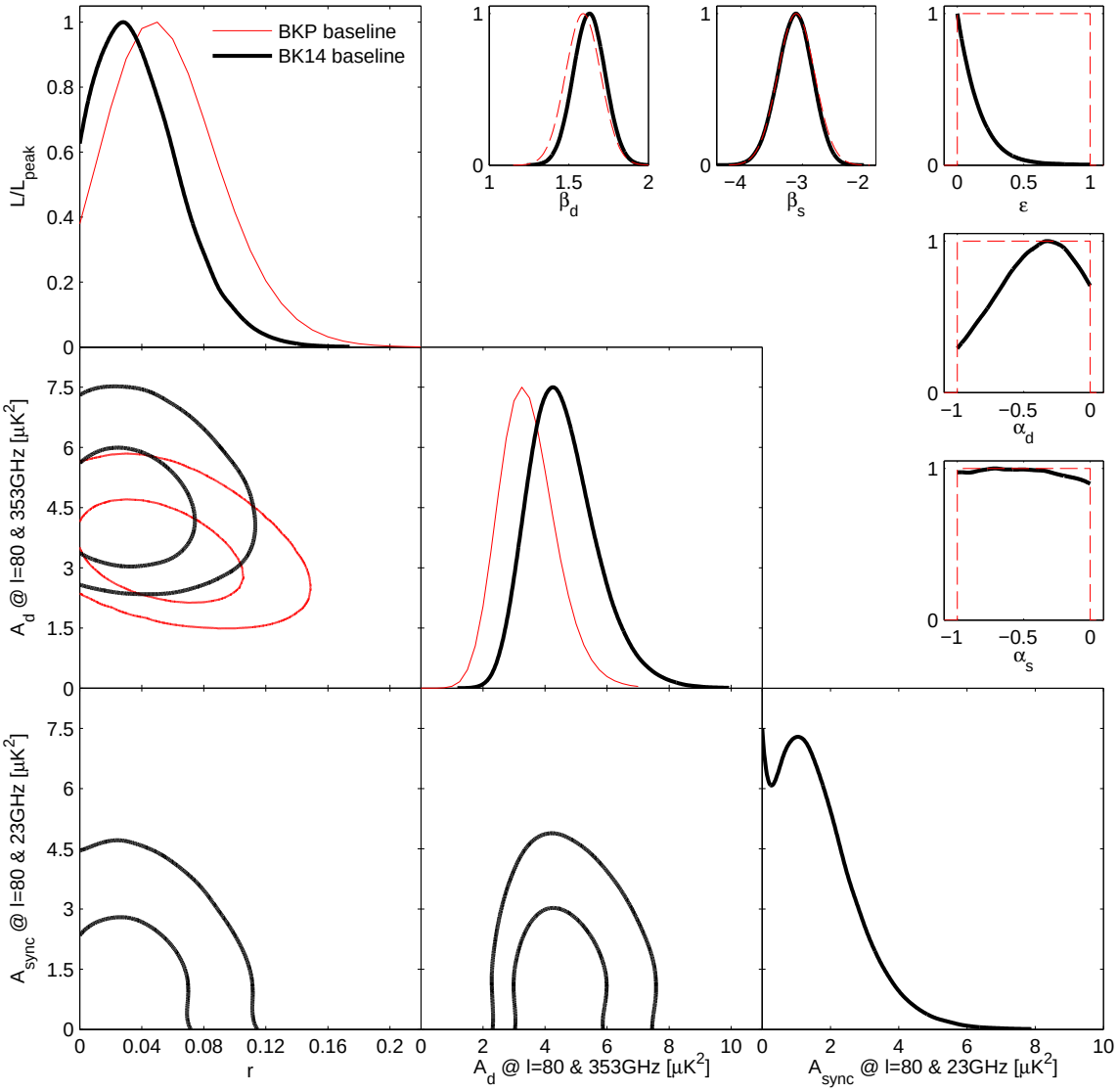

Figure 6.7: Results of the multi-component likelihood analysis using BICEP2/*Keck* data through 2014 as well as external data, shown with thick black curves. The thin red curves come from of our analysis of BICEP2/*Keck* data through 2013 in collaboration with *Planck* [18]. Besides including an additional year of *Keck* data, the black curves also include synchrotron and additional external frequency bands from WMAP and *Planck*. We see a slight shift down in the peak value of the tensor-to-scalar ratio r along with a slight increase in the frequency spectral component of dust β_d. Parameters A_d and A_sync are the amplitudes of the dust and synchrotron B-mode power spectra, and the α's are the spatial spectral indices. Finally, ϵ is the correlation coefficient between the dust and synchrotron patterns on the sky. This figure is taken from BICEP2/*Keck Array* VI [76].

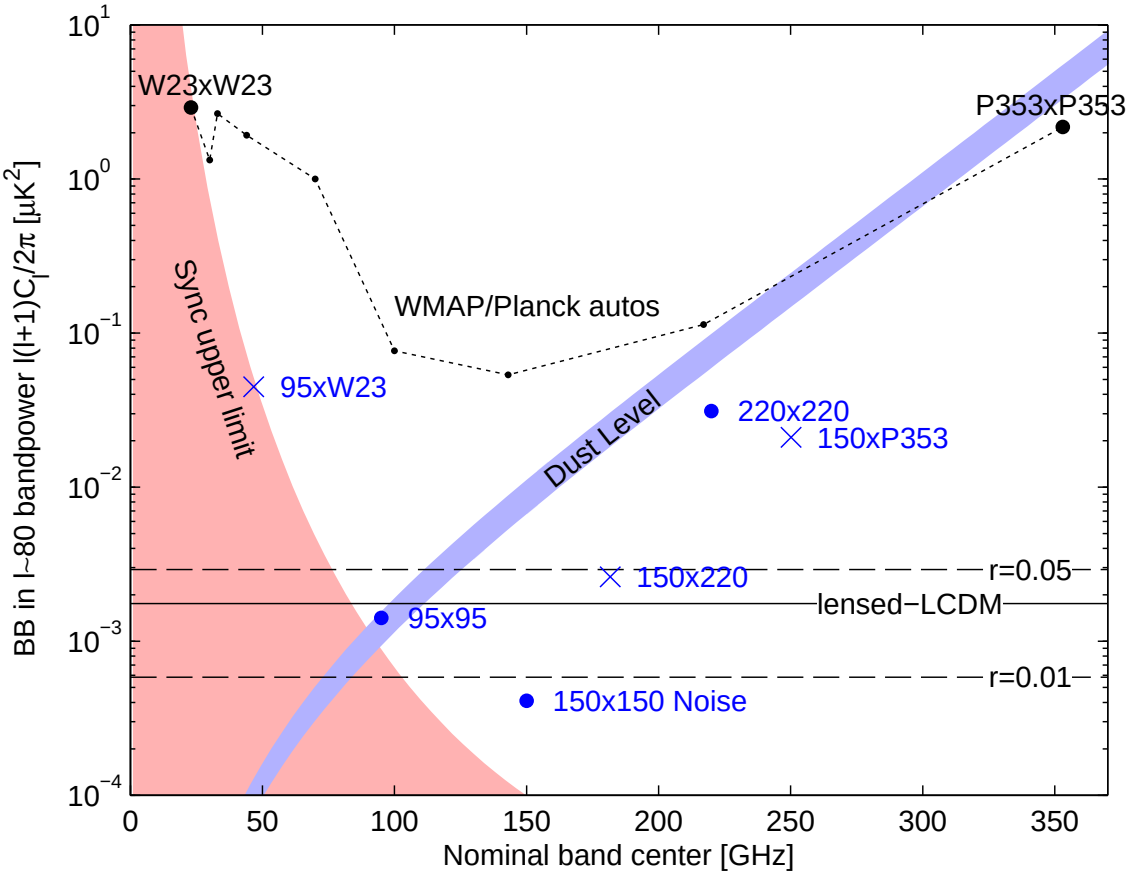

Figure 6.8: Current noise levels for the $\ell \sim 80$ BB band power in the BICEP2/*Keck* field for various auto and cross spectra of WMAP, *Planck*, and BICEP2/*Keck*. The blue band is a dust model consistent with our baseline analysis ($A_{\rm d,353} = 4.3^{+1.2}_{-1.0}\mu K^2$, $\beta_{\rm d} = 1.6$), and the red shaded region shows the allowed levels of synchrotron ($A_{\rm sync,23} < 3.8\mu K^2(95\%)$, $\beta_{\rm s} = -3.1$). Although the noise levels are based on BICEP2/*Keck* data through 2015, the baseline analysis presented in this figure is the result of the likelihood analysis of the data through 2014 since the analysis is not yet complete on the data through 2015. This figure is courtesy of the BICEP2 and *Keck Array* collaborations.

Chapter 7

CONCLUSIONS

Gravitational waves from Inflation have the potential to imprint a measurable B-mode signal in the Cosmic Microwave Background. It is this B-mode signal, with the expectation that it would peak at degree angular scales, that the family of BICEP and *Keck Array* telescopes have been designed to detect. To meet this goal, our telescopes are sited near the geographic south pole, renowned for its stable and dry atmosphere. Our telescopes also have small apertures, are located in reflective ground shields, employ comoving baffles, and are housed in a mount with a third rotation axis (aligned with the telescope boresight) that allows us to rotate our detectors' polarization angles with respect to the sky. These design choices were made in order to mitigate a class of systematics that cause false B-modes.

With our measurements of the CMB polarization, we have the potential to constrain exotic physical models in addition to our primary goal of measuring primordial B-modes. In particular, the CMB polarization serves as a probe for parity-violating physics such as cosmic birefringence, a uniform rotation of linearly polarized light over cosmological distances. Without a precise measurement of our detectors' polarization angles, we've relied on self-calibration to determine the global rotation of our polarization angles. Self-calibration,

however, eliminates our ability to measure an overall polarization angle rotation from cosmic birefringence. Therefore, a large focus of this dissertation has been on the Dielectric Sheet Calibrator, a device designed and built to measure our detectors' polarization angles as projected on the sky. Given the statistical uncertainties attained by other experiments and listed in Table 1.1, our minimum goal was to measure the absolute polarization angles of our detectors to better than $0.^{\circ}5$, though we'd like to measure the average angle to better than $0.^{\circ}1$. Due to an excess signal not accounted for in our DSC model, we were unable to measure the polarization angles of individual detectors. Instead we used pair differenced data that showed much better agreement with the model, indicating the excess signal is mostly common-mode. We performed a series of measurements to investigate the level of changing systematics from reassembling the DSC and found the measurements to be consistent to about $\pm 0.^{\circ}1$ in the mean across detector pairs. However, the angle by which the dielectric sheet is rotated about its major axis (denoted by γ in the model) was not measured and was assumed to be the design value of 0°. By allowing a conservative amount of machining tolerance in the DSC fabrication, we placed an upper limit on γ of $\pm 0.^{\circ}6$, which introduces an maximum uncertainty on the absolute polarization angles of $\pm 0.^{\circ}1$ in addition to the $\pm 0.^{\circ}1$ already mentioned.

Although we expect that we've met our goal of measuring the absolute polarization angles of our detectors, we trust the relative polarization angles to a much higher precision. Even though the relative polarization angles from DSC measurements were used in the mainline analysis of BICEP2 data, they have not been used in the mainline analysis of *Keck* data. The primary reason is that there is no DSC calibration data taken on detectors which are no longer in the field but which comprise a large fraction of the *Keck* CMB data. We have, however, inserted the relative polarization angles, measured on one 150 GHz receiver,

into simulations and found that the resulting bias on our B-mode measurements is very small.

In addition to the DSC calibration data, we've collected polarized calibration data on the *Keck Array* using the Rotating Polarized Source, a calibrator with a set of possible systematics independent from the DSC. When this dataset is analyzed, we'll be able to place tighter constraints on the uncertainties of our absolute polarization angle measurements. Another goal is to obtain polarization angles using individual detector data with the DSC instead of the currently used per-pair data. This will require further understanding of the source of the excess common-mode signal that plagues our current polarization angle calibration data. It is possible that we can reduce this excess signal by increasing the diameter of the baffle and covering the aluminum clamping ring in the same absorptive material as the baffle.

Returning to the main scientific goal of our program, we again note that the BICEP and *Keck* family of telescopes have acquired the most sensitive measurments of the CMB polarization to date. With these measurements, we've placed tighter constraints on the level of primordial B-modes than is possible with measurements of the CMB temperature, alone. Also, we're the only experiment to have detected B-modes from gravitational lensing at large angular scales. While our detections were originally acquired only at 150 GHz, we've added additional observations at multiple frequencies. With only a year of observations, BICEP3 has produced deeper maps at 95 GHz than two *Keck* receivers did in two years. *Keck* has also added observations at 210, 220, and 270 GHz, which will provide a better measurement on the level that foregrounds contribute to our polarization measurements. With these continued measurements, and the future multi-frequency measurements from the exciting next generation BICEP Array telescope, we look forward to gaining understanding on the origin of the Universe and providing another piece of the answer to the question,

“What is our place in the Universe?”

BIBLIOGRAPHY

[1] Kelvin K. S. Wu, Ofer Lahav, and Martin J. Rees. In: *Nature* 397.6716 (Jan. 1999), pp. 225–230. DOI: 10.1038/16637. URL: https://doi.org/10.1038/16637.

[2] Jaswant Yadav et al. "Testing homogeneity on large scales in the Sloan Digital Sky Survey Data Release One". In: *Monthly Notices of the Royal Astronomical Society* 364.2 (2005), pp. 601–606. DOI: 10.1111/j.1365-2966.2005.09578.x. eprint: /oup/backfile/content_public/journal/mnras/364/2/10.1111_j.1365-2966.2005.09578.x/1/364-2-601.pdf. URL: http://dx.doi.org/10.1111/j.1365-2966.2005.09578.x.

[3] C. Patrignani and Particle Data Group. "Review of Particle Physics". In: *Chinese Physics C* 40.10 (2016), p. 100001. URL: http://stacks.iop.org/1674-1137/40/i=10/a=100001.

[4] Barbara Ryden. *Introduction to Cosmology*. 1301 Sansome St., San Francisco, CA 94111: Addison Wesley, 2003. ISBN: 0-8053-8912-1.

[5] E. Hubble. "A Relation between Distance and Radial Velocity among Extra-Galactic Nebulae". In: *Proceedings of the National Academy of Science* 15 (Mar. 1929), pp. 168–173. DOI: 10.1073/pnas.15.3.168.

[6] A. A. Penzias and R. W. Wilson. “A Measurement of Excess Antenna Temperature at 4080 Mc/s.” In: *Astrophys. J.* 142 (July 1965), pp. 419–421. DOI: 10.1086/148307.

[7] H. Bondi and T. Gold. “The steady-state theory of the homogeneous expanding universe”. In: *The Observatory* 74 (Feb. 1954), pp. 36–37.

[8] F. Hoyle. “A New Model for the Expanding Universe”. In: *Monthly Notices of the Royal Astronomical Society* 108.5 (1948), p. 372. DOI: 10.1093/mnras/108.5.372. eprint: /oup/backfile/content_public/journal/mnras/108/5/10.1093_mnras_108.5.372/2/mnras108-0372.pdf. URL: http://dx.doi.org/10.1093/mnras/108.5.372.

[9] Planck Collaboration et al. “Planck 2015 results. I. Overview of products and scientific results”. In: *Astr. & Astroph.* 594, A1 (Sept. 2016), A1. DOI: 10.1051/0004-6361/201527101. arXiv: 1502.01582.

[10] Marc Kamionkowski, Arthur Kosowsky, and Albert Stebbins. “A Probe of Primordial Gravity Waves and Vorticity”. In: *Phys. Rev. Lett.* 78 (11 Mar. 1997), pp. 2058–2061. DOI: 10.1103/PhysRevLett.78.2058. URL: https://link.aps.org/doi/10.1103/PhysRevLett.78.2058.

[11] Matias Zaldarriaga. “Nature of the $E-B$ decomposition of CMB polarization”. In: *Phys. Rev. D* 64 (10 Oct. 2001), p. 103001. DOI: 10.1103/PhysRevD.64.103001. URL: https://link.aps.org/doi/10.1103/PhysRevD.64.103001.

[12] Sarah Kernasovskiy. “Measuring the Polarization of the Cosmic Microwave Background with the Kecky Array and Bicep2”. PhD thesis. Stanford University, 2014.

[13] W. Hu and M. White. “A CMB polarization primer”. In: 2 (Oct. 1997), pp. 323–344. DOI: 10.1016/S1384-1076(97)00022-5. eprint: astro-ph/9706147.

[14] Matias Zaldarriaga and Uro š Seljak. “Gravitational lensing effect on cosmic microwave background polarization”. In: *Phys. Rev. D* 58 (2 June 1998), p. 023003. DOI: 10.1103/PhysRevD.58.023003. URL: https://link.aps.org/doi/10.1103/PhysRevD.58.023003.

[15] D. Hanson et al. “Detection of B-Mode Polarization in the Cosmic Microwave Background with Data from the South Pole Telescope”. In: *Physical Review Letters* 111.14, 141301 (Oct. 2013), p. 141301. DOI: 10.1103/PhysRevLett.111.141301. arXiv: 1307.5830 [astro-ph.CO].

[16] P. A. R. Ade et al. “Evidence for Gravitational Lensing of the Cosmic Microwave Background Polarization from Cross-Correlation with the Cosmic Infrared Background”. In: *Phys. Rev. Lett.* 112 (13 Apr. 2014), p. 131302. DOI: 10.1103/PhysRevLett.112.131302. URL: https://link.aps.org/doi/10.1103/PhysRevLett.112.131302.

[17] Alexander van Engelen et al. “The Atacama Cosmology Telescope: Lensing of CMB Temperature and Polarization Derived from Cosmic Infrared Background Cross-correlation”. In: *The Astrophysical Journal* 808.1 (2015), p. 7. URL: http://stacks.iop.org/0004-637X/808/i=1/a=7.

[18] P. A. R. Ade et al. “Joint Analysis of BICEP2/Keck Array and Planck Data”. In: *Phys. Rev. Lett.* 114 (10 Mar. 2015), p. 101301. DOI: 10.1103/PhysRevLett.114.101301. URL: https://link.aps.org/doi/10.1103/PhysRevLett.114.101301.

[19] Kevork N. Abazajian et al. “CMB-S4 Science Book, First Edition”. In: (2016). arXiv: 1610.02743 [astro-ph.CO].

[20] Alan H. Guth. “Inflationary universe: A possible solution to the horizon and flatness problems”. In: *Phys. Rev. D* 23 (2 Jan. 1981), pp. 347–356. DOI: 10.1103/PhysRevD.23.347. URL: https://link.aps.org/doi/10.1103/PhysRevD.23.347.

[21] The LIGO Scientific Collaboration. “Advanced LIGO”. In: *Classical and Quantum Gravity* 32.7 (2015), p. 074001. URL: http://stacks.iop.org/0264-9381/32/i=7/a=074001.

[22] F Acernese et al. “Advanced Virgo: a second-generation interferometric gravitational wave detector”. In: *Classical and Quantum Gravity* 32.2 (2015), p. 024001. URL: http://stacks.iop.org/0264-9381/32/i=2/a=024001.

[23] L. Gottardi et al. “Sensitivity of the spherical gravitational wave detector MiniGRAIL operating at 5 K”. In: *Phys. Rev. D* 76 (10 Nov. 2007), p. 102005. DOI: 10.1103/PhysRevD.76.102005. URL: https://link.aps.org/doi/10.1103/PhysRevD.76.102005.

[24] Rainer Beck and Richard Wielebinski. “Magnetic Fields in Galaxies”. In: *Planets, Stars and Stellar Systems: Volume 5: Galactic Structure and Stellar Populations*. Ed. by Terry D. Oswalt and Gerard Gilmore. Dordrecht: Springer Netherlands, 2013, pp. 641–723. ISBN: 978-94-007-5612-0. DOI: 10.1007/978-94-007-5612-0_13. URL: https://doi.org/10.1007/978-94-007-5612-0_13.

[25] Eugene Hecht. *Optics (5th Edition)*. Pearson, 2017. ISBN: 0133977226.

[26] T. D. Lee and C. N. Yang. “Question of Parity Conservation in Weak Interactions”. In: *Phys. Rev.* 104 (1 Oct. 1956), pp. 254–258. DOI: 10.1103/PhysRev.104.254. URL: https://link.aps.org/doi/10.1103/PhysRev.104.254.

[27] C. S. Wu et al. “Experimental Test of Parity Conservation in Beta Decay”. In: *Phys. Rev.* 105 (4 Feb. 1957), pp. 1413–1415. DOI: 10.1103/PhysRev.105.1413. URL: https://link.aps.org/doi/10.1103/PhysRev.105.1413.

[28] J. H. Christenson et al. “Evidence for the 2π Decay of the K_2^0 Meson”. In: *Phys. Rev. Lett.* 13 (4 July 1964), pp. 138–140. DOI: 10.1103/PhysRevLett.13.138. URL: https://link.aps.org/doi/10.1103/PhysRevLett.13.138.

[29] D. Contreras, P. Boubel, and D. Scott. “Constraints on direction-dependent cosmic birefringence from Planck polarization data”. In: *ArXiv e-prints* (May 2017). arXiv: 1705.06387.

[30] Sean M. Carroll. “Quintessence and the Rest of the World: Suppressing Long-Range Interactions”. In: *Phys. Rev. Lett.* 81 (15 Oct. 1998), pp. 3067–3070. DOI: 10.1103/PhysRevLett.81.3067. URL: https://link.aps.org/doi/10.1103/PhysRevLett.81.3067.

[31] Mingzhe Li and Xinmin Zhang. “Cosmological CPT violating effect on CMB polarization”. In: *Phys. Rev. D* 78 (10 Nov. 2008), p. 103516. DOI: 10.1103/PhysRevD.78.103516. URL: https://link.aps.org/doi/10.1103/PhysRevD.78.103516.

[32] Maxim Pospelov, Adam Ritz, and Constantinos Skordis. “Pseudoscalar Perturbations and Polarization of the Cosmic Microwave Background”. In: *Phys. Rev. Lett.* 103 (5 July 2009), p. 051302. DOI: 10.1103/PhysRevLett.103.051302. URL: https://link.aps.org/doi/10.1103/PhysRevLett.103.051302.

[33] Fabio Finelli and Matteo Galaverni. “Rotation of linear polarization plane and circular polarization from cosmological pseudoscalar fields”. In: *Phys. Rev. D* 79 (6 Mar.

2009), p. 063002. DOI: 10.1103/PhysRevD.79.063002. URL: https://link.aps.org/doi/10.1103/PhysRevD.79.063002.

[34] Robert R. Caldwell, Vera Gluscevic, and Marc Kamionkowski. "Cross-correlation of cosmological birefringence with CMB temperature". In: *Phys. Rev. D* 84 (4 Aug. 2011), p. 043504. DOI: 10.1103/PhysRevD.84.043504. URL: https://link.aps.org/doi/10.1103/PhysRevD.84.043504.

[35] Guo-Chin Liu and Kin-Wang Ng. "Axion dark matter induced cosmic microwave background B modes". In: *Physics of the Dark Universe* 16 (2017), pp. 22–25. ISSN: 2212-6864. DOI: http://dx.doi.org/10.1016/j.dark.2017.02.004. URL: http://www.sciencedirect.com/science/article/pii/S2212686417300171.

[36] David J.E. Marsh. "Axion cosmology". In: *Physics Reports* 643 (2016). Axion cosmology, pp. 1–79. ISSN: 0370-1573. DOI: https://doi.org/10.1016/j.physrep.2016.06.005. URL: http://www.sciencedirect.com/science/article/pii/S0370157316301557.

[37] Jonathan P. Kaufman, Brian G. Keating, and Bradley R. Johnson. "Precision tests of parity violation over cosmological distances". In: *Monthly Notices of the Royal Astronomical Society* 455.2 (2016), pp. 1981–1988. DOI: 10.1093/mnras/stv2348. eprint: /oup/backfile/content_public/journal/mnras/455/2/10.1093_mnras_stv2348/2/stv2348.pdf. URL: http://dx.doi.org/10.1093/mnras/stv2348.

[38] Borge Nodland and John P. Ralston. "Indication of Anisotropy in Electromagnetic Propagation over Cosmological Distances". In: *Phys. Rev. Lett.* 78 (16 Apr. 1997),

pp. 3043–3046. DOI: 10.1103/PhysRevLett.78.3043. URL: https://link.aps.org/doi/10.1103/PhysRevLett.78.3043.

[39] M. Galaverni et al. “Cosmological birefringence constraints from CMB and astrophysical polarization data”. In: *Journal of Cosmology and Astroparticle Physics* 2015.08 (2015), p. 031. URL: http://stacks.iop.org/1475-7516/2015/i=08/a=031.

[40] E. Komatsu et al. “Five-Year Wilkinson Microwave Anisotropy Probe Observations: Cosmological Interpretation”. In: *The Astrophysical Journal Supplement Series* 180.2 (2009), p. 330. URL: http://stacks.iop.org/0067-0049/180/i=2/a=330.

[41] Luca Pagano et al. “CMB polarization systematics, cosmological birefringence, and the gravitational waves background”. In: *Phys. Rev. D* 80 (4 Aug. 2009), p. 043522. DOI: 10.1103/PhysRevD.80.043522. URL: https://link.aps.org/doi/10.1103/PhysRevD.80.043522.

[42] G. Hinshaw et al. “Nine-year Wilkinson Microwave Anisotropy Probe (WMAP) Observations: Cosmological Parameter Results”. In: *The Astrophysical Journal Supplement Series* 208.2 (2013), p. 19. URL: http://stacks.iop.org/0067-0049/208/i=2/a=19.

[43] J. P. Kaufman et al. “Self-calibration of BICEP1 three-year data and constraints on astrophysical polarization rotation”. In: *Phys. Rev. D* 89 (6 Mar. 2014), p. 062006. DOI: 10.1103/PhysRevD.89.062006. URL: https://link.aps.org/doi/10.1103/PhysRevD.89.062006.

[44] E. Y. S. Wu et al. “Parity Violation Constraints Using Cosmic Microwave Background Polarization Spectra from 2006 and 2007 Observations by the QUaD Polarimeter”. In: *Phys. Rev. Lett.* 102 (16 Apr. 2009), p. 161302. DOI: 10.1103/PhysRevLett.

102.161302. URL: https://link.aps.org/doi/10.1103/PhysRevLett.102.161302.

[45] K. Array et al. "BICEP2 / Keck Array IX: New Bounds on Anisotropies of CMB Polarization Rotation and Implications for Axion-Like Particles and Primordial Magnetic Fields". In: *ArXiv e-prints* (May 2017). arXiv: 1705.02523.

[46] D. Barkats et al. "Degree-scale Cosmic Microwave Background Polarization Measurements from Three Years of BICEP1 Data". In: *Astrophys. J.* 783, 67 (Mar. 2014), p. 67. DOI: 10.1088/0004-637X/783/2/67. arXiv: 1310.1422.

[47] BICEP2 Collaboration I. "BICEP2 I: Detection of B-Mode Polarization at Degree Angular Scales by BICEP2". In: *Physical Review Letters* 112.24, 241101 (June 2014), p. 241101. DOI: 10.1103/PhysRevLett.112.241101. arXiv: 1403.3985.

[48] BICEP2 Collaboration IV. "BICEP2/Keck Array IV: Optical Characterization and Performance of the BICEP2 and Keck Array Experiments". In: *Astrophys. J.* 806 (2015), p. 206.

[49] W. L. K. Wu et al. "Initial Performance of Bicep3: A Degree Angular Scale 95 GHz Band Polarimeter". In: *Journal of Low Temperature Physics* 184 (Aug. 2016), pp. 765–771. DOI: 10.1007/s10909-015-1403-x. arXiv: 1601.00125 [astro-ph.IM].

[50] Planck Collaboration Int. XXX. "Planck intermediate results. XXX. The angular power spectrum of polarized dust emission at intermediate and high Galactic latitudes". In: *ArXiv e-prints* (Sept. 2014). arXiv: 1409.5738.

[51] L. Duband and B. Collaudin. "Sorption coolers development at CEA-SBT". In: *Cryogenics* 39 (Dec. 1999), pp. 659–663. DOI: 10.1016/S0011-2275(99)00066-1.

[52] K. S. Karkare et al. “Optical Characterization of the BICEP3 CMB Polarimeter at the South Pole”. In: *ArXiv e-prints* (July 2016). arXiv: 1607.04567 [astro-ph.IM].

[53] B. G. Keating et al. “BICEP: a large angular scale CMB polarimeter”. In: *Polarimetry in Astronomy*. Ed. by S. Fineschi. Vol. 4843. Proc. of SPIE. Feb. 2003, pp. 284–295. DOI: 10.1117/12.459274.

[54] K. W. Yoon et al. “The Robinson Gravitational Wave Background Telescope (BICEP): a bolometric large angular scale CMB polarimeter”. In: *Society of Photo-Optical Instrumentation Engineers (SPIE) Conference Series*. Vol. 6275. Proc. of SPIE. June 2006, 62751K. DOI: 10.1117/12.672652. eprint: astro-ph/0606278.

[55] C. L. Kuo et al. *Antenna-coupled TES bolometer arrays for CMB polarimetry*. 2008. DOI: 10.1117/12.788588. URL: http://dx.doi.org/10.1117/12.788588.

[56] BICEP2/*Keck* and Spider Collaborations. “Antenna-coupled TES Bolometers Used in BICEP2, Keck Array, and Spider”. In: *Astrophys. J.* 812, 176 (Oct. 2015), p. 176. DOI: 10.1088/0004-637X/812/2/176. arXiv: 1502.00619 [astro-ph.IM].

[57] BICEP2 Collaboration II. “BICEP2 II: Experiment and Three-Year Data Set”. In: *Astrophys. J.* 792, 62 (Sept. 2014), p. 62. DOI: 10.1088/0004-637X/792/1/62. arXiv: 1403.4302.

[58] K.D. Irwin and G.C. Hilton. “Transition-Edge Sensors”. In: *Cryogenic Particle Detection*. Ed. by Christian Enss. Berlin, Heidelberg: Springer Berlin Heidelberg, 2005, pp. 63–150. ISBN: 978-3-540-31478-3. DOI: 10.1007/10933596_3. URL: https://doi.org/10.1007/10933596_3.

[59] W. L. K. Wu et al. “Initial Performance of Bicep3: A Degree Angular Scale 95 GHz Band Polarimeter”. In: *Journal of Low Temperature Physics* 184 (Aug. 2016), pp. 765–771. DOI: 10.1007/s10909-015-1403-x. arXiv: 1601.00125 [astro-ph.IM].

[60] J. A. Grayson et al. “BICEP3 performance overview and planned Keck Array upgrade”. In: *ArXiv e-prints* (July 2016). arXiv: 1607.04668 [astro-ph.IM].

[61] H. Hui et al. “BICEP3 focal plane design and detector performance”. In: *ArXiv e-prints* (July 2016). arXiv: 1607.06861 [astro-ph.IM].

[62] *Keck Array* and BICEP2 Collaborations VI. “BICEP2 / Keck Array VI: Improved Constraints On Cosmology and Foregrounds When Adding 95 GHz Data From Keck Array”. In: *ArXiv e-prints* (Oct. 2015). arXiv: 1510.09217.

[63] Grant Teply. “” PhD thesis. California Institute of Technology, 2015.

[64] URL: http://irsa.ipac.caltech.edu/data/Planck/release_1/all-sky-maps/previews/HFI_SkyMap_143_2048_R1.10_nominal/index.html.

[65] URL: http://irsa.ipac.caltech.edu/data/Planck/release_1/all-sky-maps/previews/HFI_SkyMap_100_2048_R1.10_nominal/index.html.

[66] URL: http://irsa.ipac.caltech.edu/data/Planck/release_1/all-sky-maps/previews/HFI_SkyMap_217_2048_R1.10_nominal/index.html.

[67] A. van Engelen et al. “A Measurement of Gravitational Lensing of the Microwave Background Using South Pole Telescope Data”. In: *The Astrophysical Journal* 756.2 (2012), p. 142. URL: http://stacks.iop.org/0004-637X/756/i=2/a=142.

[68] Kendrick M. Smith and Matias Zaldarriaga. “General solution to the $E-B$ mixing problem”. In: *Phys. Rev. D* 76 (4 Aug. 2007), p. 043001. DOI: 10.1103/PhysRevD.76.043001. URL: https://link.aps.org/doi/10.1103/PhysRevD.76.043001.

[69] P. A. R. Ade et al. “BICEP2/Keck Array. VII. Matrix Based E/B Separation Applied to Bicep2 and the Keck Array”. In: *The Astrophysical Journal* 825.1 (2016), p. 66. URL: http://stacks.iop.org/0004-637X/825/i=1/a=66.

[70] Y. D. Takahashi et al. “CMB polarimetry with BICEP: instrument characterization, calibration, and performance”. In: *Millimeter and Submillimeter Detectors and Instrumentation for Astronomy IV*. Vol. 7020. Proc. of SPIE. July 2008, p. 70201D. DOI: 10.1117/12.790306. arXiv: 0808.1763.

[71] Brian Koopman et al. “Optical modeling and polarization calibration for CMB measurements with ACTPol and Advanced ACTPol”. In: *Millimeter, Submillimeter, and Far-Infrared Detectors and Instrumentation for Astronomy VIII*. Ed. by Wayne S. Holland and Jonas Zmuidzinas. SPIE, July 2016. DOI: 10.1117/12.2231912. URL: https://doi.org/10.1117/12.2231912.

[72] C. W. O’Dell. “A New Upper Limit on the Large Angular Scale Polarization of the Cosmic Microwave Background Radiation”. PhD thesis. University of Wisconsin, Madison, 2001.

[73] Y. D. Takahashi. “Measurement of the Cosmic Microwave Background Polarization with the Bicep Telescope at the South Pole”. PhD thesis. University of California, Berkeley, 2010.

[74] R. W. Aikin. “Testing Inflationary Cosmology with the Bicep1 and Bicep2 Experiments”. PhD thesis. California Institute of Technology, 2013.

[75] F. James and M. Roos. “Minuit: A System for Function Minimization and Analysis of the Parameter Errors and Correlations”. In: *Comput. Phys. Commun.* 10 (1975), pp. 343–367. DOI: 10.1016/0010-4655(75)90039-9.

[76] P. A. R. Ade et al. “Improved Constraints on Cosmology and Foregrounds from BICEP2 and Keck Array Cosmic Microwave Background Data with Inclusion of 95 GHz Band”. In: *Phys. Rev. Lett.* 116 (3 Jan. 2016), p. 031302. DOI: 10.1103/PhysRevLett.116.031302. URL: https://link.aps.org/doi/10.1103/PhysRevLett.116.031302.

[77] Planck Collaboration Int. L. “Planck intermediate results. L. Evidence of spatial variation of the polarized thermal dust s pectral energy distribution and implications for CMB B-mode analysis”. In: *Astr. & Astroph.* 599, A51 (Mar. 2017), A51. DOI: 10.1051/0004-6361/201629164. arXiv: 1606.07335.

[78] Samira Hamimeche and Antony Lewis. “Likelihood analysis of CMB temperature and polarization power spectra”. In: *Phys. Rev. D* 77 (10 May 2008), p. 103013. DOI: 10.1103/PhysRevD.77.103013. URL: https://link.aps.org/doi/10.1103/PhysRevD.77.103013.

[79] C. Sheehy and A. Slosar. “No evidence for dust B-mode decorrelation in Planck data”. In: *ArXiv e-prints* (Sept. 2017). arXiv: 1709.09729.

[80] Planck Collaboration Int. LIV. *Planck intermediate results. LIV. Polarized dust foregrounds*. 2018. eprint: arXiv:1801.04945.

Appendix A

PER-DETECTOR POLARIZATION FITS

In Chapter 4, we used pair differenced data from the DSC to fit a single polarization angle to a detector pair. We would instead like to fit for the individual detector polarization angles but have not attained reasonable results. There appears to be additional signal in the individual detector data that is not accounted for in the model and which is, at least mostly, common-mode. Therefore, the excess signal cancels in the pair difference and does not affect the fits presented in Chapter 4. In this appendix, we explore the difference between the model and single-detector signal, and we leave the source of the discrepancy as an open question.

A.1 History

In our program, we first used a DSC with BICEP1 [73]. The same apparatus was later used with BICEP2 [74]. In both uses, different thicknesses of plastic were employed for the beam combiner, and BICEP1 even tried different materials. In many ways, the DSC built

Figure A.1: *Left*: DSC apparatus used on both the BICEP1 and BICEP2 telescopes. This figure is taken from BICEP2/*Keck Array* IV [48]. *Right*: DSC apparatus used with the *Keck* telescopes. Both images show the respective DSC mounted on the BICEP1 telescope and one of the five *Keck* telescopes. For scale comparison, the elliptical ring which clamps the plastic film has the same dimensions in both apparatuses.

for the *Keck Array* is like it's predecessor. Figure A.1 shows images of the two; they are both aluminum buckets with the same absorptive lining covered with the same foam, and they both use an aluminum elliptical clamping ring (with the same dimensions) to hold the dielectric sheet. However, we only used a 0.9 mil biaxially oriented polypropylene film with *Keck*. Additionally, the mechanism for rotating the calibrator differed between the two apparatuses. While BICEP1 and BICEP2 used the mount axes to rotate the calibrator, *Keck* used an external motor (under servo control) to rotate its calibrator.

Per-detector fits were used with BICEP1 DSC data and were attempted with BICEP2 data. Though the BICEP1 data and model appeared well-matched, the BICEP2 data and model did not. The lack of agreement in BICEP2 was attributed to sky fluctuations that were, common-mode between detectors of a pair. Therefore, the fitting was changed to use pairdiff data, and the agreement between data and model was improved. We will see below that sky fluctuations are not an issue for the *Keck* data.

A.2 Per-Detector Fits

Using calibration data taken on the *Keck Array* telescope during the 2014/2015 summer, we first show some of the data which displays the largest disagreement between model and data. We choose this data because it is the only year with calibration data at three frequencies—95, 150, and 220 GHz. Figures A.2 to A.4 show the data and fit for both detectors in a pair located near the corner of the focal plane for one of the 95, 150, and 220 GHz receivers, respectively. Both the per-detector and pairdiff data and their fits are shown to demonstrate the improvement when switching to pairdiff. Figures A.5 to A.7 show the same type of data for detector pairs located near the center of the focal planes. We are only able to provide rough estimates of the signals in temperature units since the data are taken with the detectors biased on the aluminum transition while our absolute calibration (see Section 3.4) is derived from CMB data taken with detectors biased on the titanium transition. Where A is the abscal value and E is the median of elnod gains (see Section 3.1.2) over detectors, we solve the following to estimate the abscal to use with data taken on the aluminum transition: $A_{\mathrm{Al}}E_{\mathrm{Al}} = A_{\mathrm{Ti}}E_{\mathrm{Ti}}$. Where a is the amplitude of the DSC signal, we expect the following relation with respect to frequency: $a \propto \nu^2$ [73]. Using this relation, it appears the ratio of the signals across frequency is correct to within a factor of two.

We make the following observations about the plots that were mentioned in the previous paragraph: (i) The agreement between data and model improves as the observation frequency increases. This appears to be the consequence of stronger signals at higher frequencies but similar residuals at all frequencies. (ii) The agreement between data and model is better for detector pairs closer to the center of the focal plane. (iii) The pair difference fitting eliminates much of the discrepancy between data and model. This suggest the source of the disagreement between per-detector data and model is common-mode for detectors within a

pair.

To explore the trend across the focal plane, Figure A.8 shows the best fit polarization offsets for the same data sets used in Figures A.2 to A.7. The polarization offset is the angle which needs to be subtracted from the design polarization angle. Like the plots for the individual detectors, the pair difference fitting produces a more uniform distribution of angles across the focal plane than the per-detector fitting. In addition to having larger disagreements between model and data timestreams, Figure A.8 shows us that the best fit model requires larger polarization angle offsets for detectors at lower observation frequencies. Also, we can see that the radial dependence of the offset angle is smooth from the center of the focal plane to the edges. We also see that there is a 2-ϕ dependence of the offset angle and that the A and B detectors within a pair are rotated in opposite directions from the mean shift. We further note that the relative pattern is independent of frequency.

If this effect is real instead of mismatch between calibration data and model, it has implications for our polarization data. In our analysis, we assume the polarization angles within a pair are orthogonal, but the analysis pipeline has the ability to account for any polarization angle for any detector. If a pair is not orthogonal, there is no leakage of temperature to polarization, but there is a loss of polarization efficiency. In that case our absolute calibration, derived from the TT spectrum (see Section 3.4), would be insufficient to calibrate our EE spectrum. Yet there is no evidence for large inconsistencies between ΛCDM-expected E-modes and our measured E-modes, nor is there evidence for a frequency-dependent effect [47, 76].

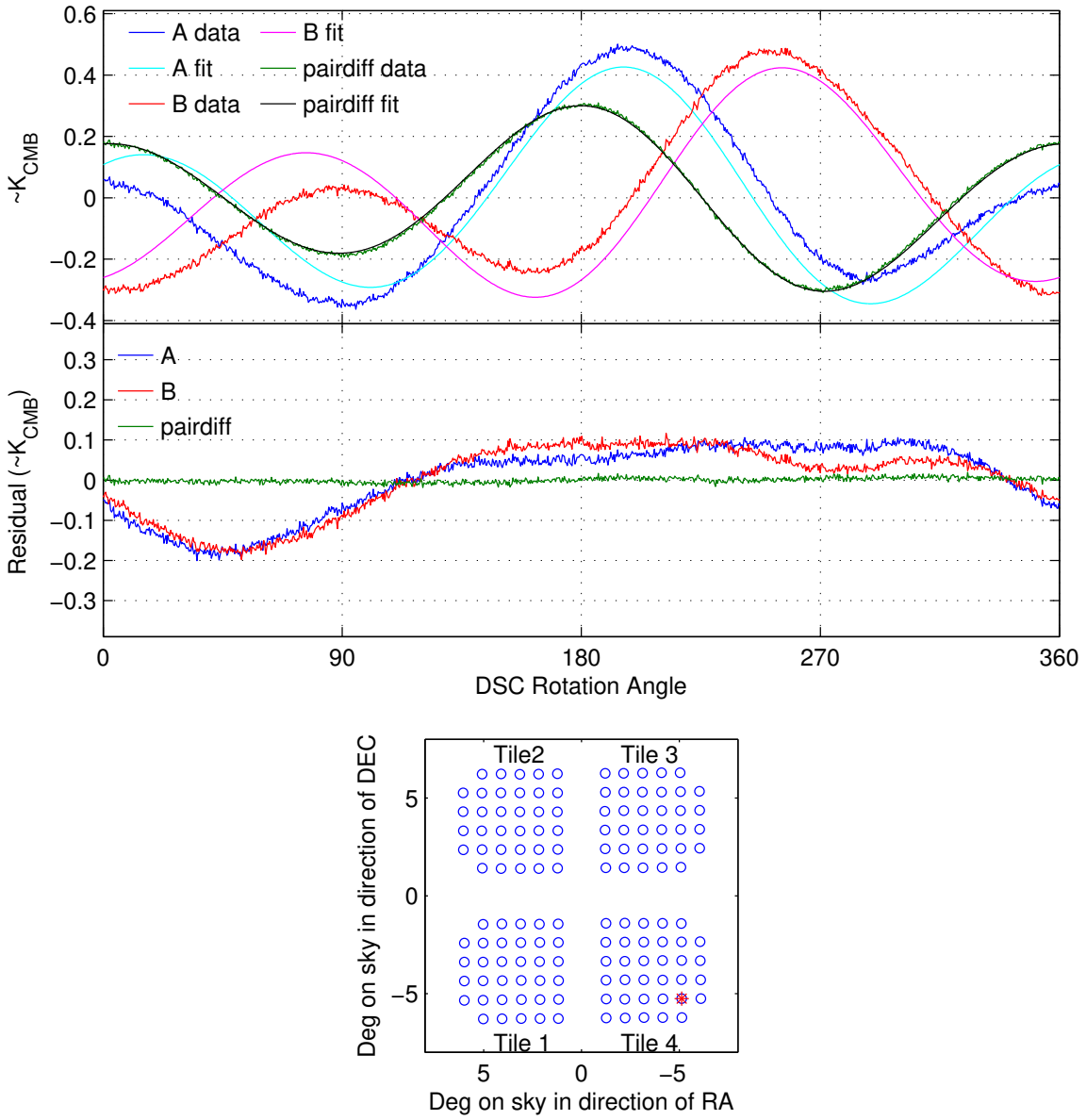

Figure A.2: *Top*: DSC signals and fits for one revolution of the calibrator for the individual detectors of a corner pair and for their difference. The vertical scale is roughly in temperature units. These data are taken from one calibration run on one 95 GHz receiver in the 2014/2015 summer season. For the A and B detector fits, the model is clearly unable to simultaneously match both peaks, but it is able to in the pair difference. *Middle*: The residual when subtracting the fit from the data. *Bottom*: The location of the plotted pair (red mark) in the focal plane. This should be interpreted as the angular distance (on the sky) of the detector pair from the boresight of the telescope.

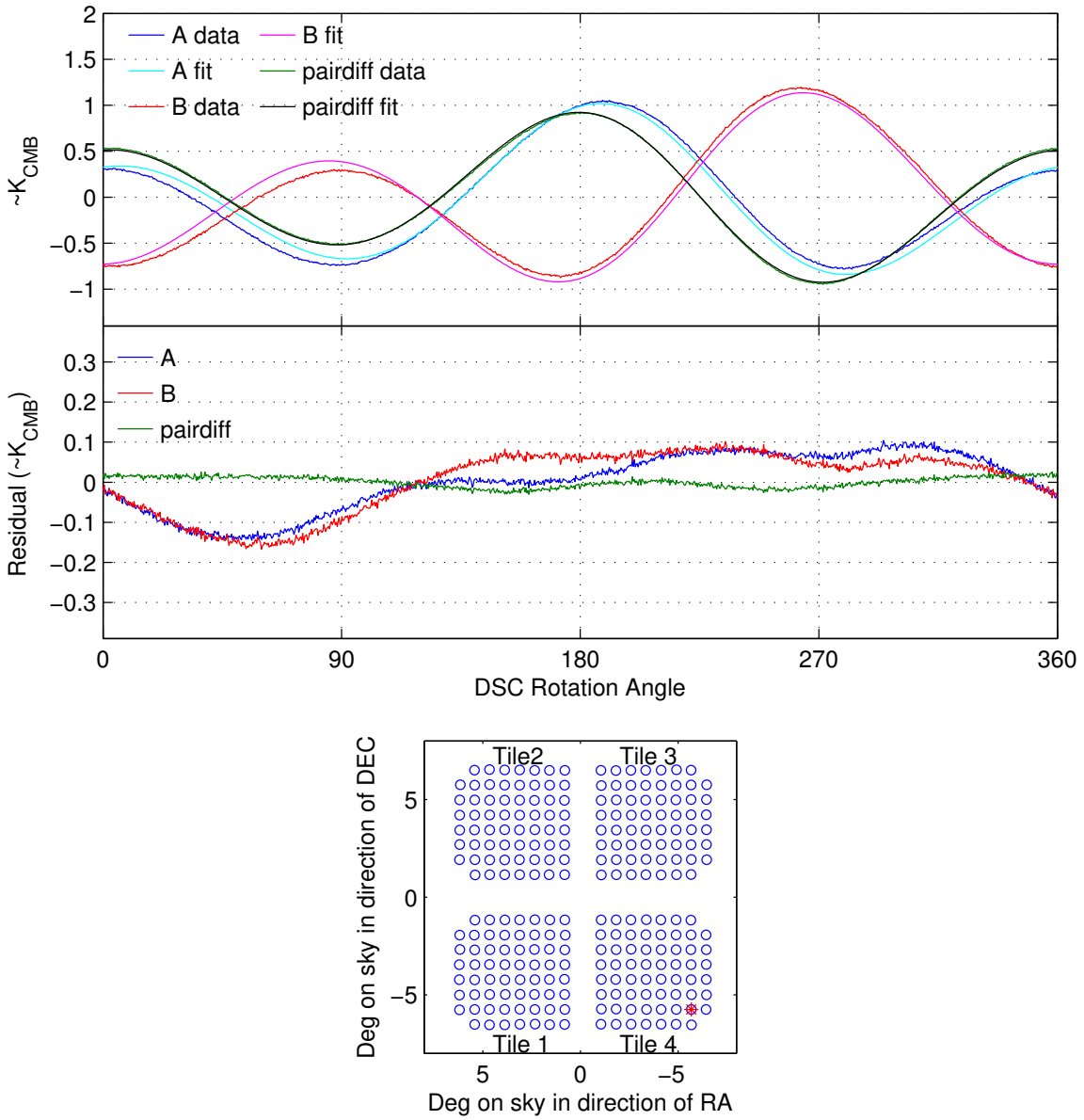

Figure A.3: A similar plot to Figure A.2 but for a 150-GHz detector pair. The data plotted are from one calibration run in the 2014/2015 summer season. The per-detector model is better able to match the peaks of the data than it was for the 95 GHz data, but it is still a worse match than the pairdiff data and model.

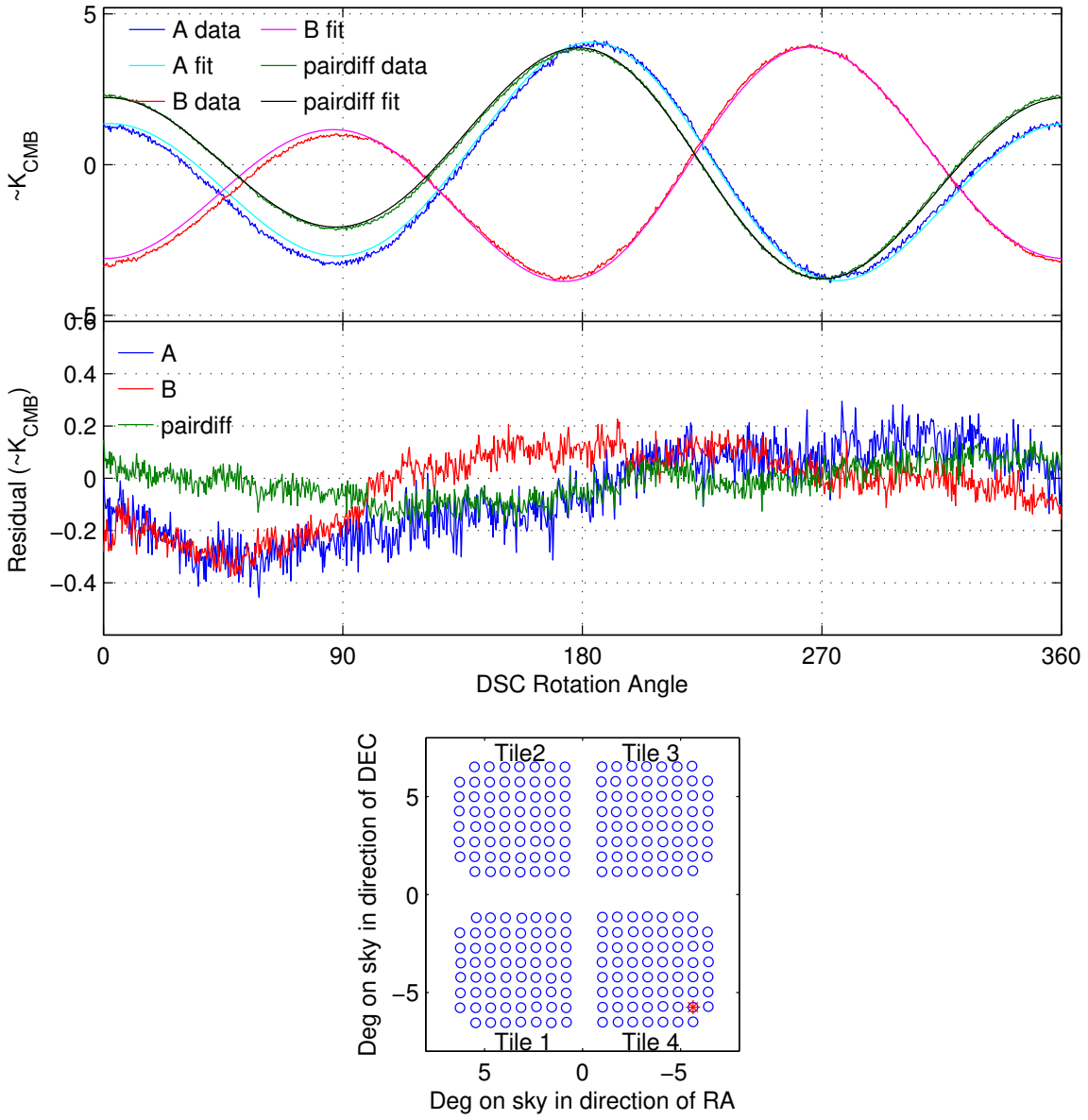

Figure A.4: A similar plot to Figures A.2 and A.3, but for one calibration run on one of the 220 GHz receivers during the 2014/2015 summer. There is additional improvement over the 150 GHz data presented in Figure A.3 in the agreement between per-detector data and model. The pairdiff data and model still match better than they do in the per-detector case, though.

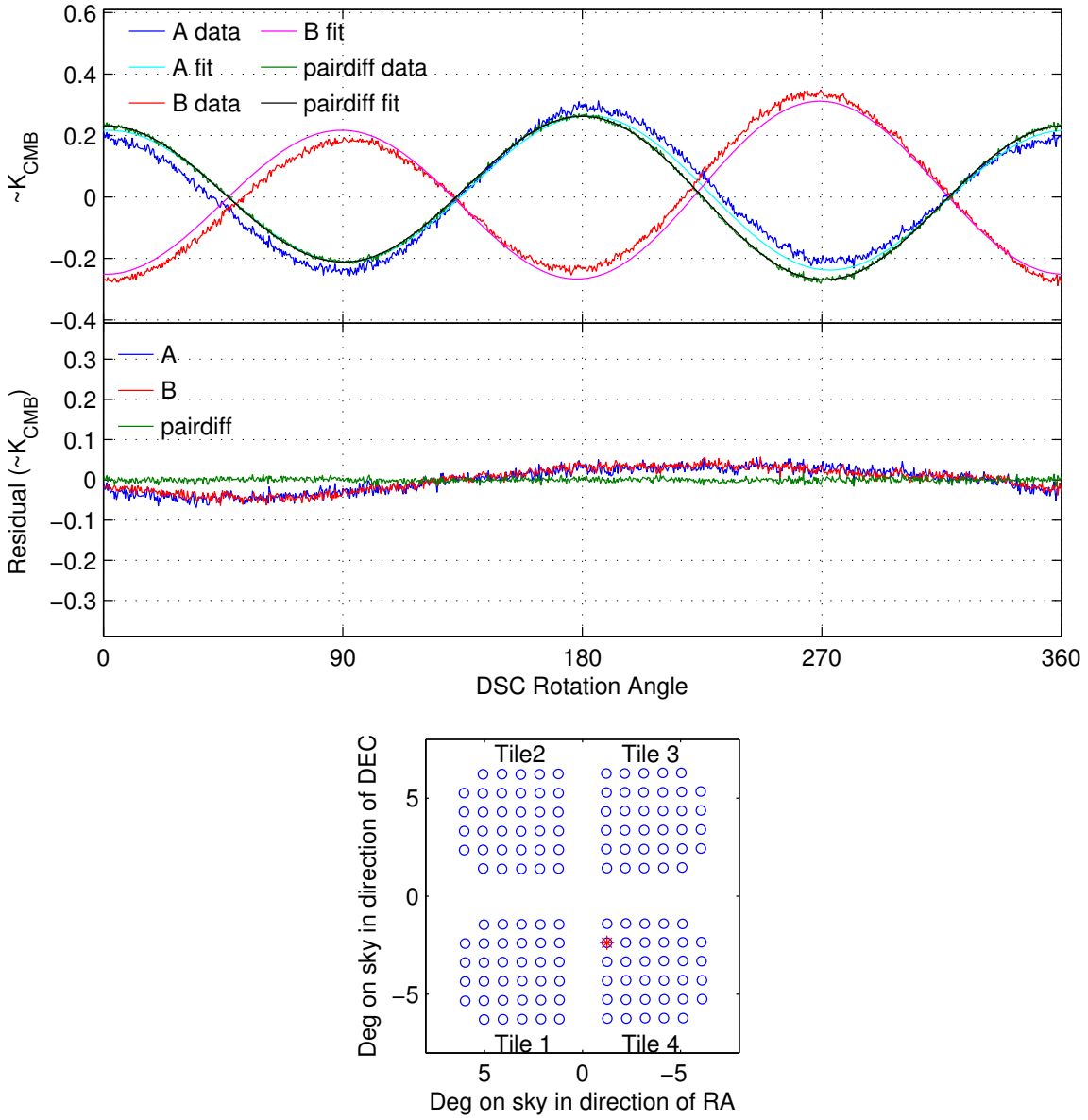

Figure A.5: DSC data for a detector pair near the center of the focal plane for the same calibration run as shown in Figure A.2, which is on a 95 GHz receiver. The per-detector data and model are better matched than they were for the pair located near the corner of the focal plane, but there is still a large improvement when switching to the pair difference data and model.

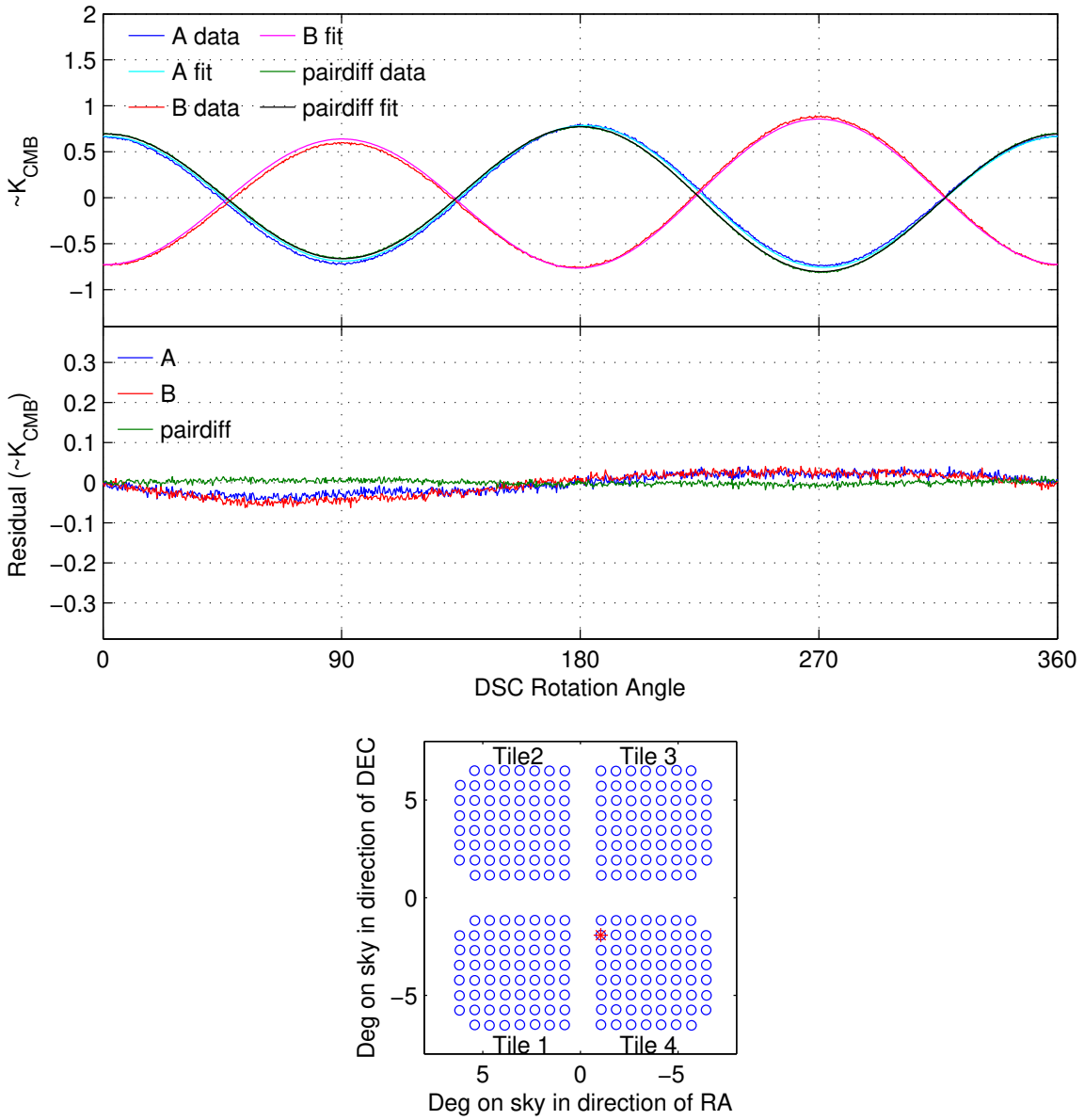

Figure A.6: DSC data for a detector pair near the center of the focal plane for the same calibration run as shown in Figure A.3, which is on a 150 GHz receiver.

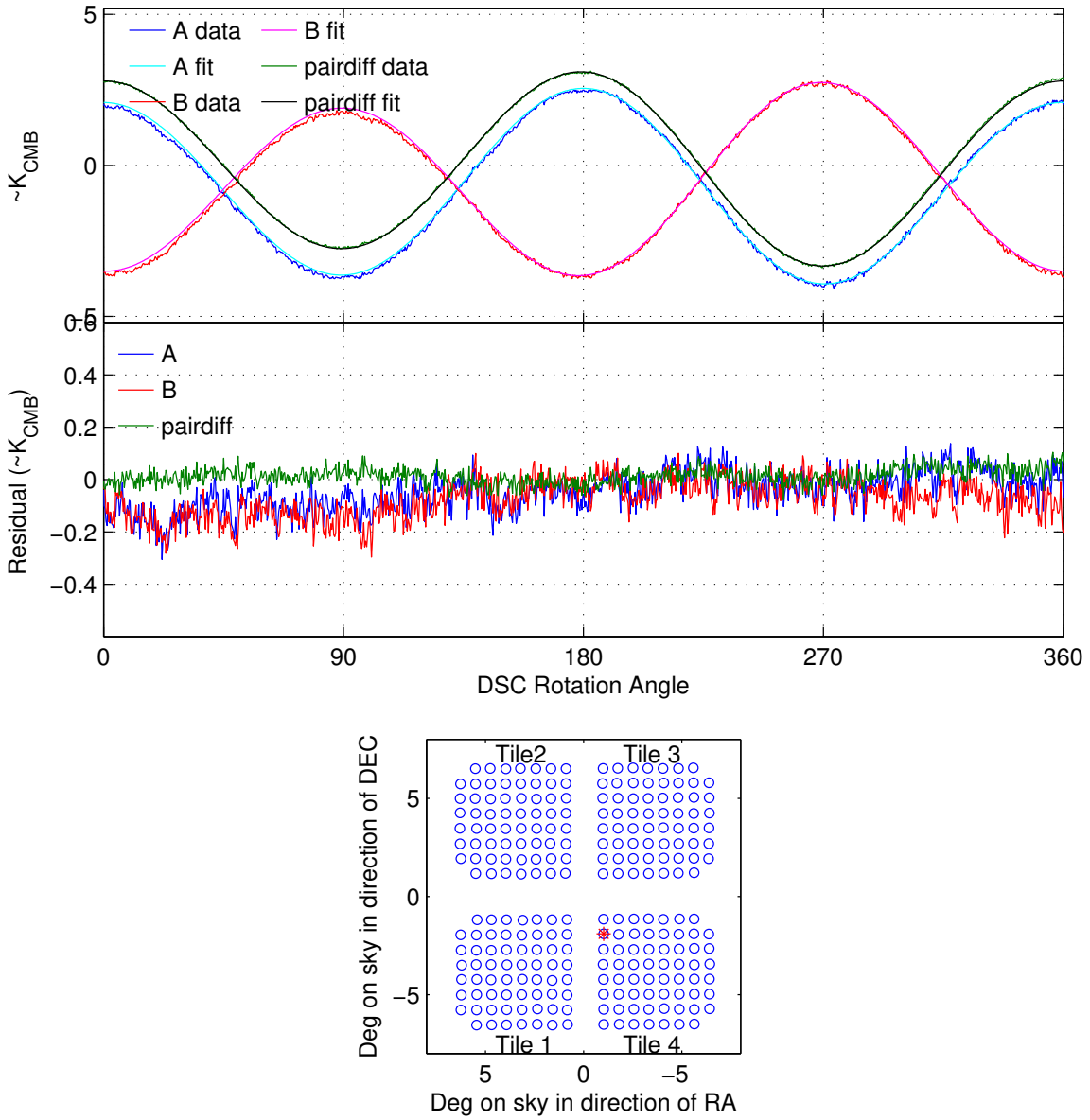

Figure A.7: DSC data for a detector pair near the center of the focal plane for the same calibration run as shown in Figure A.4, which is on a 220 GHz receiver.

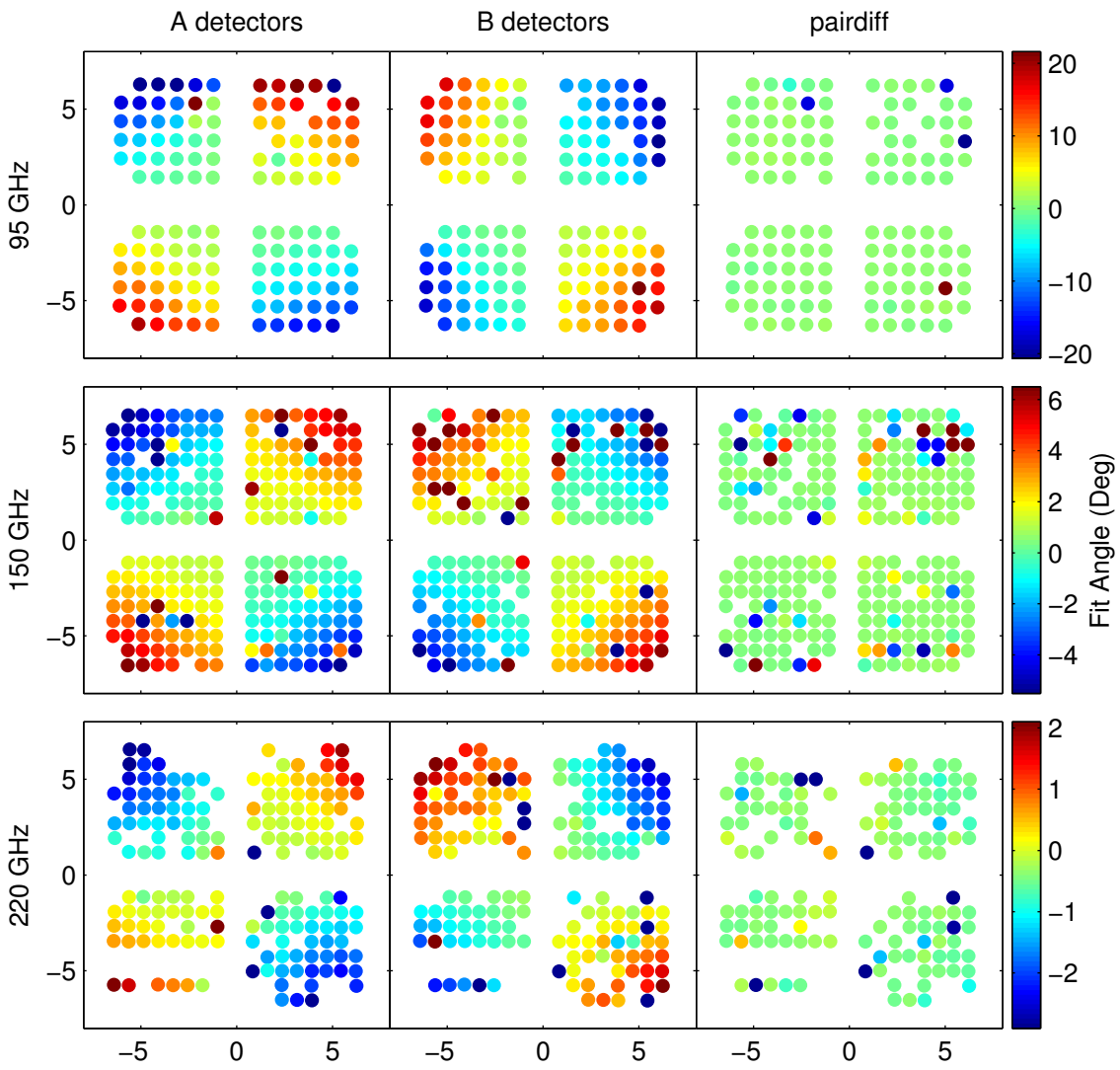

Figure A.8: Polarization angle fits, with respect to design angles, for calibrations performed on 95, 150, and 220 GHz receivers (one run on each) in the 2014/2015 summer season. Columns from left to right are fit values for the A detectors, B detectors, and the pair difference signal. Frequencies are separated by row. Though the color stretch is common among plots at the same frequency, it decreases as the frequency increases. Missing detectors are the result of poor data. For more description of these plots, see the text.

A.3 Statistics on the Curves

We define statistics about the shapes of the signal curves and compare them to the best fit model. The statistics all involve the local maxima (peaks) and minima (troughs) of the curve. There are two of each for each revolution of the DSC. We compare the DSC rotation angle at which the peaks and troughs occur (hereafter referred to as the location) as well as the ratio of temperatures between the two peaks and between the two troughs, normalized by the range of the data.

Figure A.9 shows an example of the fitting procedure, in this instance at a peak. We start with the full timestream, typically about three revolutions, and we subtract the best fit linear nuisance parameter, a linear drift. We then fold the data over 360° to improve the accuracy of the eventual fit. Though it's not shown we replicate the data and place it between 360° and 720°. We need an ample amount of data on either side of a peak or trough in order to fit for it, so this step is necessary to fit any peaks or troughs that occur near 0° or 360°. We then estimate the locations of the peaks and troughs by finding the sign changes in the point-to-point derivative of a smoothed version of the folded timestream. Finally, we fit a parabola to the portion of data surrounding our estimated locations and use the parabola vertex as both the temperature and location for that peak or trough.

Using the above fitting method, we present three statistics for the peak locations in Figures A.10 to A.12 and an equivalent three statistics for the trough locations in Figures A.13 to A.15. The statistics shown are the locations of the first peak (or trough), the difference between the locations of consecutive peaks (or troughs), and the fractional temperature difference between consecutive peaks (or troughs). We present the statistics for both the A and B detectors within a pair and compare the actual data with the best fit model. Note that the best fit model rotates the polarization axis of the detectors by the amounts shown

in Figure A.8, amounts we do not trust represent reality. With that caveat, we make the following observations about Figures A.10 to A.15. (i) The model fits match the first data peaks in two of the focal plane quadrants but not the other two. Also, only one of the matching quadrants is the same between the A and B detectors within a pair. (ii) The model fits match the first troughs in a similar way to the peaks. The difference is that matching quadrants are reversed between the A and B detectors with respect to the peaks. (iii) The distance between peaks and troughs shows larger variation in the data than the model allows. Although the trough-to-trough spacing is nearly consistent between data and model at 220 GHz, the peak-to-peak spacing is not.

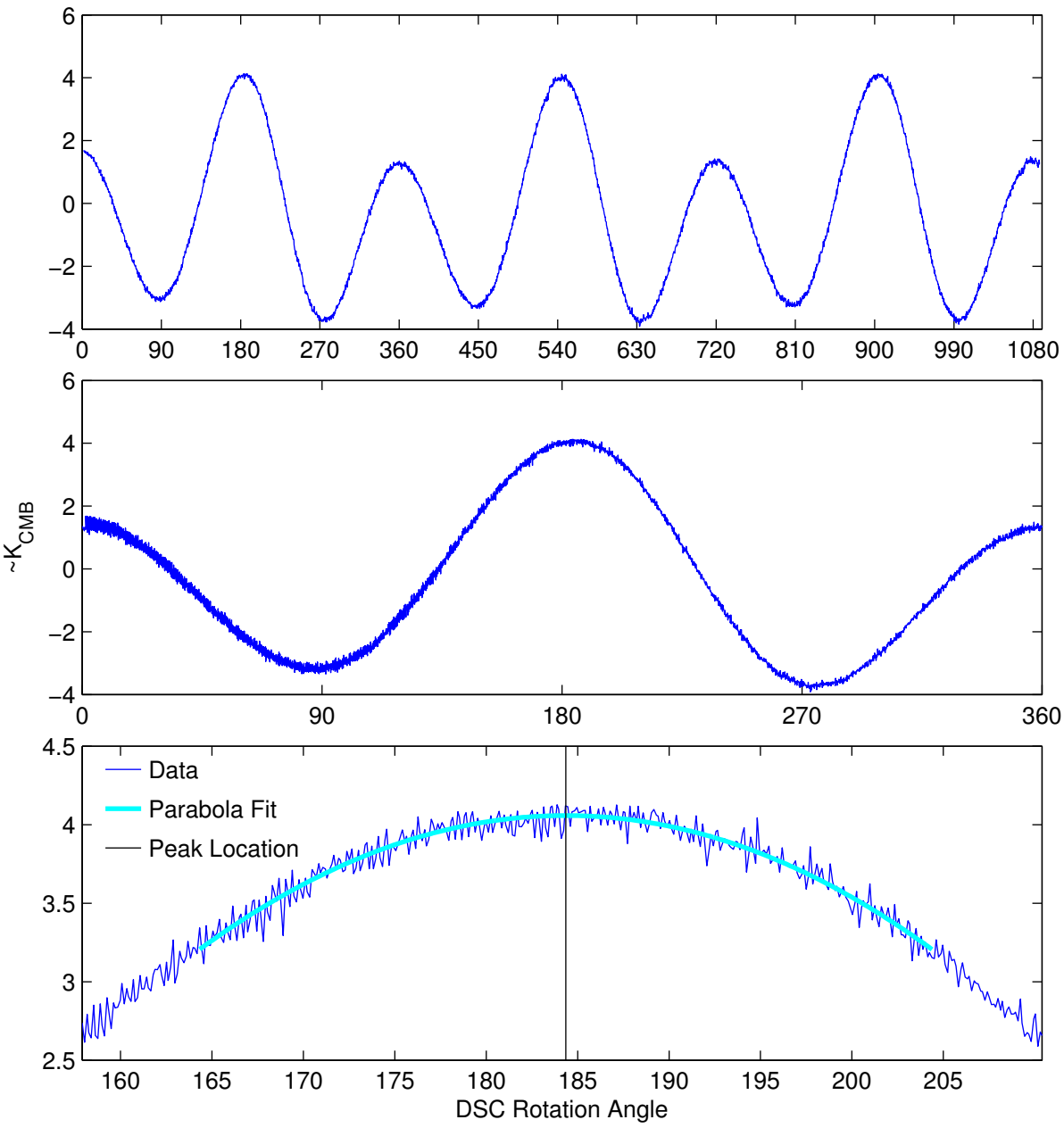

Figure A.9: Process of finding the peaks and troughs in a DSC timestream. *Top*: the full signal for the A detector shown in Figure A.4. This includes a little more than three revolutions of the DSC. *Middle*: The full signal is folded over 360°. *Bottom*: A zoom-in of the data around one of the inflection points of the folded data. A parabola fit is shown, the length of which shows the portion of the plotted data used in the fit. The vertex location of the parabola is indicated with a vertical line, indicating the value used as the estimate for this peak location.

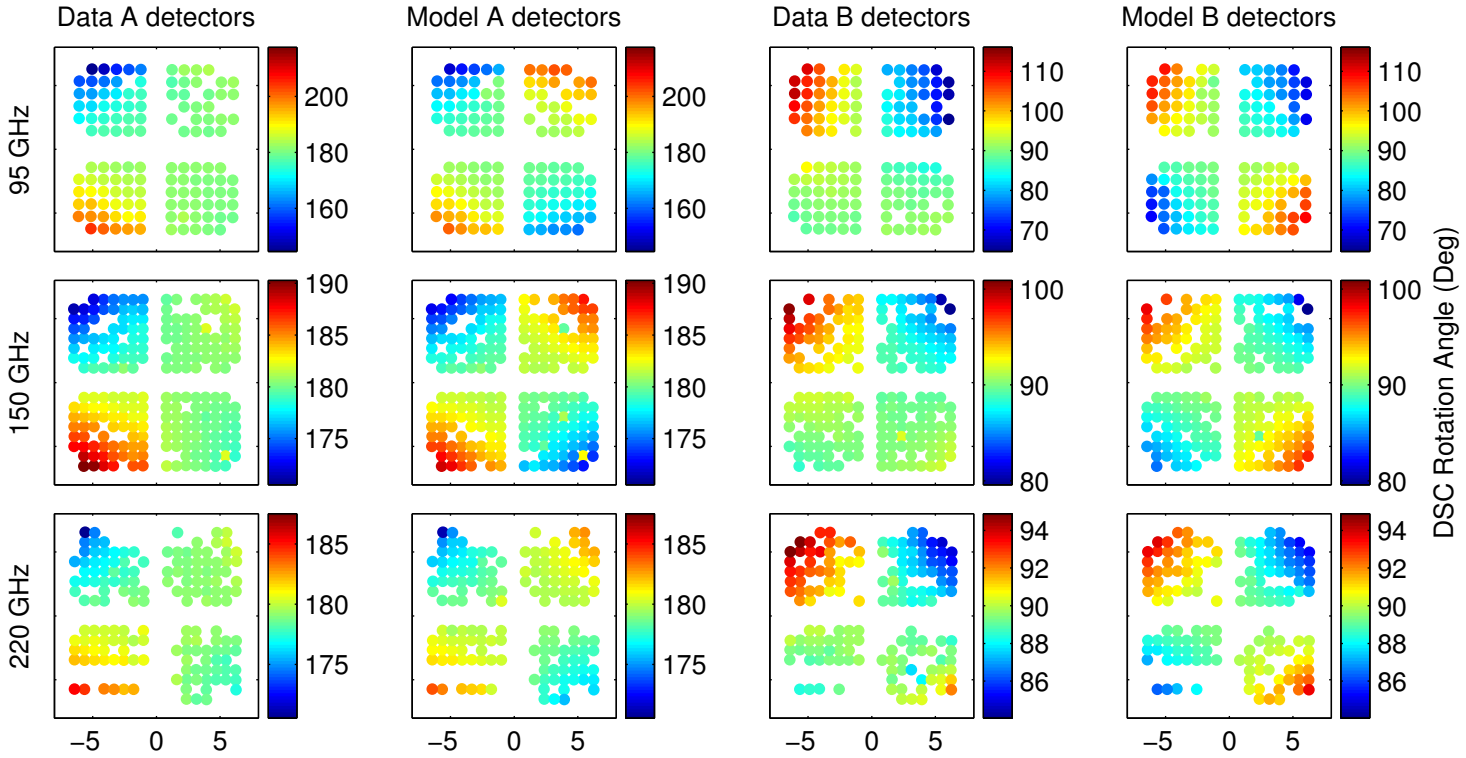

Figure A.10: Locations of the first peak for three receivers at three frequencies. Values for the A and B channels are shown for both the data and best fit model.

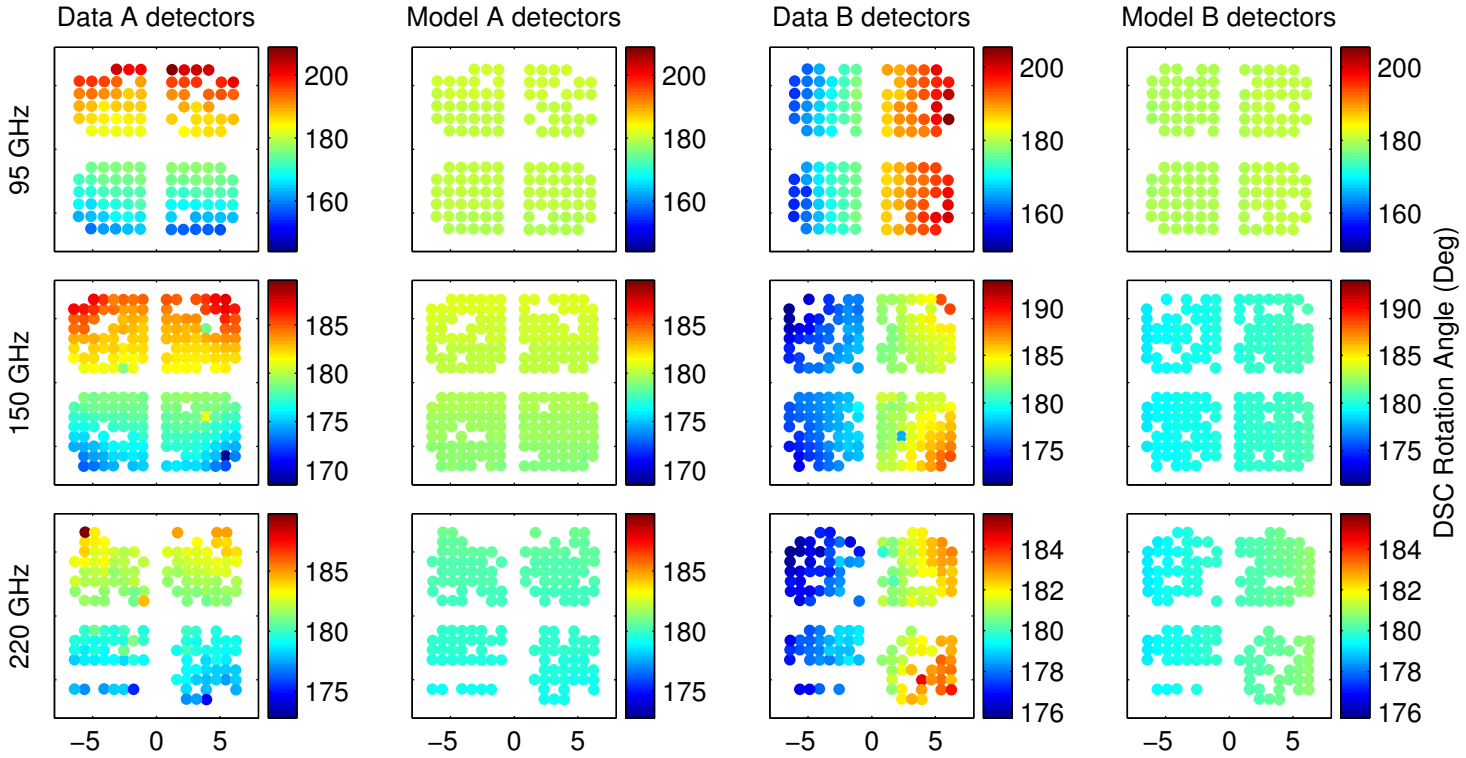

Figure A.11: Difference of the first two peak locations for three receivers at three frequencies. Values for the A and B channels are shown for both the data and best fit model.

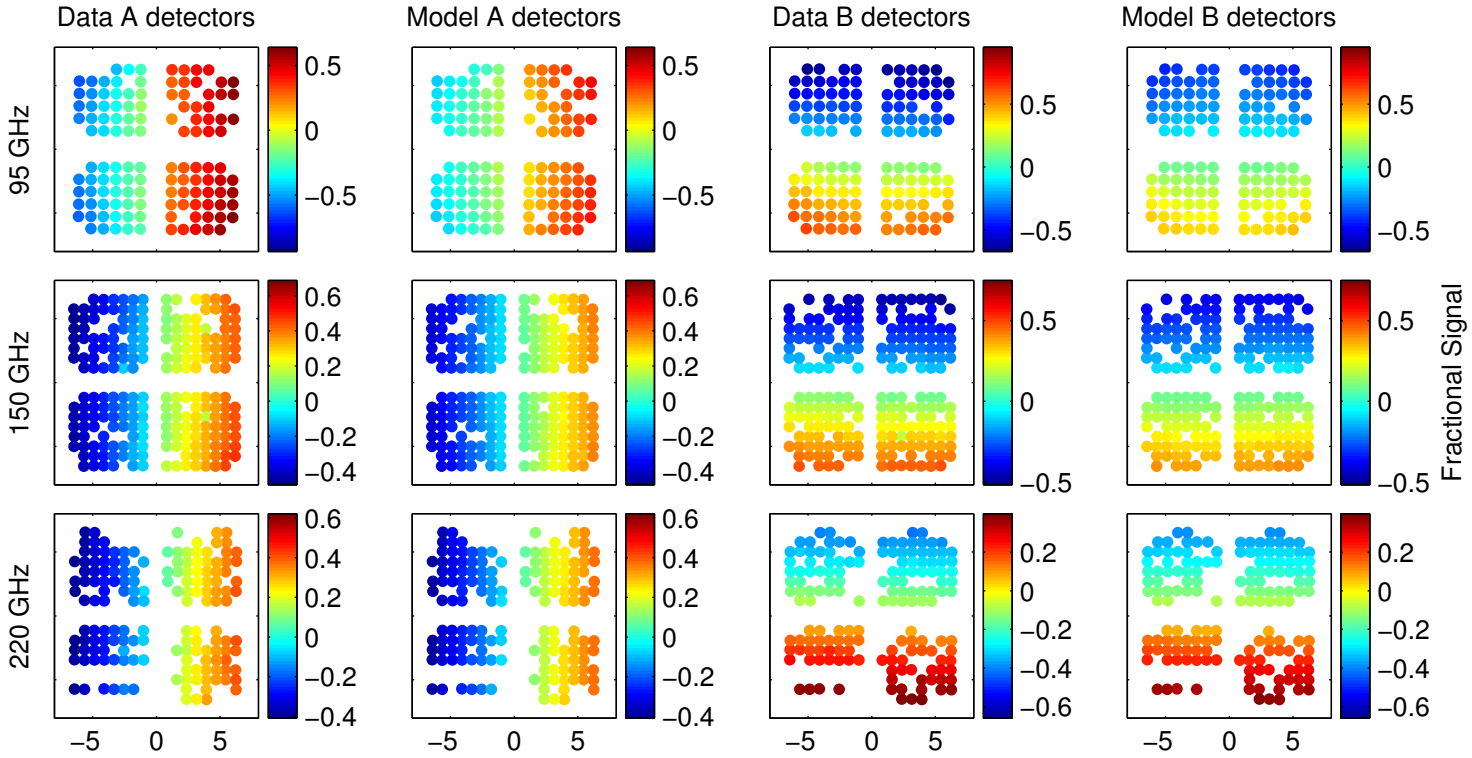

Figure A.12: Fractional temperature difference of the first two peaks for three receivers at three frequencies. Values for the A and B channels are shown for both the data and best fit model.

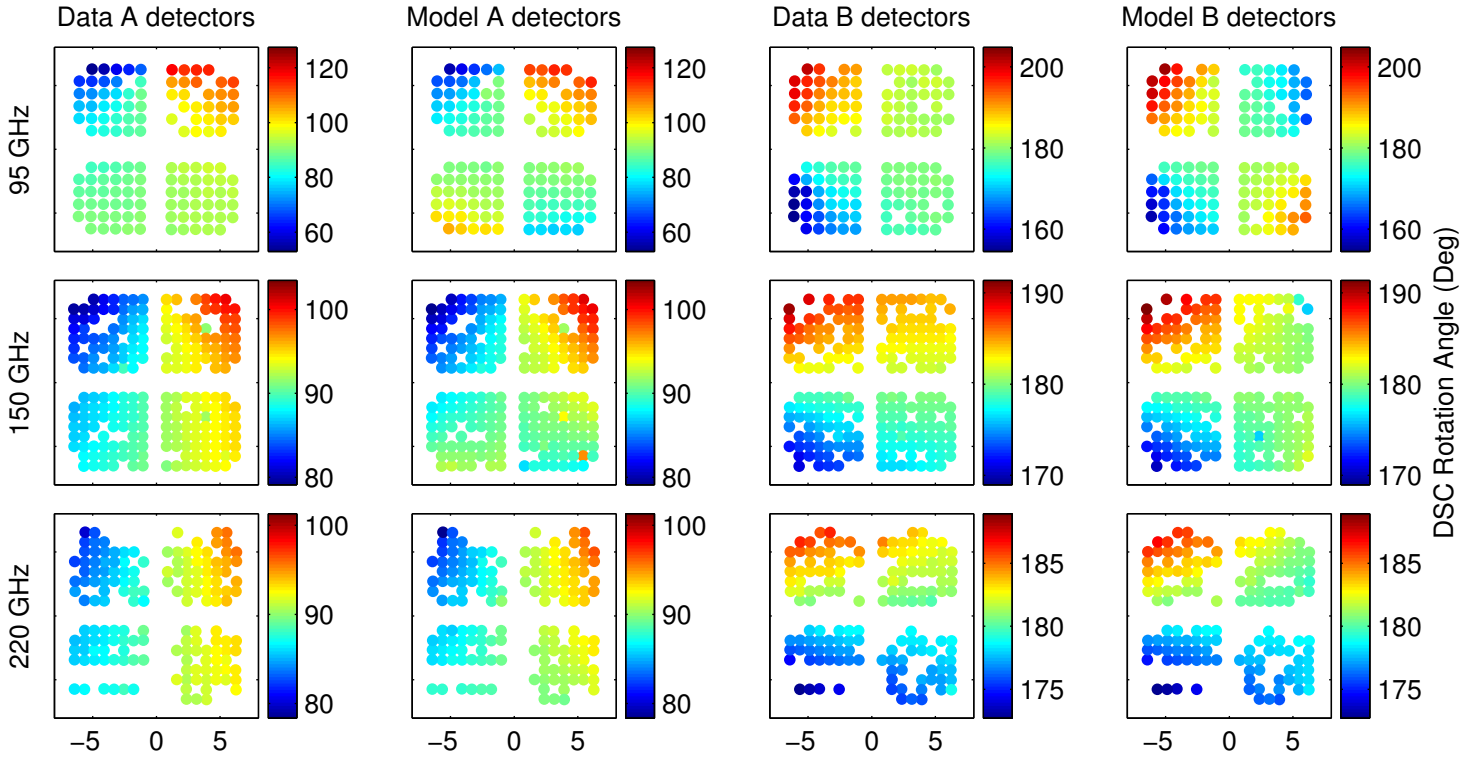

Figure A.13: Locations of the first trough for three receivers at three frequencies. Values for the A and B channels are shown for both the data and best fit model.

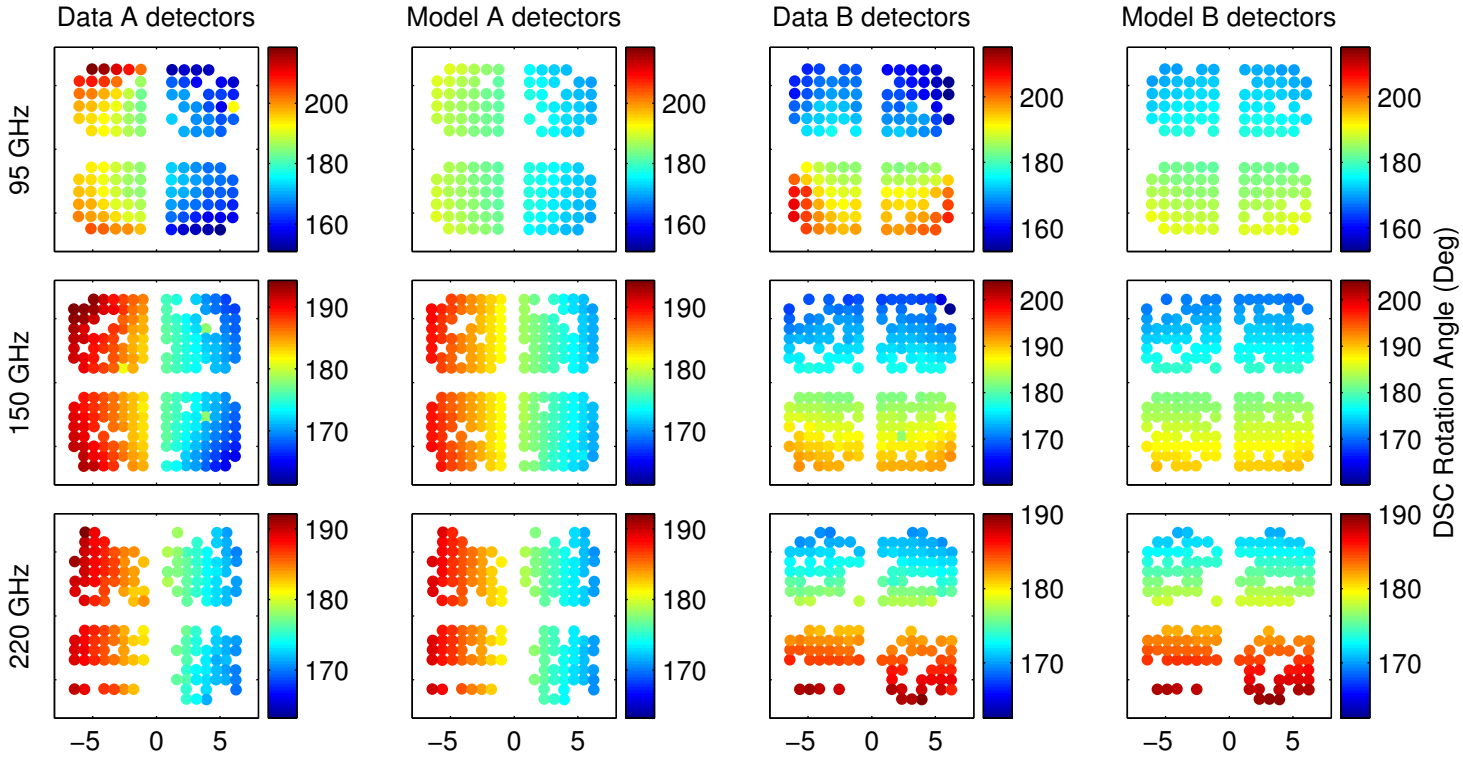

Figure A.14: Difference of the first two trough locations for three receivers at three frequencies. Values for the A and B channels are shown for both the data and best fit model.

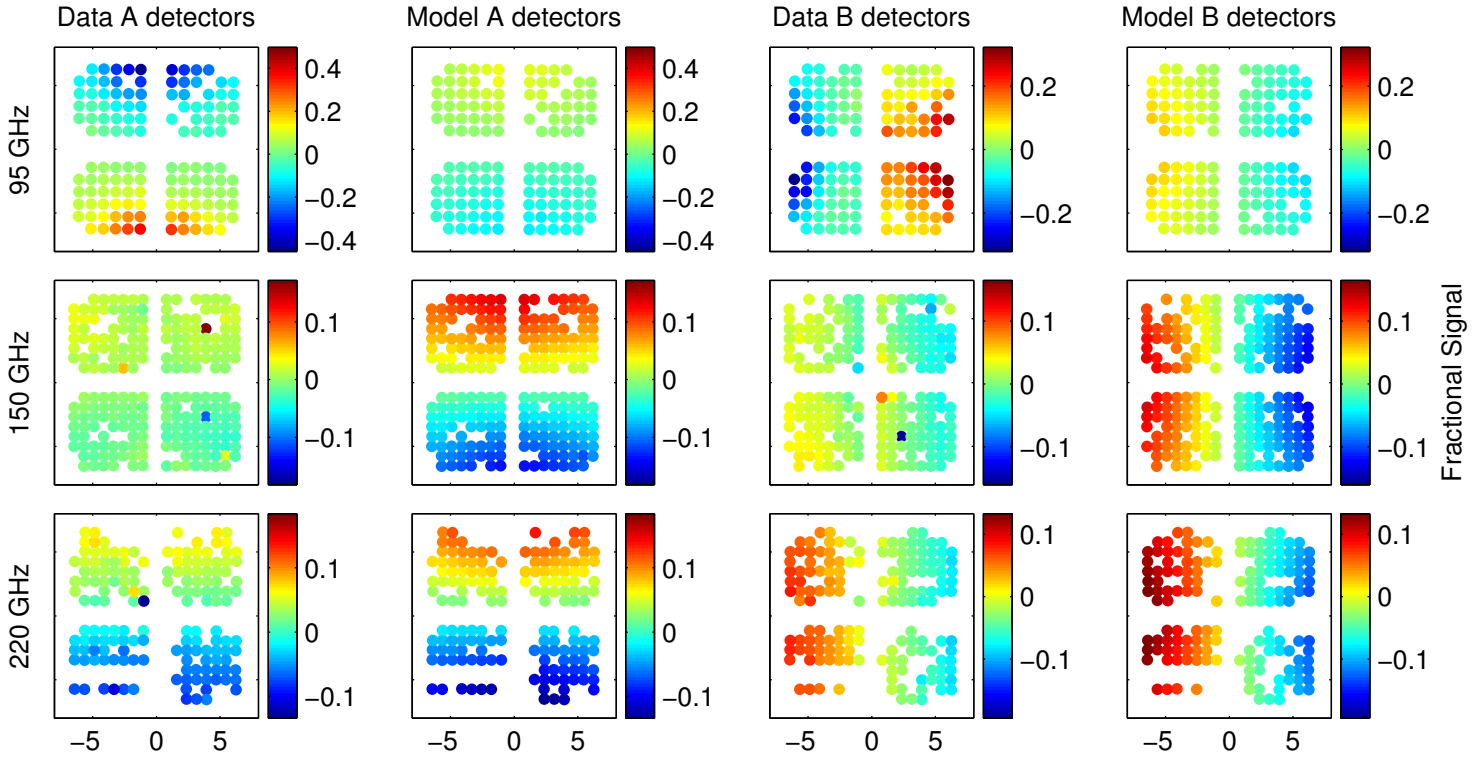

Figure A.15: Fractional temperature difference of the first two troughs for three receivers at three frequencies. Values for the A and B channels are shown for both the data and best fit model.

A.4 Final Remarks

With the data presented in this appendix, we can't blame the poor per-detector fit performance on the weather. First, the signal to noise is quite large, even at 95 GHz which has the weakest signal of the three frequencies. Second, Figure A.8 shows a pattern in the polarization fit angles across the focal plane, and that pattern is consistent across the frequencies. If this were due to atmospheric variations, it would require the atmosphere add signal to the detectors in a radial and 2-ϕ pattern. Third, though it's not shown, Figure A.8 would look very similar if we would have used the data from other calibration runs. These data sets span multiple days and multiple years. In order to explain the poor per-detector fits with the weather, the atmospheric variations would need to be correlated with the rotation angle of the calibrator, and the correlation would need the same phase for each calibration run.

In Section 4.7, we suggested that the aluminum ring which holds the dielectric sheet may inject an excess signal if it rotates in and out of the detector beams, but we don't insist that this is the only possibility. We are searching for an excess signal in our data that is not accounted for in our model. The above three points eliminate weather from consideration as a first-order source of this excess. Further, the excess signal must be mostly common-mode within a detector pair, and it must be associated with the calibration apparatus. Finally, any dependence on frequency must be smaller than ν^2. If this last point weren't true, we would expect the excess signal would have the same ratio to the calibration signal at all frequencies, and the patterns in the fit angles shown in Figure A.8 would have similar amplitudes at all frequencies.